Experimentelle Physik

Development of a high-repetition-rate intense ultrashort optical parametric chirped-pulse amplifier system with a global dispersion management

Inaugural-Dissertation
zur Erlangung des Doktorgrades
der Naturwissenschaften im Fachbereich Physik
der Mathematisch-Naturwissenschaftlichen Fakultät
der Westfälischen Wilhelms-Universität Münster

vorgelegt von
Wataru Kobayashi
aus Tokyo
-2012-

Dekan:	**Prof. Dr. T. Kuhn**
Erster Gutachter:	**Prof. Dr. H. Zacharias**
Zweiter Gutachter:	**Prof. Dr. C. Fallnich**
Tag der mündlichen Prüfung:	**07. 09. 2012**
Tag der Promotion:	**07. 09. 2012**

Thesis contents

1. **Introduction**

2. **Fundamentals of optical pulses**

3. **Non-collinear OPCPA**

4. **Dispersion management in OPCPA**

Chapter 1

Introduction

This thesis focuses on the development of a high-repetition-rate intense few-cycle near-infrared pulse source in optical parametric chirped-pulse amplification (OPCPA). A novel stretcher-compressor design is introduced to realize a large stretching factor of more than 10^4 with a broad acceptance bandwidth from 690 nm to 1010 nm and a high transmission efficiency of more than 90 % through the compressor system. Coupled with an adaptive dispersion device, the system successfully compresses amplified pulses down to sub-10 fs. The laser system with such a large stretching ability has a feasibility for the further energy scaling by use of a high-energy pump laser and it may serve to generate high-average-power ultrashort extreme ultraviolet (EUV) and soft x-ray pulses through the high-order harmonics generation (HHG) process.

1.1 Motivation: Soft x-ray spectroscopy and microscopy

Since the first coherent radiation in the infrared region by use of a ruby (Cr^{3+}:Al_2O_3) in 1960 [1], physical and chemical properties of various systems have been much more precisely investigated through temporally and spatially localized optical pulses. Recently, one can easily operate table-top size high-intensity femtosecond (fs) laser systems owing to the progress of mode-locking techniques and compact amplifier systems. The intense fs laser source has proved to be a powerful tool for the time-resolved spectroscopic measurements due to its extremely short temporal duration and achievable peak intensity. One can investigate the dynamics of the molecules in gas phases by means of fs-laser-based time-resolved Raman spectroscopy [2], photoelectron spectroscopy [3], and so on. The key point of the ultrafast spectroscopic measurement is that the duration of the laser pulses must be shorter than the time scale for the dynamics of the system. The "femtosecond" is the fundamental time scale for tracing molecular motions [4]. For example, the rotational transitions of a molecule lie in the microwave region (1 picosecond (ps) - 100 ps), and the vibrational transitions in the region from the visible to infrared (10 fs - 1 ps) [5]. Femtosecond pulses provide quite high resolutions to take snapshots of these fundamental motions of molecules.

The ultrafast time-resolved spectroscopic study is commonly based on a pump-probe method, i.e. a fast reaction is induced by a pump pulse and the process is scanned by a temporally delayed probe pulse [6]. With this method, various photo-induced ultrafast dynamics in molecular systems have been investigated [7]. Optical pulses with high energy densities expand the application of time-resolved ultrafast spectroscopies from from analyses of exited ultrafast dynamics to the direct manipulation of the system such as the coherent control of chemical reactions [8] and the dissociation and recombination of chemical bonds [9, 10]. The study on ultrafast dynamics by use of fs laser pulses has been comprehensively classified as femtochemistry [11].

The observation and control of even faster dynamics such as electronic motions demand the sub-fs time scale. However, due to the temporal period of the optical wave cycle, the pulse duration in visible region is restricted to a few-fs range (e.g. 2.6 fs for 800 nm). At present, no amplifier medium is found that generates ultraviolet sub-fs pulses directly from the laser cavity. Instead, laser-like coherent radiation at the wavelength of vacuum-ultraviolet (VUV), EUV, and soft x-ray are available through a process of HHG in noble gases [12-15]. In such short wavelengths, coherently superimposed optical waves form ultrashort pulses whose temporal duration is of the order of sub-fs and attosecond. New records on the attosecond pulse generation through the HHG process have been vigorously reported since the beginning of 21st century [16-24]. Now, the research trend has been shifting from femtochemistry to a new branch of science, attophysics, for the investigation of the fastest physical event [25-29].

Such ultrashort pulses obtained through HHG make an important role in a field of atom-, molecular- and bio-science. For example, time-resolved spectroscopic measurements have observed the inner-shell electronic dynamics in atoms [22, 30], imaged an electron orbital in molecules [31], and directly revealed the electric field of a light pulse [32]. In the soft x-ray region including the water-window spectral region (2.4 nm - 4.3 nm), the absorption coefficient of the carbon and oxygen becomes so large that the influence of the water on the microscopic measurement can be neglected. Therefore, the soft x-ray attosecond pulse source is feasible for the high-contrast biological imaging [33-35]. However, the practical applications through the HHG process suffer from the low photon flux in shorter wavelengths than the EUV region due to the small conversion efficiency [36]. Usually, bright soft x-ray sources are based on synchrotron radiation. This does not, however, satisfy the demands sufficiently, because of its long pulse duration, large system size, and high cost. Compared to the synchrotron, laser-based soft x-ray sources generate coherent sub-fs x-ray pulses with a compact system and comparatively low cost. In order to obtain the brilliant soft x-ray radiation, researchers have competed to develop high-repetition-rate optical sources and increased the average soft x-ray photon flux. In spectroscopic measurements, the high-average power leads to the increase of the counting rate for the precise statistics and, in the microscopic measurement, the signal-to-noise ratio in the soft x-ray-imaging [37]. Consequently, the generation of high intensity ultrashort soft x-ray pulses with a high brilliance is essential for the application of the laser-based soft x-ray source to the spectroscopic and microscopic measurements. The point in obtaining high-flux soft x-ray through HHG is to irradiate noble gases with intense ultrashort near-infrared optical pulses at a high repetition rate. Especially, for generating isolated soft x-ray attosecond pulses, it is necessary to produce optical pulses in the near-infrared region with the electric field oscillating only few cycles in a wave packet, i.e. few-cycle pulse. In this thesis, we report a high-repetition-rate intense ultrashort optical parametric chirped-pulse amplifier (OPCPA) system, which exactly satisfies these demands and is expected to be a powerful optical source for a time-resolved soft x-ray spectroscopy and microscopy through the HHG process. This laser system is a recent technique but is based on two conventional amplifier concepts CPA and OPA. Before we introduce this novel laser system, we briefly overview the fundamental concepts for these laser pulse amplification methods.

1.2 General introduction to intense ultrashort pulse generation

The first ruby laser was already pulsed laser due to the flash-lamp pumping. Later Q-switching and mode-locking techniques have made large progresses in the intense optical pulse generation. The Q-switching method has succeeded to generate high-energy giant pulses with the pulse duration from nanoseconds to several hundred picoseconds. The ultrashort pulse generation down to sub-ps regime was realized only after a mode-locking technique was developed. It has been also one of the important issues to develop broadband amplifier media were to generate ultrashort laser pulses. Especially, it was a large step forward that a dye medium was replaced with a broadband titanium-doped sapphire (Ti:sapphire, Ti^{3+}:Al_2O_3) crystal [38]. Combined with a Kerr-lens mode-locking technique [39], Ti:sapphire lasers succeeded to generate few-cycle pulses with a simple and compact setup [40, 41]. However, the pulse energy is limited to nJ-revel, and further energy scaling requires external amplifier systems. A widely implemented approach to amplify ultrashort pulses is traditionally based on Ti:sapphire chirped-pulse amplification (CPA) [42, 43]. Fig.1.1 schematically depicts the concept of CPA. This technique pays attention to the fact that the pulse peak power is controlled through the temporal stretching and compression of the pulse. Ultrashort pulses from the Ti:sapphire oscillator are stretched in time to decrease the peak intensity by a factor proportional to the amount of pulse stretching, and then the stretched pulses are amplified by efficiently extracting energy from the laser gain medium under the damage-threshold of the medium, and finally the duration of the amplified pulses is returned to the original duration through a compressor. CPA has achieved extremely high power densities in an ultrashort time scale and has made progress in high energy laser pulse generation. However, the pulse generation in a few-cycle regime has been difficult to achieve because the gain narrowing during the amplification limits the spectral bandwidth [44, 45]. For the purpose of generating intense few-cycle pulses, the CPA systems need a help of external gas-filled hollow waveguides [46] or filamentation in gases [47]. These systems are, however, limited in the pulse energy scaling due to the low damage threshold of the hollow-core fiber or the unstable multi filaments generation. The energy scaling of few-cycle pulses by use of the Ti:sapphire CPA system is therefore limited to a few mJ.

There is another direct energy scaling technique by use of a nonlinear crystal, which is referred to as optical parametric amplification (OPA). OPA is now a promising technique to obtain an extremely broad gain bandwidth [48-51]. This technique is based on the frequency conversion through a three-wave mixing process in a nonlinear crystal [52]. A first

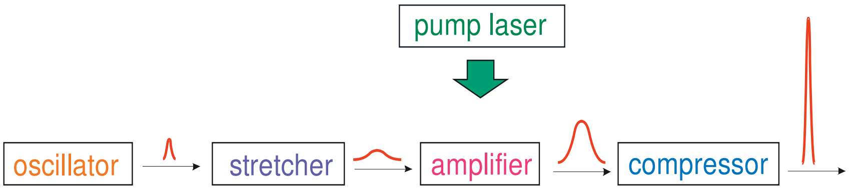

Figure 1.1: Principle of chirped-pulse amplification (CPA). The pulse stretching, amplification, and compression are depicted in the figure. Ultrashort pulses with a high peak power are obtained after the CPA system.

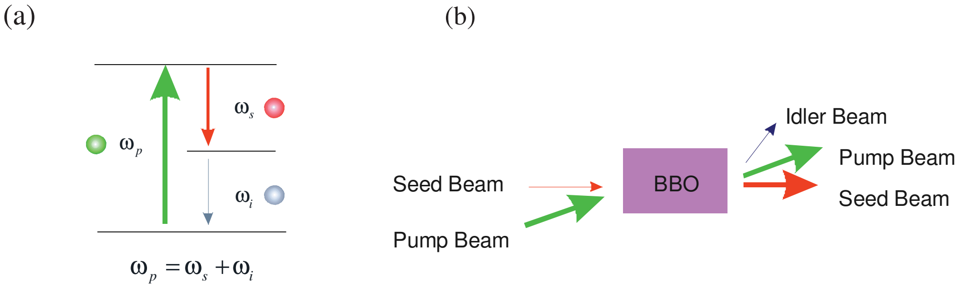

Figure 1.2 (a): Difference frequency generation (DFG). Pump photon, signal photon, and idler photon are depicted. When seeded with a low frequency beam, the system enables to amplify the low frequency beam. (b): Scheme of the non-collinear optical parametric amplification (NOPA).

demonstration of the nonlinear wave-mixing process was reported by Franken, who succeeded to generate frequency-doubled coherent UV radiation from quartz crystal by use of a pulsed Ruby laser in 1961 [53]. A sum frequency of two different wavelengths was achieved as well in 1962 [54]. Afterwards, a difference-frequency generation was observed, i.e. a high-frequency pump photon is split into two photons, one of which has the same frequency as a seeded photon (Fig. 1.2 (a)). OPA aims at the amplification of the signal beam through the difference-frequency process [55]. The broadband amplification is realized in a non-collinear beam geometry, where the signal and pump beam cross each other at a certain angle (Fig. 1.2 (b)). This non-collinear optical parametric amplification (NOPA) has opened a way for the direct amplification of few-cycle optical pulses [56-58] at a high repetition rate, but the energy is limited to the μJ range.

Recently, researchers have paid attention to a novel amplification technique, OPCPA [59, 60], as an attractive alternative to the conventional amplifier systems. OPCPA is presently an only possible technique for boosting the energy of few-cycle pulses to terawatt-level without using additional spectrum-broadening devices such as a hollow-wave guide or filamentation.

Besides, it does not suffer from thermal problems even if the repetition rate is increased. This thesis reports a new OPCPA system for the purpose of the investigation for ultrafast dynamics of molecule, atoms, electrons, and surfaces.

1.3 Optical parametric chirped-pulse amplification (OPCPA)

The energy scaling of few-cycle pulses is performed by combining OPA with CPA to form a newly emerging amplifier configuration, OPCPA. An original model was experimentally demonstrated by Piskarskas *et al*. in 1986 [59]. This report proved that the signal phase modulation was not so much distorted during the amplification if the OPA gain bandwidth was larger than signal spectral width. An OPCPA system was then first demonstrated by Dubietis *et al* in 1992 [60]. OPCPA has unique advantages over the conventional Ti:sapphire CPA systems in some respects.

First, OPCPA exhibits an extremely broadband gain under optimum phase-matching conditions in non-collinear geometry. Besides, the intensity of the signal pulse is amplified exponentially with a high gain. The high single-pass gain minimizes the accumulation of undesired nonlinear effects in the crystal. Combined with high energy pump sources, OPCPA exhibits a high energy scaling of signal pulses. At present, optical sources based on OPCPA have succeeded to generate terawatt-class few-cycle pulses. The generation of 10-fs, 5.0-mJ pulses with 0.5-terawatt peak intensity in the near-infrared spectral region was reported by Ishii *et al.* [62]. Soon after, the generation of 2.0-terawatt 7.6-fs laser pulses was succeeded at a repetition rate of 30 Hz [63]. Recently, the peak power of few-cycle OPCPA has reached beyond 10 terawatt [64, 65]. The further broadband amplification beyond an octave is realized by the two-colour pumping OPCPA [66] and a supercontinuum from an all-normal-dispersion photonic crystal fiber [67].

Second, one can amplify the signal wave with a minimal heat deposition in a nonlinear crystal. In the conventional amplification based on the population-inversion medium, the excitation energy is converted into the photon energy (i.e. stimulated emission process) and thermal energy (i.e. non-radiative decay process). The amplifier system therefore demands external cooling system to suppress thermal effects in the crystal. In OPCPA, the photon energy that is not converted into the signal beam is emitted as idler radiation, so there remains no thermal load in the crystal. This shows great possibilities for the development of high-repetition-rate (high-average-power) laser sources. These days several research groups vigorously report on the development of high-average-power laser sources in OPCPA. 5-fs, 2.7-mJ laser pulses were obtained at a repetition rate of 1 kHz [68]. 8-fs laser pulses with an average power of 6.7 W at a repetition rate of 96 kHz and sub-5 fs pulses with an average power of 3.0 W at a repetition rate of 30 kHz were generated from a fiber-amplifier pumped OPCPA system [69-71]. Besides, sub-10 fs laser pulses were generated at a repetition rate of 143 kHz and with an average power of 430 mW [72]. Recently, octave-spanning OPCPA system generating 22-W average-power few-cycle pulses at 1-MHz repetition rate was reported [73].

Finally, the carrier-envelope phase (CEP) stability is maintained throughout the entire OPCPA system [83]. In few-cycle pulse regime, the amplitude of the optical wave becomes quite sensitive to the CEP. Because the HHG process strongly depends on the pulse-to-pulse CEP change, it is essential to stabilize the CEP. Usually the CEP is stabilized in the broadband Ti:sapphire oscillator before seeding the CPA system and again after the amplification because of thermal drifts in the amplifier medium. On the contrary, the OPCPA process has very weak influence on the CEP stability. In addition, the carrier-envelope offset can be measured and stabilized by use of the idler wave [74, 75].

The OPCPA system is therefore a great promising optical source for ultrafast soft x-ray spectroscopy and the attosecond pulse generation through the HHG process [76]. However, the OPCPA systems mentioned above [69-73] have a limitation in the energy scaling due to the low stretching factor of the signal pulses to around a picosecond. Even higher energy is required for the application of the OPCPA to the soft x-ray spectroscopy and microscopy. In this thesis we report the development of an OPCPA system with a large stretching ratio of more than 10^4 through the broadband dispersion management. This system is unique in that a novel stretcher-compressor deign is applied to the high-repetition-rate intense ultrashort OPCPA system. A large stretching ability allows the feasibility of rather long high energy pump pulse sources to the OPCPA system. In order to develop such an OPCPA laser system, there are several requirements that must be carefully considered. First, the phase-matching condition must be precisely optimized. Although two operating modes NOPA and OPCPA should be distinguished, it is revealed that both modes represent the same technique and share a common concept [61]. The phase-matching angle, the non-collinear angle, the crystal thickness, and the pump intensity decide the gain amount and amplification bandwidth. Second, the pump laser must satisfy several requirements such as a high pulse energy, a good shot-to-shot stability, and a nice beam quality, for the signal amplification is quite sensitive to the output characteristics of the pump source. Third, a moderate signal pulse durations is required to achieve an efficient extraction of the pump energy, i.e. a high energy-conversion efficiency. The balance of the signal and pump pulse duration influences the timing-jitter-induced shot-to-shot stability of the output signal pulse as well. Finally, the dispersion management up to high orders is required to make the phase constant over a broad spectral range. This thesis reports the development of a novel OPCPA system addressing these requirements.

1.4 Outline of this thesis

This thesis is expanded into 7 chapters. First, fundamentals of the optical pulses are introduced in *Chapter 2*. Here the basic knowledge on optical pulse and techniques for pulse characterization are discussed. In *Chapter 3* the OPCPA simulations are presented on several conditions under the small-signal approximation and by use of modified coupled wave equations. The phase-matching condition, crystal length, spectral phase in OPCPA, and the influences of the pump and signal fluctuation and timing-jitter on the CEP are investigated. In

Chapter 4 the dispersion management of the broadband spectrum is discussed. Here the optimum combination of the stretcher and compressor and its new design are evaluated for a broadband acceptance width with a large stretching ability. The experimental setups and their results are presented in *Chapter 5* and *Chapter 6*. *Chapter 5* mainly introduces whole system setup and amplification results by use of a new pump laser. *Chapter 6* concentrates on final compression results through the higher-order dispersion compensation. *Chapter 7* presents the conclusions and a further outlook.

Chapter 2

Fundamentals of optical pulses

This chapter provides a general introduction to optical pulses. The optical wave is mathematically described with wave equations. The solutions consist of the wave amplitude and the optical phase. The phase is Taylor-expanded to the dispersion terms, which provides the systematic description of the pulse propagation in a dispersive medium. The first-order dispersion describes the carrier-envelop-phase shift, while the second-order and even higher-order dispersion induce the temporal shape modulations. In the final section of this chapter, several representative techniques for the pulse characterization are introduced. These experimental techniques are essential to obtain the phase information and reconstruct the output pulse.

2.1 Mathematical framework of the optical wave

The knowledge of the electromagnetism can be directly applied to the propagation of optical waves. The Maxwell equations represent the propagation of the electric and magnetic field and lead to the following wave equation in vacuum: [77, 78]

$$\nabla\times\nabla\times\vec{E}(\vec{r},t)-\varepsilon_0\mu_0\frac{\partial^2\vec{E}(\vec{r},t)}{\partial t^2}=0 \tag{2.1}$$

$$\nabla\times\nabla\times\vec{B}(\vec{r},t)-\varepsilon_0\mu_0\frac{\partial^2\vec{B}(\vec{r},t)}{\partial t^2}=0\ , \tag{2.2}$$

where $\vec{E}(\vec{r},t)$ and $\vec{B}(\vec{r},t)$ are the electric field and magnetic field in the time-domain, respectively. $\varepsilon_0 = 8.854\times10^{-12}$ F/m is an electric permittivity of vacuum and $\mu_0 = 4\pi\times10^{-7}$ H/m is a magnetic permittivity of vacuum. The value of $1/(\varepsilon_0\mu_0)^{1/2}$ is equal to the speed of light in vacuum c_0. The following equations fulfill the solutions of these wave equations:

$$\vec{E}(\vec{r},t)=E_0e^{i(\vec{k}\vec{r}-\omega t)}+c.c. \tag{2.3}$$

$$\vec{B}(\vec{r},t)=B_0e^{i(\vec{k}\vec{r}-\omega t)}+c.c.. \tag{2.4}$$

These solutions stand for the sinusoidal waves traveling in vacuum at an angular frequency of ω and a wave number of k, where ω and k have a relation of $c_0 = f\lambda = \omega/k$. E_0 and B_0 are amplitudes of the waves and $\vec{k}\cdot\vec{r}-\omega t$ stands for the phase of the sinusoidal wave. The electromagnetic wave is a transverse wave, where the electric field and magnetic field are always vertical in propagation. The both waves have the same phase and simultaneously propagate in the same direction. The electrons in a medium receive the force mainly from the electric field, so the magnetic field is neglected in the following discussion for simplicity.

An optical pulse is formed through the coherent superposition of optical waves in a broadband frequency range. The electric fields in the temporal domain are described by adding the optical waves through the whole spectral domain (Fourier transform), and the electric fields in the frequency domain are described by the summation of the optical wave through the whole temporal domain (Inverse Fourier transform):

$$E(\vec{r},t)=\int_{-\infty}^{\infty} E(\vec{r},\omega)e^{-i\omega t}d\omega \tag{2.5}$$

$$E(\vec{r},\omega)=\frac{1}{2\pi}\int_{-\infty}^{\infty} E(\vec{r},t)e^{i\omega t}dt. \tag{2.6}$$

A transform-limited pulse is obtained under the constant phase. In vacuum the optical pulse receives no modulation because the wave vector doesn't depend on the frequency. In a dispersive device however the wave vector becomes a function of the frequency so the electric field is rewritten as follows:

$$\begin{aligned} E(\vec{r},\omega) &= E(0,\omega)e^{i\vec{k}(\omega)\vec{r}} \\ &= E(\omega)e^{i\phi(\omega)}, \end{aligned} \tag{2.7}$$

where $E(0,\omega)$ $(= E(\omega))$ is the spectral amplitude of the incident beam and $k(\omega)$ is the frequency-dependent wave-vector. The spectral phase $\phi(\omega)$ $(= k(\omega)r)$ becomes a function of the angular frequency. The temporal electric field is then described in the following form:

$$\vec{E}(\vec{r},t)=\int_{-\infty}^{\infty} E(\omega)e^{i\phi(\omega)}e^{-i\omega t}d\omega + c.c. \;. \tag{2.8}$$

The spectral phase includes all information on the dispersion. Once the spectral phase is known, the pulse stretching and compression are mathematically described.

2.2 Propagation in dispersive devices

When a transform-limited pulse propagates in a dispersive medium, the spectral phase receives a distortion. The spectral-phase distortion is expanded into Taylor series around the central frequency of ω_0 as follows:

$$\phi(\omega)=\phi(\omega_0)+\phi'(\omega_0)(\omega-\omega_0)+\frac{1}{2!}\phi''(\omega_0)(\omega-\omega_0)^2+\frac{1}{3!}\phi'''(\omega_0)(\omega-\omega_0)^3+\frac{1}{4!}\phi''''(\omega_0)(\omega-\omega_0)^4...$$

$$= \phi(\omega_0) + GD(\omega_0)\Delta\omega + \frac{1}{2!}GDD(\omega_0)\Delta\omega^2 + \frac{1}{3!}TOD(\omega_0)\Delta\omega^3 + \frac{1}{4!}FOD(\omega_0)\Delta\omega^4 \ldots \quad (2.9)$$

The bandwidth ($\omega - \omega_0$) is replaced with a notation $\Delta\omega$. The first-, second-, third-, and fourth-… order derivatives with respect to the central frequency ω_0 are named as group-delay (GD), group-delay dispersion (GDD), third-order dispersion (TOD), fourth-order dispersion (FOD)…, respectively. The first term $\phi(\omega_0)$ is the absolute phase, which defines the starting position of the electric-field oscillation. The GD is the travelling time of each frequency component in the dispersive medium. Usually, the constant term $\phi(\omega_0)$ and the GD have no influence on the pulse shape. The GDD and even higher terms change the temporal pulse duration and pulse shape. In the following two sections, optical pulses with the approximation of the spectral phase modulation of the first-order expansion term GD and the second-order expansion term GDD and even higher-order dispersions are discussed.

2.3 Carrier-envelope-phase (CEP) for few-cycle pulses

In few-cycle regime, the amplitude of the electric field becomes quite sensitive to the pulse envelope. Fig. 2.1 illustrates the pulse envelope (blue lines) and the carrier-wave (red line). The carrier-envelope phase (CEP) is the relative phase between the carrier-wave and the pulse envelope. The quantitative analysis of the CEP shift is represented by taking the GD into account. The transform limited pulse at the position z and time t can be written in terms of a pulse-envelope function and a carrier-wave oscillating at a central frequency ω_0 as follows

$$E(z,t) = A(z,t)e^{-i(\omega_0 t + \varphi)}. \quad (2.10)$$

The envelope function $A(z,t)$ is an amplitude of electric wave representing the shape of the optical pulse and φ is the absolute phase. When the GD is considered during the wave propagation, the electric field after the distance z is given by

$$E(z,t) = A\left(t - \frac{z}{\upsilon_g}\right)e^{i\omega_0\left(\frac{z}{\upsilon_\phi} - \frac{z}{\upsilon_g}\right)}, \quad (2.11)$$

where $\upsilon_g = 1/k^{(1)}$ is a group velocity and $\upsilon_\phi = c/n = \omega_0/k_0$ is a phase velocity. The first envelope function term indicates that the pulse shape remains constant during the propagation and the pulse travels in the medium at the speed of υ_g, while the second exponential term shows that the CEP is shift due to the difference between the phase velocity and the group velocity. The pulse-to-pulse CEP change is referred to as carrier-envelope phase offset (CEO). The CEO is described as frequency component given by [79]

$$\Delta\varphi = \omega_0\left(\frac{z}{\upsilon_\phi} - \frac{z}{\upsilon_g}\right)\mathrm{mod}\,2\pi \quad . \quad (2.12)$$

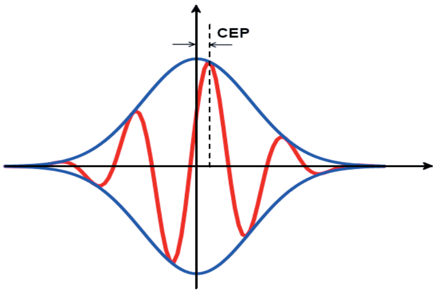

Figure 2.1: Illustration of a pulse envelope (blue line) and a carrier wave (red line) in an optical pulse. The amount of the carrier-envelope phase (CEP) is shown in the figure. The carrier wave moves at a phase velocity υ_ϕ, while the pulse envelope moves at a group velocity υ_g.

The CEO is detected by measuring the frequency-comb offset. The CEO $\Delta\varphi$ is related to the frequency-comb offset f_0 in the form of

$$f_0 = \frac{1}{2\pi} f_{rep} \Delta\varphi \quad , \tag{2.13}$$

where f_{rep} is the pulse repetition rate of the mode-locked laser. The measurement and stabilization of the CEP is therefore identically handled by measuring and stabilizing the f_0. The offset frequency is measured by use of several techniques such as the *f*-to-2*f* interferometer [79-83] and 0-to-*f* interferometer [84-88]. The frequency-comb is obtained by the Fourier-transform of the pulse train. In Fig. 2.2, the frequency-comb formation of the signal oscillator (Rainbow, Femtolasers GmbH) is shown. The above figures represent the optical waves packets and the below ones show the inverse Fourier-transformed spectra. The single-pulse spectrum corresponds to the measured spectrum (Fig. 2.2 (d)), while the two-pulse spectrum consists of narrow spike-like peaks separated at the interval of the repetition rate of the pulse train (Fig. 2.2 (e)). With the increase of the pulse number, the spectrum is transformed into the frequency comb (Fig. 2.2 (f)). The *f*-to-2*f* method is a widely used technique to measure the CEO frequency of pulses in femtosecond Ti:sapphire laser. Fig. 2.3 (a) shows the schematic of the *f*-to-2*f* scheme. A nonlinear crystal is used to generate a second harmonics of the fundamental spectrum, resulting in a generation of new frequency components. The interference beat frequency between the high-frequency and the frequency-doubled low-frequency spectral component of an octave spanning spectrum is measured [89]. The frequency component for the $\mathrm{n^{th}}$-mode of the fundamental spectrum can be written as

$$f_n = f_0 + n f_{rep} \quad . \tag{2.14}$$

If the spectrum is sufficiently broad covering one octave, it is possible to obtain the high frequency component given by

$$f_{2n} = f_0 + 2n f_{rep} \, . \tag{2.15}$$

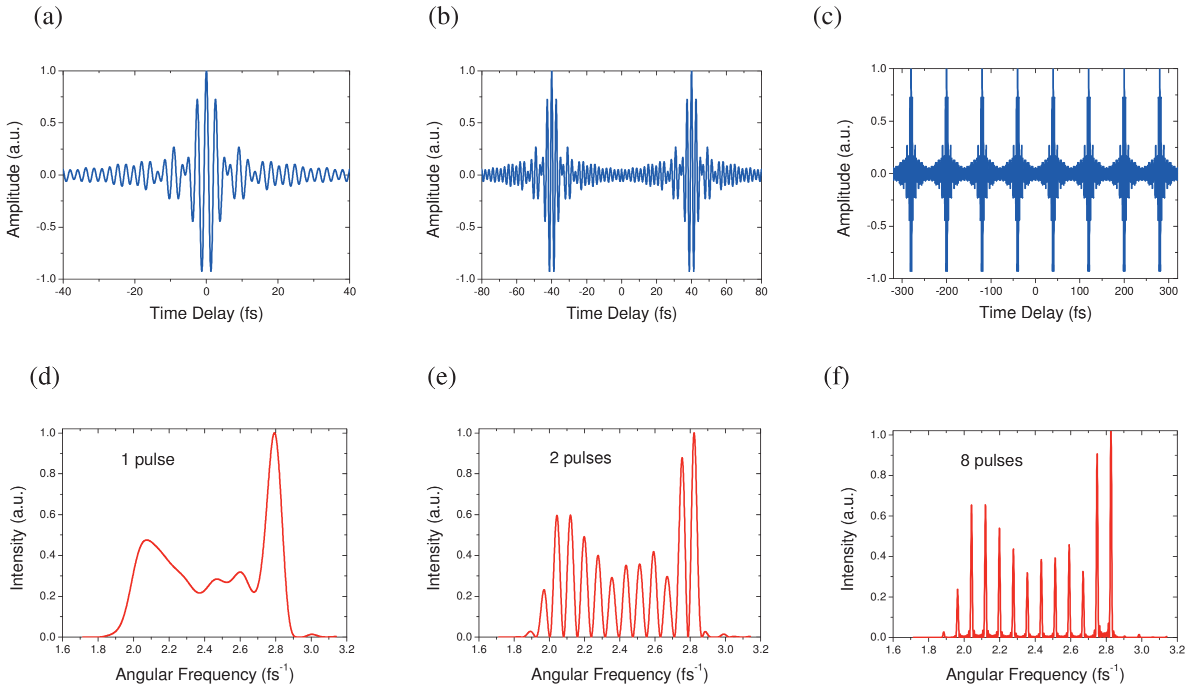

Fig 2.2: Relationship between the pulse number and the Fourier-transformed spectrum. (a)-(c): Pulse train from the Ti:sapphire oscillator (Rainbow, Femtolasers GmbH) and (d)-(f): corresponding Fourier-transformed power spectrum. This simulation follows the approach of Witte [83].

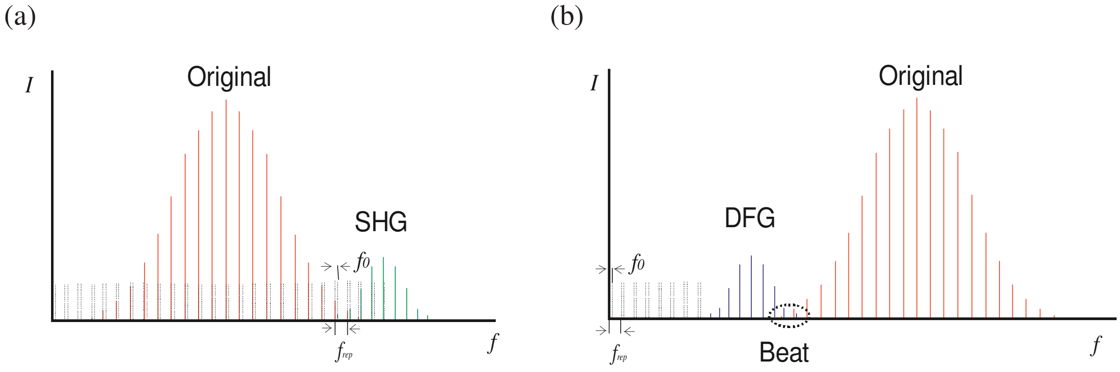

Figure 2.3: Spectrum of the frequency-comb for (a): f-to-2f technique and (b): 0-to-f technique. The frequency-comb is characterized by the mode spacing f_{rep} and the offset frequency f_0. f-to-2f technique uses the SHG signal to detect the f_0, while 0-to-f technique utilizes the DFG signal for the f_0 detection.

When the high-frequency component and the frequency-doubled low-frequency component are overlapped, a beat signal between the f_{2n} and $2f_n$ at the frequency of

$$2f_n - f_{2n} = 2(f_0 + nf_{rep}) - (f_0 + 2nf_{rep}) = f_0 \tag{2.16}$$

is measured. In order to broaden the fundamental spectrum over one octave, a photonic crystal fiber (PCF) or a glass plate are used. On the other hand, in case of the 0-to-*f* scheme, a difference frequency generation is utilized to measure the f_0. Fig. 2.3 (b) shows a schematic for the 0-to-*f* method. The difference frequency comb is produced by mixing the high-frequency part and the low-frequency part of the fundamental spectrum:

$$f_{df} = (f_0 + n_h f_{rep}) - (f_0 + n_l f_{rep}) = (n_h - n_l) f_{rep} \,, \tag{2.17}$$

where n_h and n_l are the n^{th}-mode of the high-and low-frequency component, respectively. It turns out from this equation that the different frequency is independent of f_0. Interference between the low-frequency component of the fundamental spectrum and the different frequency signal provides beating at f_0 by a 0-to-*f* comparison [87]. There are several advantages by use of the 0-to-*f* technique to measure the CEO frequency. The 0-to-*f* configuration is much simpler than the *f*-to-2*f* configuration due to the self-stabilization scheme. The alignment is also easy because the 0-to-*f* scheme requires no alignment-sensitive PCF. In addition, in the long term characteristics, the 0-to-*f* scheme has obvious advantages in hold time and coherence [89].

For the CEP stabilization, the ratio of v_ϕ / v_g inside the laser cavity is controlled [83]. There are several methods to achieve the stabilization, e.g. by tilting the end mirror in a prism-dispersion compensated mode-locked laser [79], or by modulating the pump intensity inside the gain medium of a Kerr-lens mode-locked laser [91].

2.4 GDD, TOD, and high-order dispersion

The pulse envelope receives a modulation if the dispersion of the 2nd order and more is introduced. In Fig. 2.4, several simulation results for the effect of the dispersion on the optical-wave are shown. Fig. 2.4 (a) shows a relative value of GD from the central wavelength of 800 nm and the corresponding optical wave. The wavelength-dependence of the GD provides an easy picture of the temporal information of the stretched pulse. The flat phase, i.e. the constant GD, provides a transform-limited pulse. When the GDD is introduced, the pulse is stretched in time with a temporal frequency variation (Fig. 2.4 (b)). A positive GDD stretches the pulse with a temporal gradation of frequency from low to high components, while a negative GDD with a temporal gradation of frequency from high to low components. Note that the peak amplitude of the optical wave in the stretched pulse becomes weaker than that in the transform-limited pulse. The CPA is the very technique that introduces the GDD into the transform limited pulse to suppress the peak intensity below the damage threshold. Fig. 2.4 (c) show the spectral GD with

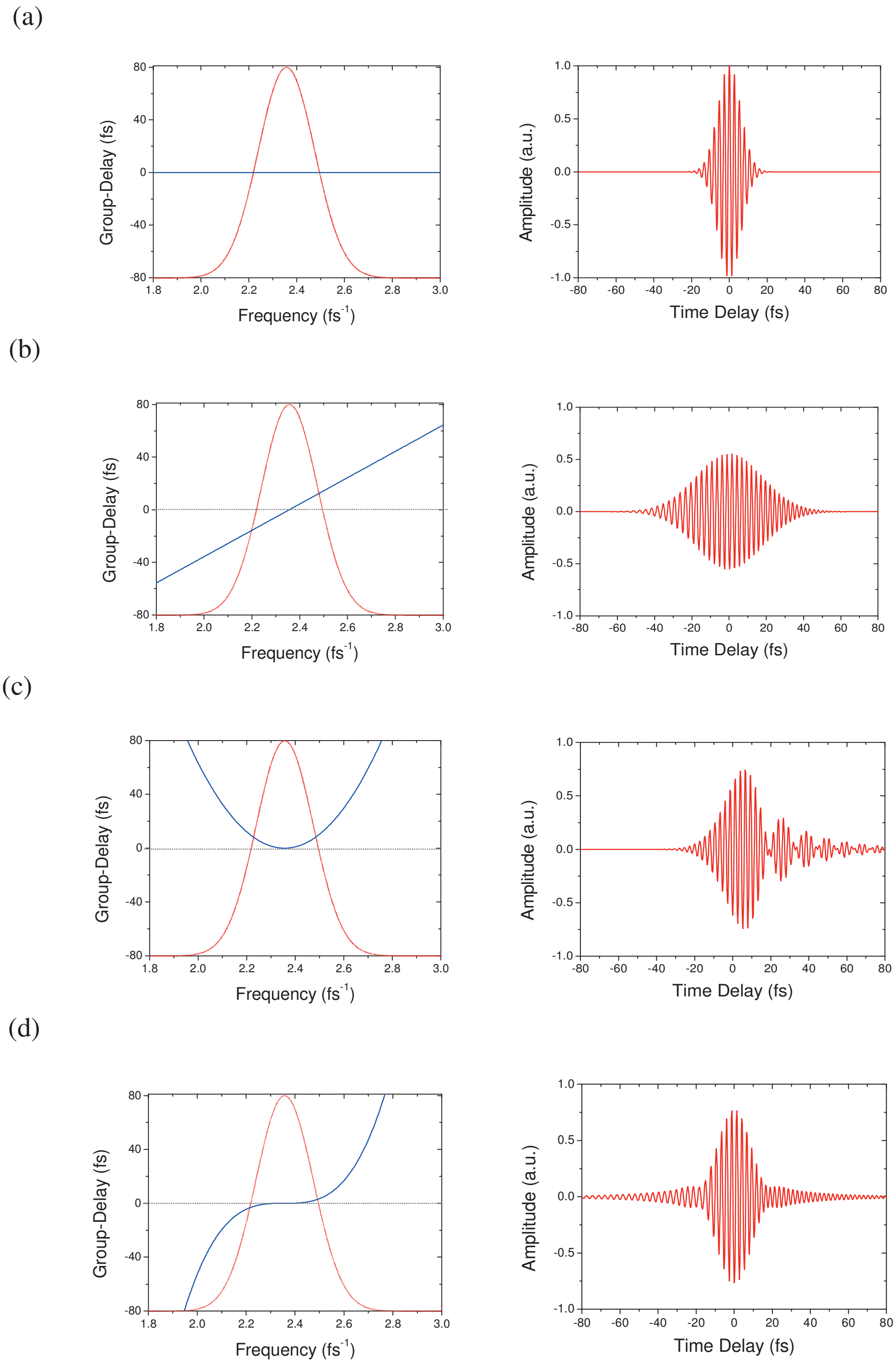

Figure 2.4: Effects of dispersion on the optical wave packet. Gaussian spectra with the group-delay curves and corresponding simulated optical waves are shown. (a): Transform-limited pulse, (b): GDD = 100 fs^2, (c): TOD = 1000 fs^3, and (d): FOD = 7000 fs^4

the introduction of the TOD and the corresponding optical wave. The pulse tail receives the asymmetrical distortion. Finally, the FOD is introduced into the transform-limited pulse (Fig. 2.4 (d)). The pulse pedestal appears in both side of the pulse. Generally, even orders lead to a symmetrical change of the tempral shape and distribute the pulse energy to the pedestal, while odd orders an asymmetrical change of the envelope and the strong modulation of the pedestal. In case of few-cycle pulses, the spectral bandwidth $\Delta\omega$ in Eq. (2.9) becomes so broad that high-order dispersive terms need to be considered. The TOD, FOD, and even higher-order dispersion influence on the pulse duration and its shape as well.

2.5 Pulse characterization

Characterization of optical pulses is usually performed by use of electric devices such as photodiodes and sampling scopes. However, there is no direct electrical method to measure ultrashot optical pulses with a temporal duration in the picosecond- and femtosecond-order. Instead, for the measurement of such ultrashort pulses, the optical pulse itself is used for sampling the waveform. This section introduces several techniques for measuring the temporal pulse duration and pulse shape in interferometric methods. Because each method has its unique advantages, some of these techniques are combined to characterize ultrashort pulses.

2.5.1 Intensity autocorrelation

Intensity autocorrelation is the most common indirect method to estimate the pulse duration by scanning the pulse's intensity versus time. Fig. 2.5 (a) and (b) show the basic optical configuration of the intensity autocorrelation and an example of the measured autocorrelation trace, respectively. In principle, it is a Michelson interferometer, in which one pulse is split into two pulses and they experience different propagation distances due to the arm length difference, and finally they are parallel recombined after the second beam splitter. Because the two pulses are non-collinearly focused at a mutual angle into the thin nonlinear crystal, a measured trace reaches zero intensity at the both wings (background-free trace). The intensity of the second harmonics signal is the convolution of two pulses and written as

$$I(\tau)=\int_{-\infty}^{\infty} I(t)I(t-\tau)dt\,, \tag{2.18}$$

where $I(t)$ and $I(t\text{-}\tau)$ are the intensity of split two pulses, respectively, and τ is the time delay between the two pulses. The nonlinear crystal is designed to have a large second-order nonlinear susceptibility and a broad phase-matching bandwidth. The intensity autocorrelation provides intuitive traces with a simple setup but it gives only limited information on the pulse shape, because the phase information is lost in Eq. (2.18). The second order nonlinearity ensures the symmetry of the autocorrelation trace so that there exist infinitely many symmetric and

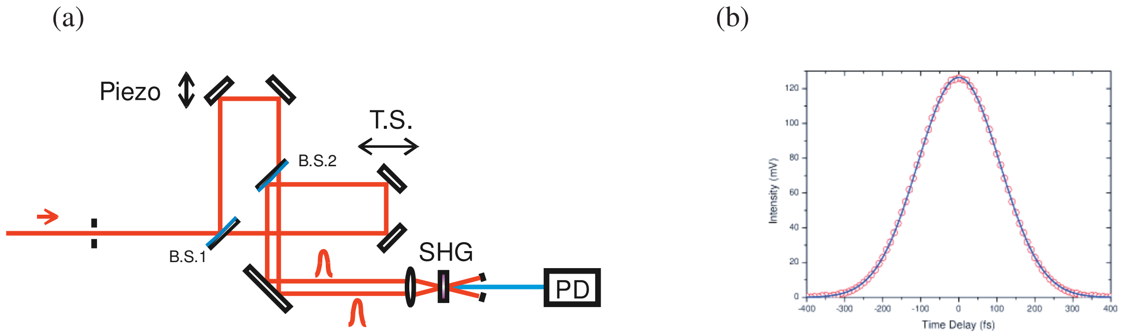

Figure 2.5 (a): Optical layout of the intensity autocorrelator. B.S.: beam splitter, Piezo: piezo actuator for femtosecond pulse, T.S.: translation stage for picoseconds pulse measurement, P.D.: photodiode. A colour filter is set after the crystal to block the fundamental beams. In order to avoid the dispersion, a thin SHG-crystal is used. (b): An example of the measured intensity autocorrelation trace.

asymmetric pulse shapes that lead to very similar symmetric autocorrelation traces. The intensity autocorrelation requires an assumption of the pulse shape. The ratio of the pulse duration with full width at half maximum (FWHM) to the autocorrelation width depends on the pulse shape; e.g. 0.71 for a Gaussian profile and 0.50 for a Lorenzian profile [92].

2.5.2 Fringe-resolved autocorrelation (FRAC)

Fringe-resolved autocorrelation (FRAC) [93-95] reconstructs an optical pulse with an additional spectral data. FRAC is similar to the intensity autocorrelation setup, but with two split beams collinearly focused into the crystal. The signal intensity is written in the following form

$$I_{FRAC}(\tau) = \int_{-\infty}^{\infty} \left| E_1(t) + E_2(t-\tau) \right|^4 dt \ , \tag{2.19}$$

where $E(t)$ is the electric field of one pulse, $E(t - \tau)$ is the electric field of the other pulse, and $I_{FRAC}(\tau)$ is the measured intensity after the nonlinear crystal. The advantage of FRAC compared to intensity autocorrelation is that the original pulse shape can be reconstructed from the FRAC trace with the output spectrum [97]. Fig.2.6 (a)-(c) show simulated FRAC traces of a transform-limited pulse (flat phase), a chirped pulse (positive GDD) and a third-order-phase modulated pulse (positive TOD) for a Gaussian spectrum. As with the intensity autocorrelation trace, FRAC traces are always symmetrical due to the second order nonlinearity, but clearly show modulation caused by the dispersion. GDD leads to pedestals around the main pulse, while TOD induces characteristic nodes in the pedestals. The FRAC trace has the intensity ratio of 0:1:8 between the minimum, the asymptotic level, and the maximum. This ratio is obtained only when the intensities of two interfering beams are strictly equal [96]. Therefore, the 0:1:8 ratio is a good guidance for the proper alignment of the FRAC setup. The FRAC trace shows a clear

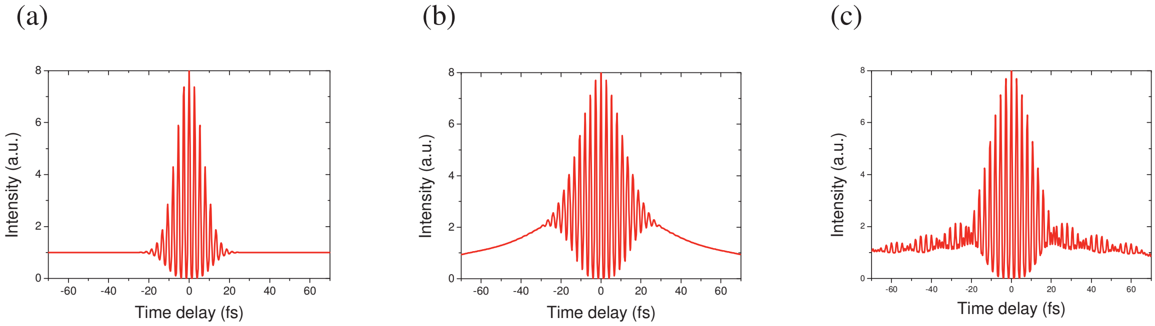

Figure 2.6: Example of simulated FRAC traces. (a): a transform-limited pulse, (b): GDD = 250 fs^2, (c): TOD = 2500 fs^3. The traces have the intensity ratio of 0:1:8 between the minimum, the pedestal, and the maximum.

modulation when the dispersion of only single-order is introduced, but it becomes more complicated in case pulses contain the dispersion with several orders. A novel method referred to as phase and intensity from cross correlation and spectrum only (PICASO) [98] reconstructs the electric field to minimize the error between the measured FRAC with an assumption of a certain phase. However, more complicated high-order phase distortions are difficult to detect using FRAC [83]. The widely used pulse characterization techniques are frequency-resolved optical gating (FROG) and spectral phase interferometry for direct electric field reconstruction (SPIDER).

2.5.3 Frequency Resolved Optical Gating (FROG)

Frequency resolved optical gating (FROG) [99, 100] is a widely used method to measure the spectral phase of optical pulses with a two-dimensional trace by use of a well-developed iterative algorithm. The advantage of FROG over the autocorrelation methods is that an optical pulse is reconstructed without assumption on the phase or pulse shape. Among several types of FROG, second-order harmonics generation FROG (SHG-FROG) is the most popular scheme [96]. The setup of SHG-FROG is same as the intensity autocorrelation, except that a photodiode is replaced with a spectrometer (Fig. 2.7 (a)). The SHG-FROG is more sensitive to the optical pulse than other FROG techniques due to the low-order nonlinearity. The autocorrelation spectrum of the electric field E of the pulse is described as

$$I_{SHG}(\omega,\tau)=\left|\int_{-\infty}^{\infty}E(t)E(t-\tau)e^{-i\omega t}dt\right|^{2} . \tag{2.20}$$

Fig. 2.7 (b) shows an example of a measured SHG-FROG trace. The data is a two-dimensional

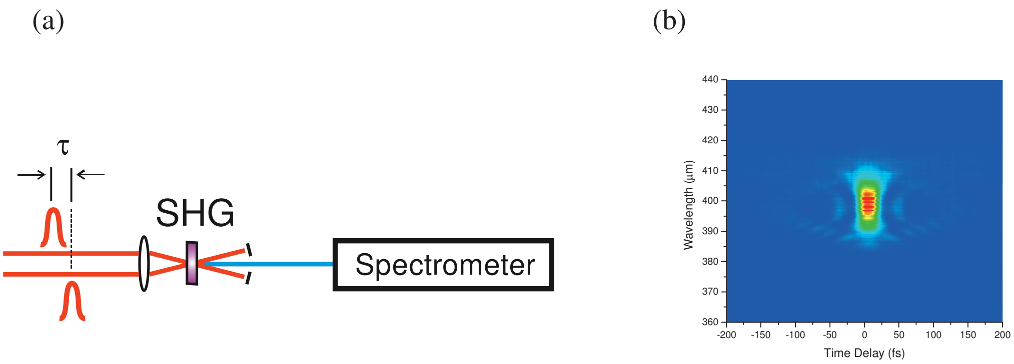

Figure 2.7 (a): SHG-FROG optical layout and (b): an example of a measured SHG-FROG trace. Second harmonics spectrum is scanned for the temporal difference of two pulses. The SHG-FROG trace is always symmetric due to the second nonlinearity.

trace depicted with a second harmonics frequency and the time delay between two identical pulses. The signal intensity is depicted through the colors of a contour plot. Because the SHG-FROG trace is always symmetrical, an ambiguity in the direction of time must be corrected by inserting dispersion-known glass plate [101]. A problem in the fs-pulse measurement is that a large amount of data points is necessary for the measurement of the broad-spectral pulses with a large dispersion. The phase retrieval by use of the iterative Fourier-transform algorithm may result in a long time running and is not suitable for the real-time operation.

2.5.4 Spectral Interferometry for Direct Electric Field Reconstruction (SPIDER)

Spectral phase interferometry for direct electric-field reconstruction (SPIDER) [102] is a single-shot self-referencing interferometric method [103, 104] to provide spectral phase information as well. Because no iterative algorithm is required to reconstruct the phase profile from the measured data, a real-time pulse characterization is possible. In addition, it is suitable for both high- and low-repetition-rate laser sources. This technique is based on the idea of generating two up-converted spectra slightly shifted in frequency and to investigate the spectral interference of these two copies [105, 106]. Fig. 2.8 (a) shows the configuration of the SPIDER apparatus. Two pulse replicas are delayed with respect to one another by τ, and they are frequency mixed with a chirped-pulse in a nonlinear crystal. Each pulse replica is frequency mixed with a different time slice, and hence spectral slice, of the stretched pulse and consequently the up-converted pulses are spectrally sheared. The resulting interferogram is resolved with a spectrometer. A frequency-domain interferogram reflects the relative phase difference between the two arms of the interferometer [107]. If the phase of the pulse travelling in one arm is already known, the task of extracting the relative phase of the pulse propagating in

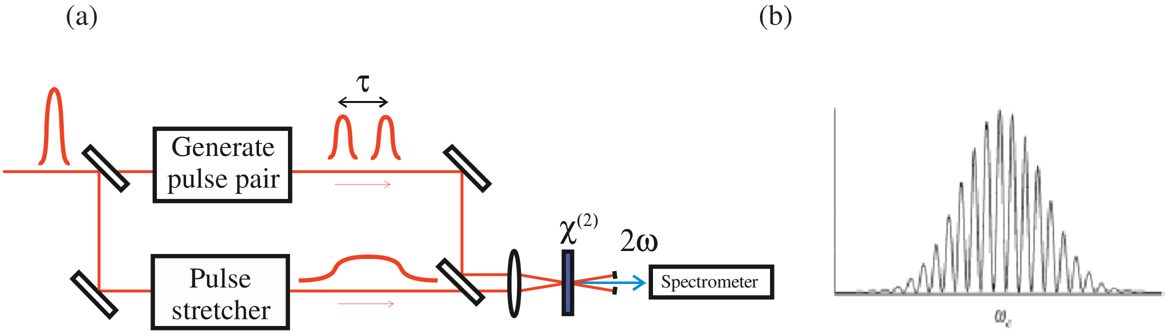

Figure 2.8 (a): SPIDER optical layout [109] and (b): an example of the SPIDER trace [104]. A background-free geometry is assumed where second harmonics is generated only through the interaction of the pulse pair with the stretched pulse.

another arm becomes straightforward. The intensity of the interference for each frequency component is written as [108]

$$I(\omega)=\left|E(\omega)\right|^2+\left|E(\omega+\Omega)\right|^2+2\left|E(\omega)E(\omega+\Omega)\right|\cos\left[\varphi(\omega+\Omega)-\varphi(\omega)+\omega\tau\right]. \tag{2.21}$$

The frequency Ω is the spectral shear, the difference of the carrier frequencies between two pulses. The spectral phase $\varphi(\omega)$ is extracted by calibrating both Ω and τ, which requires a proper and accurate alignment of the system. In Fig. 2.8 (b) an example of the resulting spectral interference pattern of the SPIDER measurement is shown. Because the trace is unintuitive, one needs the phase retrieval for every measurement.

2.5.5 Multi-photon Intrapulse Interference Phase Scan (MIIPS)

Multi-photon intrapulse interference phase scan (MIIPS) is a new technique reported by Dantus *et al* [110, 111]. This technique provides intuitive traces and allows the real-time phase correction without an iterative phase-retrieval algorithm. Multi-photon intrapulse interference (MII) means the interference of the field with itself in the process of multi-photon transition [112]. Because this is the photon interaction in the single beam, the MIIPS technique requires no beam splitter and translation stages. Fig. 2.9 shows the block diagram of MIIPS, in which only a pulse shaper, a thin nonlinear crystal and a spectrometer are used. The intensity of the second harmonics signal after the nonlinear crystal is described by the electric field [113]

$$I^{(2)}(2\omega)=\left|\varepsilon^{(2)}(2\omega)\right|^2 , \tag{2.22}$$

where $\varepsilon(2\omega)$ is the frequency-doubled electric field produced by second harmonic generation. The second harmonics electric field in the frequency domain can be expressed as the

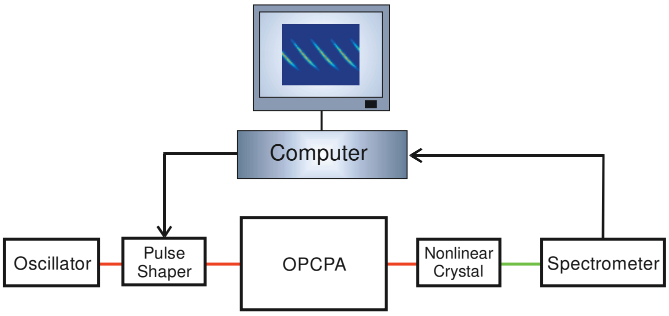

Figure 2.9: Experimental setup for the MIIPS measurement. Amplified pulses from the OPCPA system are frequency-doubled in the nonlinear crystal and detected by a spectrometer. The measured MIIPS trace is fed back to a pulse shaper. A small amount of dispersion is step by step added to the original phase.

convolution of $\varepsilon(2\omega)$ with itself. By introducing integration variables Ω, the convolution integral can be written in the form of

$$\begin{aligned}\varepsilon^{(2)}(2\omega) &= \int \varepsilon(\omega')\varepsilon(2\omega-\omega')d\omega' \\ &= \int \varepsilon(\omega+\Omega)\varepsilon(\omega-\Omega)d\Omega \\ &= \int E(\omega+\Omega)E(\omega-\Omega)e^{i[\phi(\omega+\Omega)+\phi(\omega-\Omega)]}d\Omega. \end{aligned} \tag{2.23}$$

Then the intensity is described by

$$I^{(2)}(2\omega) = \left| \int E(\omega+\Omega)E(\omega-\Omega)e^{i[\phi(\omega+\Omega)+\phi(\omega-\Omega)]}d\Omega \right|^2. \tag{2.24}$$

Eq. (2.24) is maximized when the phase satisfies $\phi(\omega+\Omega) + \phi(\omega-\Omega) = 0$ [113]. The equation is expanded in Taylor series and written in the form of

$$\begin{aligned}\phi(\omega+\Omega)+\phi(\omega-\Omega) &= \phi(\omega)+\phi'(\omega)\Omega+\frac{1}{2}\phi''(\omega)\Omega^2+\frac{1}{6}\phi'''(\omega)\Omega^3+\cdots \\ &\quad +\phi(\omega)-\phi'(\omega)\Omega+\frac{1}{2}\phi''(\omega)\Omega^2-\frac{1}{6}\phi'''(\omega)\Omega^3+\cdots \\ &= 2\phi(\omega)+\phi''(\omega)\Omega^2+\cdots+\frac{2}{(2n)!}\phi^{(2n)}(\omega)\Omega^{2n}, \end{aligned} \tag{2.25}$$

where odd-number-order derivative terms $\phi^{(2n+1)}$ vanish when $\phi(\omega+\Omega)$ and $\phi(\omega-\Omega)$ are added. This equation is minimized for all Ω when $\phi''(\omega) = 0$ because the following higher order derivative terms become zero. When the spectral phase $\phi(\omega)$ is the summation of the original phase $\Phi(\omega)$ and the known phase $f(\omega)$, i.e.

$$\phi(\omega) = \Phi(\omega) + f(\omega). \tag{2.26}$$

The second harmonics spectrum obtains a peak value at the frequency where the condition $\phi''(\omega) = \Phi''(\omega) + f''(\omega) = 0$ is satisfied. The second derivative of the unknown phase $\Phi''(\omega)$ is then described as

$$\Phi''(\omega) = -f''(\omega). \tag{2.27}$$

Once the MIIPS trace is optimized, the phase is analytically retrieved by doubly integrating the second derivative of the original phase of Eq. (2.27) in the frequency domain:

$$\Phi(\omega) = -\iint \Phi''(\omega) d\omega . \tag{2.28}$$

Usually a sinusoidal function is introduced as a reference function $f(\omega)$ because its second derivative is a sinusoidal function as well [114]. The new phase function is then written in the form of

$$f(\delta,\omega) = \alpha \sin(\gamma(\omega-\omega_0)-\delta) \ , \tag{2.29}$$

where α is the amplitude of the function, γ decides the frequency of the sinusoidal wave, ω_0 is the central wavelength to be characterized, and δ is the phase shift. α, γ and ω_0 are fixed parameters, while δ is a scanning parameter. From the Eq. (2.29), the retrieved second derivative of the measured phase function is shown [114]

$$\Phi''(\omega) = \alpha\gamma^2 \sin(\gamma(\omega-\omega_0)-\delta_{\max}(\omega)). \tag{2.30}$$

There are multiple solutions of Eq. (2.30) for the scanning parameter $\delta_{\max}$. The MIIPS trace is obtained by recording the second harmonics spectrum as a function of the scanning parameter. After the phase characterization a small amount of phase is added to the original phase by use of a pulse shaper. The measured spectral phase is then the accumulation of the real-time and iterative operation of the MIIPS measurement, i.e.

$$\Phi_{measured} = \Phi_1 + \Phi_2 + \Phi_3 + \cdots + \Phi_N . \tag{2.31}$$

Finally, the transform-limited pulse is obtained.

CHAPTER 3

Non-collinear OPCPA

Theoretical considerations for the traveling optical wave in the non-collinear parametric amplifier system are given in this chapter. The dynamics of the amplification process is first predicted under the small signal approximation. The simulation results prove the sensitivity of the non-collinear angle, the phase-matching angle, the crystal thickness, and the pump intensity to the gain spectrum. Then output performances on account of the pump depletion are numerically simulated by use of modified coupled-wave equations, in which the non-collinear angle and pump walk-off are taken into account. A two-stage OPCPA simulation reveals the spectral narrowing at the first stage and the back-conversion after the saturation at the second stage. The amplified output is evaluated by introducing the energy-band product (EBP).

3.1 Choice of nonlinear crystal

The choice of the nonlinear crystal is the first step in the OPCPA construction. The following properties should be considered in the choice of a nonlinear crystal.

- **Nonlinear optical coefficient:** A large nonlinear optical coefficient provides a large amount of the gain, which leads to an efficient energy conversion from the pump to signal

- **Damage threshold:** The damage threshold limits the pump intensity and restricts the gain amount and the gain bandwidth. A high damage threshold is therefore desired.

- **Transparency range:** Nonlinear crystals possessing a large transparency rage including the spectral region for the pump and idler wave are desired. For example, the crystal is required to have the transparency for the signal (from 700 nm to 1.0 μm) and the corresponding idler (from 1.2 μm to 2.0 μm), when pumped by 532 nm wavelength. The absorption would result in a reduced parametric amplification [115].

- **Phase-matching bandwidth:** The phase-matching bandwidth should cover the spectrum of the Ti:sapphire spectrum (from 700 nm to 1000 nm), otherwise the amplified spectral bandwidth is restricted by the cut-off of the signal spectrum.

- **Walk-off angle and beam-acceptance angle:** A small walk-off angle ensures a long interaction length and a large acceptance angle allows an easy operation of the phase-matching. A small birefringence results in a small walk-off and a large beam-acceptance.

These requirements restrict the nonlinear crystals to the borate-group crystals such as barium-borate (BBO), bismuth-borate (BiBO), and lithium-triborate (LBO). These crystals have advantages in high nonlinear coefficients, high damage thresholds, and wide transparency ranges [116]. Among these crystals, the BBO and BiBO crystal are great candidate because they have much higher nonlinear coefficients than that of the LBO crystal (BBO: 2.2 pm/V BiBO: 3.2 pm/V, LBO: 0.85 pm/V at the wavelength of 532 nm [116, 117]). Besides, the gain spectra for BBO and BiBO (> 700 nm) overlap with the Ti:sapphire spectrum (from 700 nm to 1.0 μm) better than the LBO spectrum(> 750 nm) [120]. When pumped at 532 nm, the non-collinear angle of BBO optimized at 755-nm signal wavelength is around 2.24^o, while that of BiBO around 3.6^o [117-119]. Because of its small non-collinear angle, the BBO crystal is finally chosen as an amplifier medium. The damage threshold for the BBO crystal is about 7.0 GW/cm^2 with 250-ps pump pulse [121]. This high damage threshold allows an amplification with an intense pump laser to provide a broadband gain bandwidth. The BBO crystal has a transparency ranging from 190 nm to 3.5 μm. In following sections, the BBO crystal is considered as an amplifier medium in OPCPA.

3.2 Phase-matching condition

In the three-wave mixing process, a pump photon, a signal photon and an idler photon satisfy the condition of the energy conservation that

$$\omega_s + \omega_i = \omega_p \ , \tag{3.1}$$

where ω_s, ω_i, ω_p are angular frequencies of signal, idler, and pump pulses, respectively. In the OPA process, because the energy gap between a pump and a signal photon is emitted as an idler photon, there is no heat deposition in the crystal. A high conversion efficiency or quantum efficiency requires a phase-matching among three waves. The phase-mismatch is written in the form of

$$\Delta k = \overrightarrow{k_p} - \overrightarrow{k_s} + \overrightarrow{k_i} = 0 \ , \tag{3.2}$$

where k (= $n(\omega)\omega/c_0$) denotes the wave number and $\overrightarrow{k_s}$,$\overrightarrow{k_i}$,$\overrightarrow{k_p}$ are the wave vectors of signal,

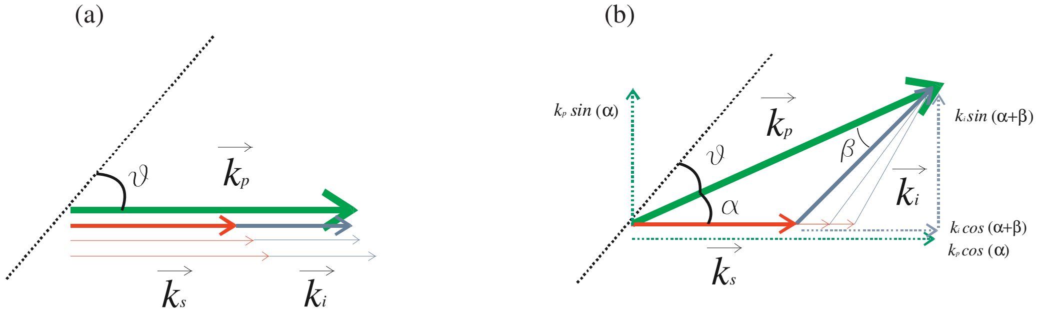

Figure 3.1: Phase-matching condition (a): in collinear and (b): in non-collinear geometry. The wave vectors of the pump ($\vec{k}_p$), signal ($\vec{k}_s$) and idler ($\vec{k}_i$) are shown. The phase-matching angle θ is defined as the angle between the optical axis and pump propagation direction. The non-collinear angle α is defined as the pump tilting from the signal beam.

idler, and pump pulses, respectively. The energy is efficiently transferred from the pump wave to the signal wave in the medium when the phase-mismatch is zero ($\Delta k = 0$). Even though the phase-mismatch is not zero, the signal wave is still amplified within the propagation length of $l < \pi/\Delta k$ (coherece length), but it causes a drop in conversion efficiency. The phase-mismatch is therefore desired to be as small as possible. Fig. 3.1 shows the beam geometries in the amplifier medium. The collinear geometry (Fig. 3.1 (a)) is a quite simple configuration, where the pump, signal, and idler beam propagate in the same direction. This geometry is, however, not suitable for the broadband amplification due to the dispersive properties of the nonlinear amplifier medium [122]. There are several techniques to achieve the phase-matching in a wide spectral range such as a temperature-controlled phase-matching [123, 124], a quasi-phase-matching [125, 126] and an angle-tuned phase-matching [127]. Among these techniques, the angle-tuned phase-matching is an easy and a widely used method to optimize the phase-matching condition. A nonlinear crystal possesses two different refractive indices for different optical polarizations. We consider a negatively uni-axial type-I phase-matching nonlinear crystal ($o + o \rightarrow e$). In non-collinear geometry (Fig. 3.1 (b)), the signal and the pump beam pass through the crystal under a small angle α. The broadband amplification in non-collinear geometry originates from a new freedom of the idler beam direction. The idler-beam direction β is automatically aligned to minimize the phase-mismatching [128, 129], while the non-collinear angle α and the phase-matching angle θ need a strict optimization. In the following subsections, the non-collinear angle and the phase-matching angle are evaluated.

3.2.1 Non-collinear angle and phase-matching angle

For the evaluation of the non-collinear angle α, the phase-mismatch is Taylor expanded and the first order coefficient is set to zero. The vector representation separates Eq. (3.2) into two components parallel and perpendicular to the signal beam direction:

$$\Delta k_{//} = k_p \cos(\alpha) - k_s - k_i \cos(\alpha + \beta) \tag{3.3}$$

$$\Delta k_{\perp} = k_p \sin(\alpha) - k_i \sin(\alpha + \beta) \ . \tag{3.4}$$

The first-order phase-mismatch is written in the form of

$$\frac{\partial \Delta k_{//}}{\partial \omega_s} = -\cos(\alpha+\beta)\frac{\partial k_i}{\partial \omega_s} + k_i \sin(\alpha+\beta)\frac{\partial \beta}{\partial \omega_s} - \frac{\partial k_s}{\partial \omega_s} \tag{3.5}$$

$$\frac{\partial \Delta k_{\perp}}{\partial \omega_s} = -\sin(\alpha+\beta)\frac{\partial k_i}{\partial \omega_s} - k_i \cos(\alpha+\beta)\frac{\partial \beta}{\partial \omega_s} \ , \tag{3.6}$$

where the derivative of the pump wave vector is set to zero with assumptions of the monochromatic pump wave ($dk_p/d\omega_s = 0$), and the zero-angular-dispersion of the non-collinear angle α ($d\alpha/d\omega_s = 0$). Both components can be neglected simultaneously by a proper choice of $\alpha+\beta$ [83]. Multiplying cos ($\alpha+\beta$) by (3.5) and sin ($\alpha+\beta$) by (3.6), and then adding them together, one can obtain the following equation:

$$\frac{\partial k_s}{\partial \omega_s}\cos\left(\alpha+\beta\right) + \frac{\partial k_i}{\partial \omega_s} = 0 . \tag{3.7}$$

The group velocity of the signal and idler waves at the central angular frequency are calculated in the form of [120]

$$\frac{\partial k_i}{\partial \omega_s} = \frac{\partial \omega_i}{\partial \omega_s}\frac{\partial k_i}{\partial \omega_i} = \frac{\partial(\omega_p - \omega_s)}{\partial \omega_s}\frac{\partial k_i}{\partial \omega_i} = -\frac{\partial k_i}{\partial \omega_i} \ . \tag{3.8}$$

Eq. (3.7) is then rewritten in the form of

$$\upsilon_{gi}\cos\left(\alpha+\beta\right) = \upsilon_{gs} \ , \qquad \text{where} \qquad \upsilon_g = \frac{\partial \omega}{\partial k} \ . \tag{3.9}$$

It turns out from this equation that the first-order phase-mismatch is minimized when group velocity of the idler wave is same as that of the signal wave in the signal propagation direction. In collinear geometry ($\alpha = \beta = 0$), the group-velocity matching condition is satisfied only when $\upsilon_{gs} = \upsilon_{gi}$, which is only satisfied at the degeneracy [130]. The introduction of the non-collinear angle α enables the group-velocity matching in the direction of the signal beam at different wavelengths. Non-collinear angles and the corresponding wavelengths, at which both the phase-matching and the group-velocity matching are satisfied, are calculated from the following two conditions:

$$\upsilon_{gs} = \upsilon_{gi}\cos(\alpha+\beta) \tag{3.10}$$

$$k_p \sin\alpha = k_i \sin(\alpha+\beta) \ . \tag{3.11}$$

The optimum non-collinear angle is written in the form of [131]

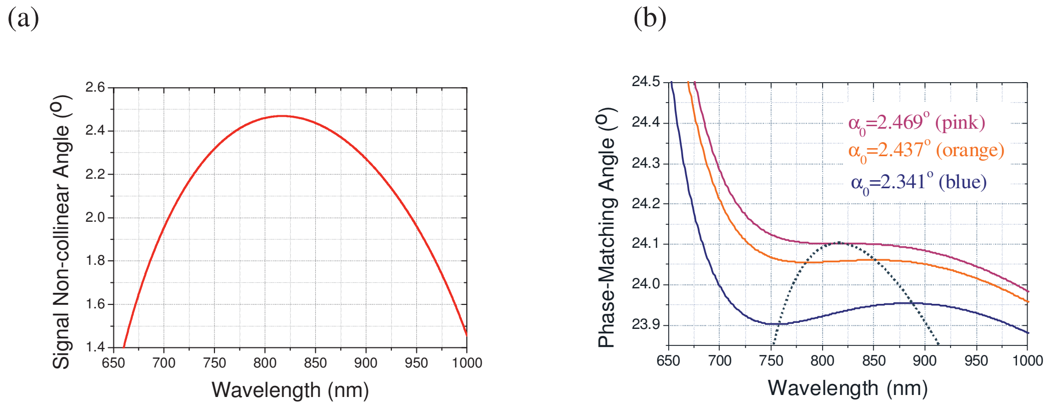

Figure 3.2 (a): Non-collinear angle of a type-I phase-matching BBO crystal at a pump wavelength of 526 nm. The group-velocity matching condition is satisfied in two seed wavelengths except for 2.46°. (b): Phase-matching angle as a function of a signal wavelength for three different non-collinear angles optimized at 755nm, 850 nm, and 825 nm. Dashed line indicates the wavelengths where a group-velocity matching condition between a signal and an idler pulse is satisfied. These simulations follow the approach of J. Zheng *et al.* [132].

$$\alpha = \sin^{-1}\left(\sqrt{\frac{1-(\upsilon_s/\upsilon_i)^2}{1+2\upsilon_s n_s \omega_s / \upsilon_i n_i \omega_i + (n_s \omega_s / n_i \omega_i)^2}}\right) \ . \tag{3.12}$$

Eq. (3.12) is derived from Eqs. (3.10) and (3.11) (See Appendix A). The calculation result for the optimum non-collinear angle at 526-nm pump wavelength is plotted in Fig. 3.2 (a). The trace shows a parabolic dependence on the wavelength and there exist two different signal wavelengths, at which both phase-matching and group-velocity matching condition are fulfilled [132]. Fig. 3.2 (b) shows phase-matching curves for different non-collinear angles with a pump wavelength of 526 nm. The phase-matching angle θ, and therefore the pump wave vector $k_p(\theta)$, is determined from Eqs. (3.3) and (3.4) on condition that both components are zero ($\Delta k_{||} = \Delta k_{\perp} = 0$). The calculation is carried out for three different non-collinear angles α of 2.341° (optimized at 755 nm), 2.437° (optimized at 850 nm), and 2.469° (optimized at 825 nm). The dashed line plots signal wavelengths at which the group-velocity matching between the signal and idler is satisfied, i.e. flat phase-matching curves are obtained at the wavelength. However, this figure shows the limitation of the phase-matching bandwidth due to the shape of the phase-matching curves. In the following section, the spectral gain is simulated at various phase-matching conditions at the optimum wavelength of 755 nm.

3.2.2 Gain simulation with various phase-matching conditions

Because of the narrower beam acceptance angle of the type-I BBO crystal than that of LBO, the strict and careful optimization of the phase-matching angle and the non-collinear angle are

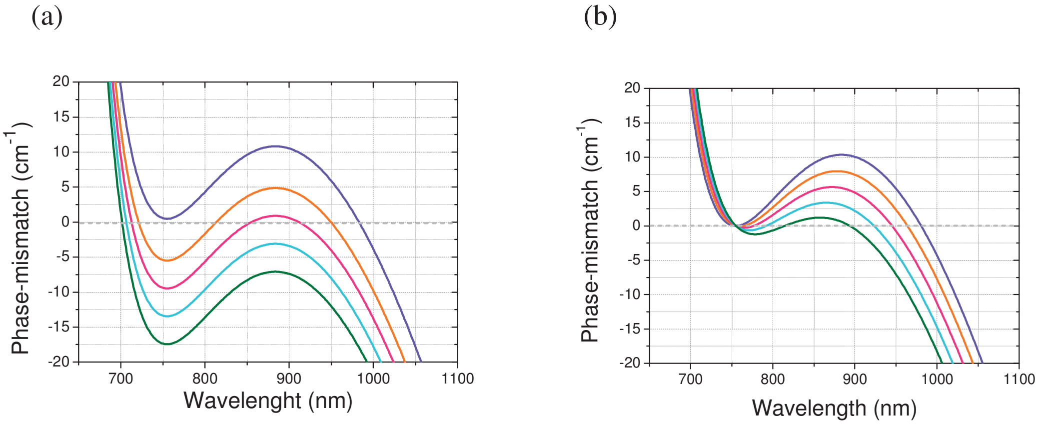

Figure 3.3 (a): Wavelength-dependent phase-mismatch for various phase-matching angles. The initial phase-matching angle is $\theta_0 = 23.90^{\circ}$ and its value is step by step increased at the interval of $\Delta\theta = +0.02^{\circ}$. (b): Wavelength-dependent phase-mismatch for different non-collinear angles, while the phase matching optimized at the signal wavelength of 755 nm. The initial non-collinear angle is $\alpha_0 = 2.341^{\circ}$ and the angle is varied at the interval of $\Delta\alpha = +0.02^{\circ}$.

required. In this section, the sensitivity of the non-collinear angle and the phase-matching angle to the signal gain spectrum is investigated. Fig. 3.3 (a) and (b) plot the variations of the phase-mismatch for different phase-matching angles and for different non-collinear angles, respectively. Fig. 3.3 (a) shows variations of the phase-matching angle and Fig. 3.3 (b) shows variations of the non-collinear angle. The phase-mismatch curve shifts parallel by tuning the phase-matching angle, while the entire curve is rotated by introducing the non-collinear angle change. Note that in Fig. 3.3 (b) the phase-matching angle must be optimized for each non-collinear angle to obtain a zero phase-mismatch at the wavelength of 755 nm. There are several reports on the gain simulation for the NOPA process, based on the small-signal approximation [128, 133-136]. With this approximation, the gain G is analytically derived from the coupled-wave equations under the condition of the flat-top pump pulse, zero pump depletion, and a small walk-off angle ρ. The gain is expressed as [133]

$$G = 1 + (gL)^2 \left(\frac{\sinh(\alpha)}{\alpha}\right)^2 , \tag{3.13}$$

where L is the interaction length in a nonlinear crystal. The phase-matching coefficient α and the gain coefficient g are written as

$$\alpha = \sqrt{(gL)^2 - \left(\frac{\Delta kL}{2}\right)^2} \qquad \text{and} \qquad g = 4\pi d_{eff} \sqrt{\frac{I_p}{2\varepsilon_0 n_p n_s n_i c \lambda_s \lambda_i}} , \tag{3.14}$$

where $\Delta kL = (\vec{k}_p - \vec{k}_s - \vec{k}_i)_s L$ is the phase mismatch in the direction of the signal propagation, d_{eff} is

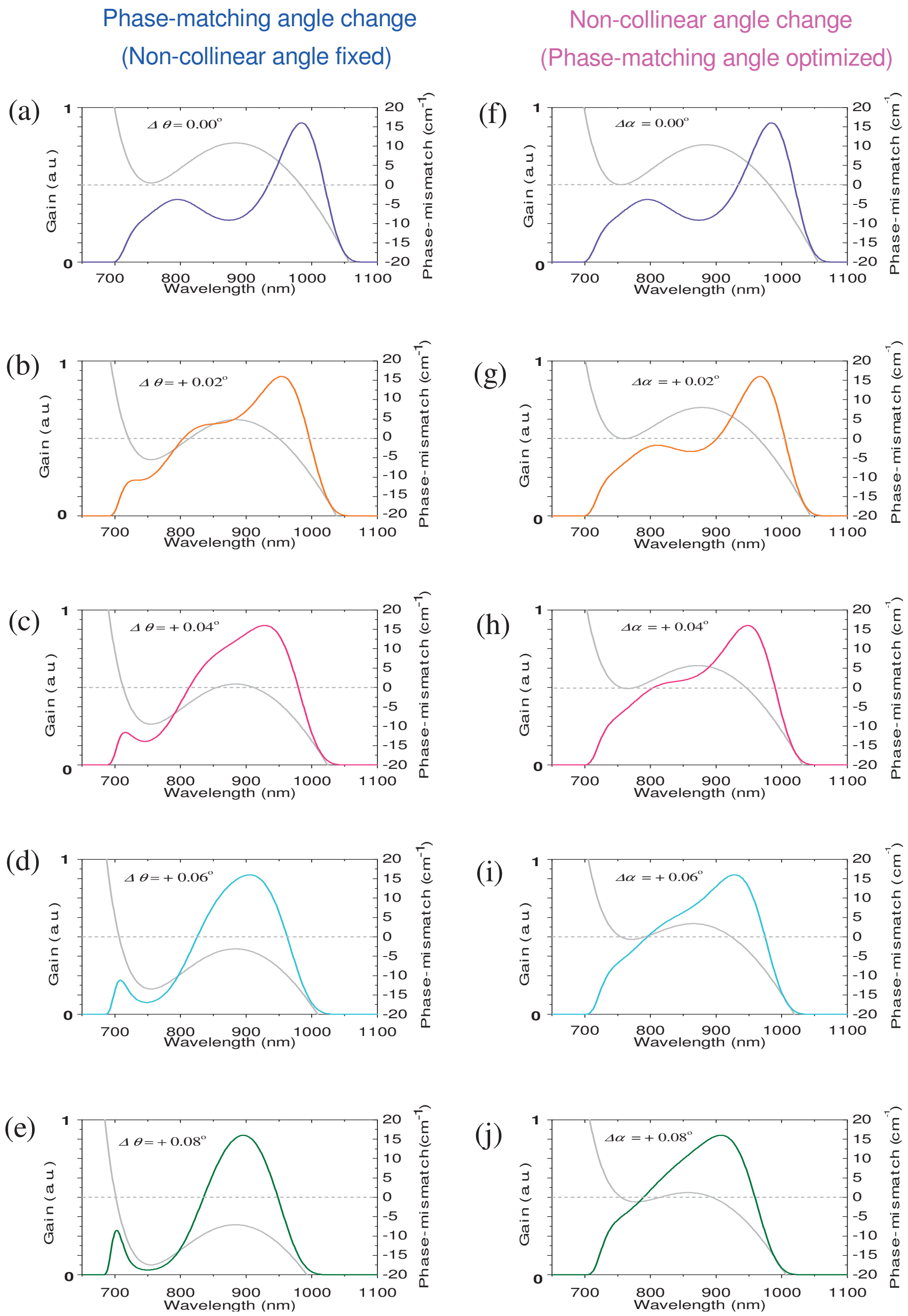

Fig. 3.4: Numerical simulations of the gain spectra in a small signal regime. (a)-(e): Gain spectra with various phase-matching angles at a fixed non-collinear angle of 2.341°. (f)-(j): Gain spectra with various non-collinear angles at the optimized phase-matching angle at a wavelength of 755 nm. The dashed horizontal line indicates zero phase mismatch.

the effective second order nonlinear coefficient of the nonlinear crystal, I_p is the pump intensity, and c is the velocity of light in vacuum. The gain sensitivity to these two angles is simulated by use of Eq. (3.13). The configuration is first optimized at 755-nm signal wavelength.

The simulations are performed by setting a crystal length of 5.0 mm with a 526-nm pump wave focused at 7.75-GW/cm^2 intensity. Fig. 3.4 (a)-(e) show the simulation results for normalized gain spectra and corresponding phase-mismatch curves at various phase-matching angles. The non-collinear angle is set at $\alpha_0 = 2.341^{\circ}$, where the group-velocity matching condition is satisfied at 755 nm (See Fig. 3.2 (a)). A broadband gain ranging from 700 nm to 1050 nm is obtained due to the flat and small phase-mismatch at 755 nm (Fig 3.4 (a)). The phase-matching angle is changed around $\theta_0 = 23.9^{\circ}$ at intervals of 0.02°. The shape and bandwidth of the gain spectrum sensitively vary with such a small change of the phase matching angle. Besides, with increasing the phase-matching angle ((b): $\theta_0 + 0.02^{\circ}$, (c): $\theta_0 + 0.04^{\circ}$, (d): $\theta_0 + 0.06^{\circ}$, (e): $\theta_0 + 0.08^{\circ}$), the amplified gain spectrum is shift to shorter wavelengths. The simulation results for the various non-collinear angles with the optimized phase-matching angle at the wavelength of 755 nm are shown in Fig. 3.4 (f)-(j), where the normalized gain spectra and corresponding phase-mismatch curves are plotted. The non-collinear angle is initially set at 2.341° and is gradually increased at intervals of 0.02°. This simulation reveals that the gain spectrum is narrowing but becomes smooth with the increase of the non-collinear angle. This result owes to the narrow but flat phase-mismatching curve around the wavelength of 755 nm.

In summary, the sensitivity of the BBO crystal to the phase-mismatch has been quantitatively analyzed through the gain simulation in a small signal approximation. The simulation results have shown the strong effect of the phase-mismatch on the parametric amplification process.

3.2.3 Gain simulation with various pump intensities and thicknesses

This section provides the simulation results on the pump-intensity and the crystal-thickness dependence on the gain spectrum. Ideally, a high pump intensity and a long crystal thickness seem to be desirable for a high output power. However, the pump intensity is restricted by the damage threshold and the signal is only amplified within the coherence length. The gain spectra for several crystal lengths under a small gain regime are simulated by use of Eq. (3.13). This equation can be simplified with an assumption of zero phase-mismatch ($\Delta k = 0$) to $G = sinh^2 (gL)$, where the same gain is obtained on condition that gL ($\propto I^{1/2}L$) is constant [120]. For example, if the pump intensity becomes 1/10 of the original intensity, the same gain amount can be obtained by increasing the crystal thickness by $10^{1/2}$ (= 3.16) times. Gain spectra are simulated for three different pump intensities with corresponding crystal thicknesses chosen to satisfy the constant gain ($I^{1/2}L$ = const.). Fig. 3.5 shows the calculation results of gain spectra for the pump intensities of 12.1 GW/cm^2 (orange line), 7.75 GW/cm^2 (pink line), and 5.38 GW/cm^2 (blue line) with the corresponding crystal thicknesses of 4.0 mm, 5.0 mm, and 6.0 mm,

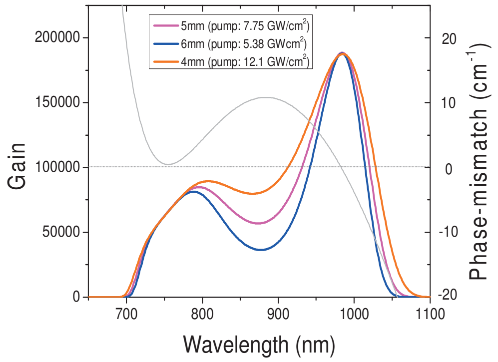

Figure 3.5: OPA gain spectra for the pump intensities of 12.1 GW/cm^2 (orange), 7.75 GW/cm^2 (pink), and 5.38 GW/cm^2 (blue) with the crystal lengths of 4.0 mm, 5.0 mm, and 6.0 mm, respectively ($I^{1/2}L$ is set to be constant). The phase-matching condition is optimized at 755 nm ($\alpha = 2.341^\circ$ and $\theta = 23.92^\circ$).

respectively. The non-collinear and phase-matching angles are optimized at 755 nm. The phase-mismatch curve is also shown in this figure (gray line). Each wavelength component is exponentially amplified in the nonlinear medium. The exact phase-matching is satisfied at two wavelengths, where three spectra show the equal gain values. It turns out from this figure that the gain and amplified bandwidth sensitively depend on both the pump intensity and the crystal thickness. A high-pump-intensity (12.1 GW/cm^2) with a short crystal length (4.0-mm thick) prevents the phase-mismatch accumulated in the crystal and therefore realizes a broader gain spectrum. On the other hand, a low pump intensity (5.38 GW/cm^2) with a long crystal length (6.0-mm thick) causes a modulation in the gain spectrum and a deep suppression of the gain growth except for the two wavelengths where the phase-matching condition is satisfied. The spectral gain distortion caused by the phase-mismatch becomes vital when a signal spectrum is broadband. It is thus better to use a thin crystal with a high intensity, although the pump intensity is limited by the damage threshold of the crystal. Besides, the accumulation of the phase-mismatch should be prevented.

3.3 Coupled-wave equations in non-collinear OPCPA

In this section, modified coupled-wave equations are introduced to describe the parametric three-wave interaction in broadband non-collinear OPCPA. The conventional numerical analyses of the parametric amplification have been based on the collinear OPA model, where the non-collinear angle α is very small for simplicity [129, 137-139]. However, when the gain spectrum is broad enough to support few-cycle pulses, the variation of the angle β must be taken into account and the effect of the dispersion in the crystal cannot be ignored. Fig. 3.6 (a)

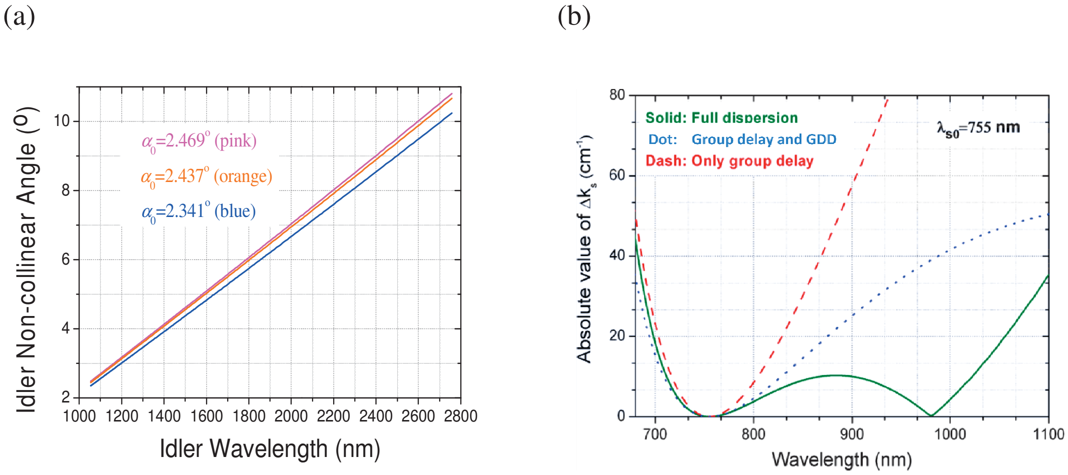

Figure 3.6 (a): Idler-wavelength dependent angle β for three different non-collinear angles ($\alpha =$ 2.341°, 2.437°, and 2.469°). BBO crystal with a type-I phase-matching is pumped at 526 nm. (b): Simulated spectral phase-mismatch with the group-delay only, the group-delay and GDD expanded at 755 nm, and the full dispersion [132].

shows the variation of the angle β as a function of the idler wavelength from 1008 nm to 2757 nm (corresponding signal wavelength from 650 nm to 1100 nm) at the pump wavelength of 526 nm. The non-collinear angle is optimized at the signal wavelength of 755 nm ($\alpha = 2.341^{\text{o}}$), 850 nm ($\alpha = 2.437^{\text{o}}$), and 825 nm ($\alpha = 2.469^{\text{o}}$). The figure shows the strong dependence of the angle β on its wavelength [132]. The dispersion in the crystal must be also considered when the acceptance bandwidth of OPA is broad. Fig. 3.6 (b) shows the simulated spectral phase-mismatch with the consideration of group-delay (GD) only, GD and group-delay dispersion (GDD) only, and full dispersion optimized at 755-nm signal wavelength [132]. The conventional coupled-wave equations take only GD [136] or up to GDD [134] into account. The figure shows that the phase information obtained from a dispersion approximation up to GD or GDD is valid only for a narrow spectral range. It is therefore necessary to improve the model to be suitable for the description of the parametric process in non-collinear OPCPA. J. Zheng *et al.* has given some modification to the conventional collinear model to correctly describe the non-collinear OPCPA and derived the following equations for the pump, signal, and idler [132]:

$$\frac{\partial \tilde{E}_p}{\partial z} + ik_p \cos(\alpha)\tilde{E}_p = -i\frac{\chi^{(2)}\omega_p}{n_p c_0 \cos(\alpha)}\frac{1}{\cos^2(\rho+\alpha)}F\{\tilde{E}_i(t)\tilde{E}_s(t)\} \tag{3.15}$$

$$\frac{\partial \tilde{E}_s}{\partial z} + ik_s \tilde{E}_s = -i\frac{\chi^{(2)}\omega_s}{n_s c_0}F\{\tilde{E}_p(t)\tilde{E}_i^*(t)\} \tag{3.16}$$

$$\frac{\partial \tilde{E}_i}{\partial z} + ik_i \cos[\alpha+\beta(\omega_i)]\tilde{E}_i = -i\frac{\chi^{(2)}\omega_i}{n_i c_0 \cos(\alpha+\beta)}F\{\tilde{E}_p(t)\tilde{E}_s^*(t)\} \quad , \tag{3.17}$$

where z is the propagation direction of the signal wave and n_s, n_i, and n_p are the refractive index of signal, idler, and pump. E_s, E_i and E_p are the amplitudes of the electric field of signal, idler, and pump, respectively. The angle ρ in Eq. (3.15) accounts for the pump walk-off. The following are the difference between the modified coupled-wave equations and the conventional ones:

- The non-collinear angle α, the wavelength-dependent idler direction $\beta(\omega)$, and the pump walk-off angle ρ are taken into account. The wave-vector magnitude is precisely presented. In case the non-collinear angle α and walk-off angle ρ have the same sign, the configuration is referred to as walk-off compensation geometry. On the other hand, when the signs of them are different, a tangential phase-matching geometry.

- The full dispersion is taken into account in the new model. By expressing the coupled-wave equations with a Fourier transform, the phase information is automatically included in the right side of the coupled-wave equations.

- 3rd-order nonlinear effects such as self-phase modulation (SPM) and cross-phase modulation (XPM) accompanying the parametric amplification can be easily added into the right side of the coupled-wave equations [132]. Eq. (3.15)-(3.17) are then rewritten in the form of

$$\begin{aligned}\frac{\partial \tilde{E}_p}{\partial z} + ik_p\cos(\alpha)\tilde{E}_p = &-i\frac{\chi^{(2)}\omega_p}{n_p c_0\cos(\alpha)}\frac{1}{\cos^2(\rho+\alpha)}F\{\tilde{E}_i(t)\tilde{E}_s(t)\}\\ &-i\frac{3\chi^{(3)}\omega_p}{2n_p c_0\cos(\alpha)}F\left\{\left[\gamma_{pp}\left|\tilde{E}_p\right|^2+\gamma_{ps}\left|\tilde{E}_s\right|^2+\gamma_{pi}\left|\tilde{E}_i\right|^2\right]\tilde{E}_p\right\}\end{aligned} \tag{3.18}$$

$$\begin{aligned}\frac{\partial \tilde{E}_s}{\partial z} + ik_s\tilde{E}_s = &-i\frac{\chi^{(2)}\omega_s}{n_s c_0}F\{\tilde{E}_p(t)\tilde{E}_i^*(t)\}\\ &-i\frac{3\chi^{(3)}\omega_s}{2n_s c_0}F\left\{\left[\gamma_{ss}\left|\tilde{E}_s\right|^2+\gamma_{sp}\left|\tilde{E}_p\right|^2+\gamma_{si}\left|\tilde{E}_i\right|^2\right]\tilde{E}_s\right\}\end{aligned} \tag{3.19}$$

$$\begin{aligned}\frac{\partial \tilde{E}_i}{\partial z} + ik_i\cos[\alpha+\beta(\omega_i)]\tilde{E}_i = &-i\frac{\chi^{(2)}\omega_i}{n_i c_0\cos(\alpha+\beta)}F\{\tilde{E}_p(t)\tilde{E}_s^*(t)\}\\ &-i\frac{3\chi^{(3)}\omega_i}{2n_i c_0\cos(\alpha+\beta)}F\left\{\left[\gamma_{ii}\left|\tilde{E}_i\right|^2+\gamma_{is}\left|\tilde{E}_s\right|^2+\gamma_{ip}\left|\tilde{E}_p\right|^2\right]\tilde{E}_i\right\}\end{aligned} , \tag{3.20}$$

where the value of γ is dependent on the light polarization. The γ value equals 1 if the optical waves have the same polarization, and it is 1/3 in the other case [128].

3.4 Numerical simulations of two-stage OPCPA

Output performances of the non-collinear OPCPA system are theoretically calculated based on the modified coupled-wave equations. Simulation results for the output of a two-stage OPCPA under various phase-matching conditions, e.g. temporal overlapping, angular sensitivity and influence of pump fluctuations, have been reported in detail by J. Zheng *et al.* [132]. We briefly review the simulation results for the amplified spectra and output energies depending on the propagation distance in an amplifier medium, taking the pump depletion into account. In these simulations, 526-nm, 60-ps Gaussian pump pulses are focused into a crystal with a pump energy of 700 μJ, which corresponds to the intensity of 7.75 GW/cm^2. The signal spectrum to be amplified resembles that of a commercially available source supporting sub-7 fs pulses (Rainbow, Femtolesers). The idler wave is set to zero again at the beginning of the 2nd pass amplification.

3.4.1 Output simulation of two-stage non-collinear OPCPA

We consider the dynamics of a two-stage (5-mm thickness × 2 pass) OPCPA system. The coupled-wave equations are numerically solved with a split-step Fourier-transform algorithm under the plane wave approximation [132]. This algorithm splits the crystal into small sections and calculates the wave propagation in each section in the spectral domain. The nonlinear interaction terms are calculated in the temporal domain with a 4th order Runge-Kutta integration routine. Fig. 3.7 (a) illustrates the numerical results of the signal spectrum depending on the crystal length for non-collinear OPCPA optimized at the signal wavelength of $\lambda_{s0} = 755$ nm. The position from 0 mm to 5.0 mm describes the first stage and that from 5.0 mm to 10 mm the second stage. These results show that the spectrum becomes narrower in the crystal length of 0 mm to 7.5 mm, while it broadens in the crystal length from 7.5 mm to 10 mm. This initial spectral gain narrowing is due to the non-uniform gain distribution caused by the Gaussian temporal profile of the pump pulse. The different spectral components experience different gain, which results in the spectral shape modulation [132]. In order to prevent the spectral narrowing, it is ideal if the pump has a flat temporal profile and the signal has a flat spectral profile. The following spectral broadening results from the back conversion process from the signal topump. The broadened spectrum possesses double peaks, leading to a deterioration of the pulse contrast after the pulse compression. Fig. 3.7 (b) presents the corresponding transform-limited pulse profiles of the spectrum at each crystal position. The transform-limited pulse duration can be a measure to estimate the spectral bandwidth of the distorted spectrum. In the first stage the spectral bandwidth becomes narrower in the crystal, and the transform-limited pulse duration increases as the pulse propagates in the crystal. On the other hand, the spectral broadening after the 7.5-mm crystal position leads to the decreasing of the transform-limited pulse duration, althoug the temporal profile is modulated as a result of the strong back-conversion process.

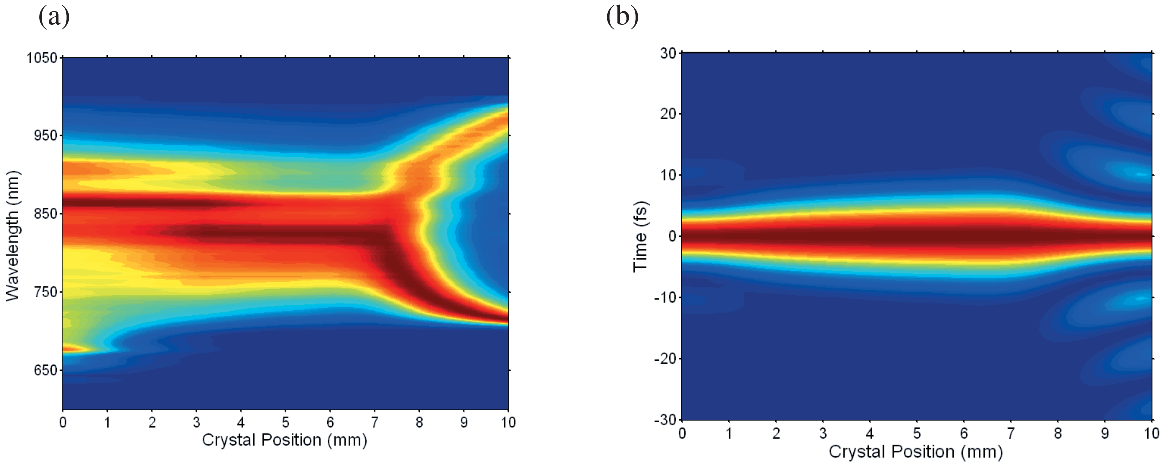

Figure 3.7: Evolution of signal light in the BBO crystal. (a): Signal spectrum dependence on the crystal position. (b): Corresponding Fourier transform-limited pulse profile at each position. The configuration is optimized at $\lambda_{s0} = 755$ nm [141].

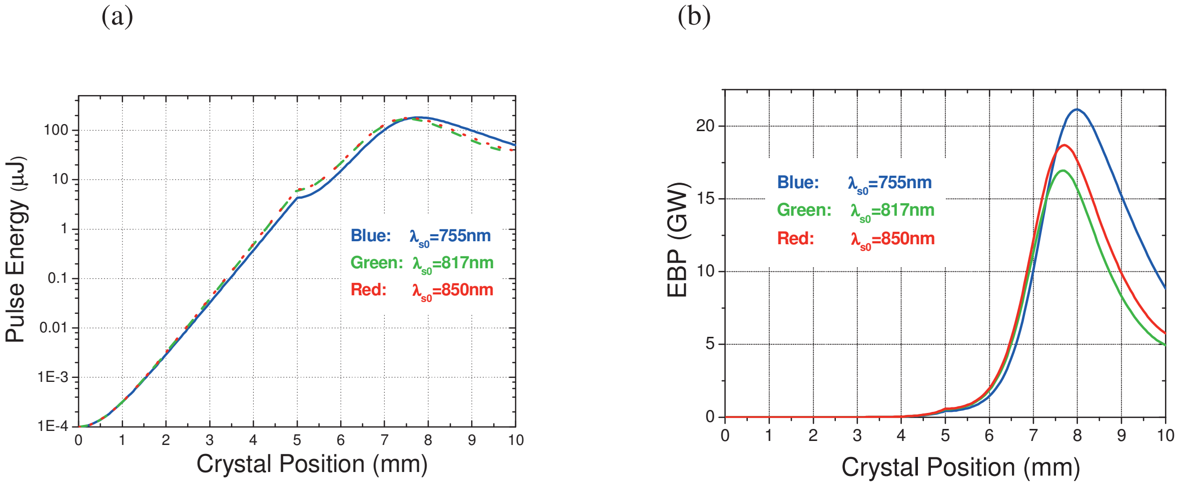

Figure 3.8 (a): Signal pulse energy dependence on the propagation distance in the crystal for three different configurations optimized at $\lambda_{s0} = 755$ nm (blue line), 817 nm (green line), and 850 nm (red line), respectively [132]. (b): Energy-bandwidth product (EBP) inside the crystal for three different configurations optimized at $\lambda = 755$, 817, and 850 nm [132].

The output energy is simulated by use of the modified coupled-wave equations. Fig. 3.8 (a) plots the dependence of the signal pulse energy on the propagation distance inside the crystal for three different configurations optimized at the central wavelength of 755 nm, 817 nm and 850 nm. The signal pulse energy is exponentially increased in the first stage, while the saturation is observed in the second stage. The saturation position weakly depends on the central wavelength. Pulse energies at the saturation position are about 182 μJ (at 7.80-mm crystal length), 170 μJ (at

7.55-mm crystal length) and 178 μJ (at 7.55-mm crystal length) for the central wavelength of 755 nm, 817 nm and 850 nm, respectively. After the saturation, strong back-conversions are observed and the pulse energies decrease rapidly toward the end of the crystal down to 50 μJ. Strong back-conversions observed in all simulations are quite typical in optical parametric processes [132]. It is therefore crucial to correctly choose the crystal length to balance the spectral gain narrowing and the back-conversion process to optimize the output performance of the system. It seems to be one of the best choices to select a nonlinear crystal with a suitable thickness by maximizing the achievable output energy, However, the achievable peak power depends on both the output energy and the transform-limited pulse duration. The energy-band product (EBP) is instead employed as a criterion to examine the performance of the system. EBP is the product of the pulse energy and the frequency-bandwidth, which corresponds to the ratio of the pulse energy to the transform-limited pulse duration. Fig. 3.8 (b) shows the EBP as a function of the crystal thickness. The plots behave similar to the output energy, but the peak positions are slightly later than the plots in Fig. 3.8 (a). Therefore a certain back-conversion results in spectral broadening and is beneficial to obtain ultrashort pulses [129]. It is necessary to control those parameters carefully to optimize the output performance of the whole system. At the pump intensity in these simulations, a 4-mm thickness crystal is expected to balance the gain narrowing and the back-conversion process and the output signal at the end of the second pass.

3.5 Summary

This chapter has presented the numerical simulations for the travelling wave in the non-collinear parametric amplifier system. The simulations aim at optimizing the output performance of the system. The gain-simulation under a small-signal approximation have revealed that the gain is quite sensitive to the non-collinear angle, the phase-matching angle, the crystal thickness and the pump intensity. These parameters must be carefully controlled to optimize the performance of the whole system. The simulation has recommended a high pump intensity below the threshold. The two-stage OPCPA simulation has been shown by use of the modified coupled-wave equations, which is suitable to describe the non-collinear optical parametric interaction. The simulation results have revealed that the amplified spectrum becomes narrower at the initial stage due to the non-uniform gain distribution and broader after the saturation due to the back-conversion process. It is therefore crucial to correctly control the experimental parameters and balance the spectral gain-narrowing and back-conversion process.

CHAPTER 4

Dispersion management in OPCPA

Dispersion management is one of the challenging themes in non-collinear OPCPA. A broadband spectral phase must be precisely controlled, although it is quite sensitive to the dispersion up to high orders. This chapter introduces several dispersive devices and provides the best choice of a stretcher and a compressor to obtain a broad acceptance bandwidth. Our stretcher-compressor scheme shows a large stretching ability and a high transmission through the compressor. Two configurations are tested as a stretcher-compressor design; a conventional TOD/GDD-matching design and a novel global-dispersion-balance design. The latter design successfully expands the tunable spectral range of an adaptive dispersive device by suppressing the residual group delay of the whole system within the working window of the device.

4.1 Calculation of dispersion for different devices

This section introduces several popular devices used for the dispersion management, i.e. a transparent medium, a prism sequence [142], a grating sequence [143], and a grism sequence [144].

4.1.1 Material dispersion

Transparent materials are the simplest dispersive device. Fig. 4.1 (a) illustrates a beam propagating in a glass block cut at an angle θ. The spectral phase in the angularly dispersive transparent medium is described as [145]

$$\phi(\omega) = \frac{\omega l}{c}\sqrt{n(\omega)^2 - \sin^2(\theta_i)}\,, \tag{4.1}$$

where l is the thickness of the transparent medium, $n(\omega)$ is the refractive index, and θ_i is the incident angle. When the incident angle is perpendicular to the glass block ($\theta_i = 0$), the sinusoidal part vanishes and the equation is identified with the familiar spectral phase in materials. The dispersion of each order is derived from the derivative of Eq. (4.1) as mentioned in Eq. (2.9). Fig. 4.1 (b) lists positive or negative signs of each dispersion order for the SF-57 glass in the visible range ($\lambda < 1000$ nm). This list shows that GDD and TOD are positive in this

(a)

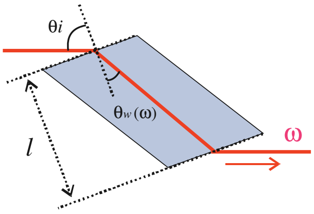

(b)

GVD	+
TOD	+
FOD	+
FiOD	+

Figure 4.1(a): Optical beam path in a glass block. θ_i.: angle of incidence, l: thickness of a transparent medium, $n(\omega)$: frequency-dependent refractive index. (b): Signs for the dispersion of a Brewster-cut SF57 glass block ($\lambda < 1000$ nm).

spectral range. Because the SF-57 glass has a high reflective index, an optical pulse receives a large amount of dispersion with a short propagation. The angular dispersion caused by the refraction at the glass surface is so small that it makes no obvious influence on the signs of the dispersion. The most advantageous property of the glass block as a dispersive device is its high transmission efficiency. When the beam incidents at a Brewster angle, it passes through the material without surface reflections.

4.1.2 Dispersion of prism sequence

A prism sequence is commonly used to compensate small amounts of material dispersion. The configuration of the prism sequence is shown in Fig. 4.2 (a). A beam is diffracted on the surface of the first prism and the each frequency component propagates in a different direction and then the spatially expanded beam is collimated by use of the second prism. The original beam diameter is obtained by using a prism pair in a mirror-imaged geometry. At the angle of Brewster incidence, the energy loss is minimized and a high transmission efficiency is realized after the prism sequence. The negative GDD is introduced via angular dispersion of the prism sequence. The phase of the prism sequence is calculated using simple geometrical optics. The beam direction for each wavelength is defined as $\theta_p\ (\omega)$, the angle between the direction normal to the interior surface and the direction of the beam propagation. $\theta_p(\omega)$ in this figure is written in the form of [145]

$$\theta_p(\omega) = \sin^{-1}\left(n(\omega)\sin\left\{ \alpha - \sin^{-1}\left[\frac{\sin\theta_i}{n(\omega)} \right] \right\} \right) , \tag{4.2}$$

where θ_i is the angle of incidence on the first prism surface, $n(\omega)$ is the refractive index of the prism material, and α is the apex angle. The phase of the prism sequence is described by use of θ_p as

$$\phi(\omega) = \frac{\omega l}{c}\cos\left[\theta_R - \theta_p(\omega) \right] , \tag{4.3}$$

where θ_R is the angle between the line connecting the two apices and the normal to the interior

(a)

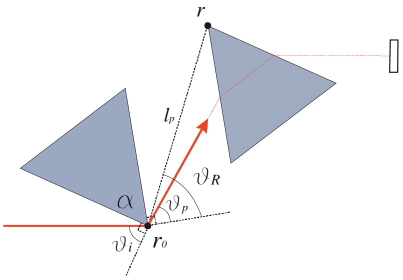

(b)

GVD	-
TOD	-
FOD	-
FiOD	+

Figure 4.2 (a): Schematic drawing of a prism sequence. The amount of the negative dispersion is controlled by changing the distance between two prisms and the insertion length of them. (b): Example of signs for the dispersion of the prism sequence. (SF57 prism, α = 62°, l_p = 10 cm, θ_i = 62°, θ_R = 42°)

faces of the prisms. Fig. 4.2 (b) lists the signs of the dispersion for each order of the SF57 glass prism at the wavelength of 800 nm with an apex angle α = 62°. The prism sequence has an advantage to control the GDD continuously from negative to positive with the control of the angle θ_R and distance l_p. The material dispersion of the second-prism becomes effective in case the prism is deeply inserted, while the angular dispersion is strongly effective in case the second-prism insertion is shallow. Under the later condition, a prism sequence has a negative GDD and negative TOD, which compensates those of materials.

4.1.3 Dispersion of grating sequence

A grating sequence is widely used in high-intensity CPA systems due to its great dispersive ability. Fig. 4.3 (a) illustrates two identical parallel gratings facing each other. The incident beam is diffracted on the first grating surface and spatially expanded. The beam is then re-collimated to form a Fourier plane after the second grating. The original beam cross-section is obtained again after the mirror-imaged reflection. The relation between the incident angles and m$^{\mathrm{th}}$-order diffraction angle for each wavelength is described as

$$\sin\theta_d(\omega) = m\frac{\lambda}{d} - \sin\theta_i \, , \tag{4.4}$$

where d is the grating constant, θ_i is the angle of incidence, and $\theta_d(\omega)$ is the diffraction angle. The phase of the first-order diffracted beam after the grating sequence is written in this form [145]

$$\varphi_g(\omega) = l_g \frac{\omega}{c}\sqrt{1-\left(\frac{\lambda}{d} - \sin\theta_i\right)^2} \quad , \tag{4.5}$$

where l_g is the separation between the gratings. Fig. 4.3 (b) lists the signs of each dispersion

(a)

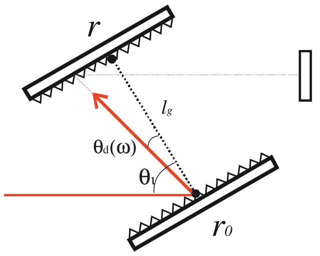

(b)

GVD	-
TOD	+
FOD	-
FiOD	+

Figure 4.3 (a): Schematic drawing of a grating sequence. The ray path is shown for the frequency components with ω. l_g: distance between two gratings along the beam at the central wavelength, θ_i: angle of incidence, $\theta_d\,(\omega)$: diffraction angle at frequency ω. (b): Signs for the dispersion of the grating sequence.

(a)

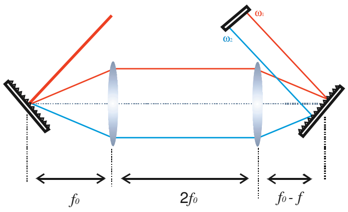

(b)

GVD	+
TOD	-
FOD	+
FiOD	-

Figure 4.4 (a): Schematic drawing of the grating sequence with -1 magnification geometry. (b): Signs for the dispersion of the grating sequence.

order. The grating sequence is different from the prism sequence in that the sing of the GDD is opposite to that of the TOD. The grating sequence has another configuration incorporating with a telescope with -1 magnification (Fig. 4.4 (a)), which realizes the optically negative distance and generates exactly the opposite dispersion (Fig. 4.4 (b)). Both configurations are usually employed as a stretcher and a compressor in CPA systems because this combination exactly cancels the dispersion of each order, which realizes a broadband dispersion compensation. The origin of the larger stretching ability of the grating sequence comes from a strong angular dispersion on the grating surface, which is an advantageous to realize a compact setup. The transmission efficiency of a grating sequence is generally lower than that of the prism sequence.

4.1.4 Dispersion of grism sequence

A grism sequence is a newly designed dispersive device consisting of parallel prisms attached to the surface of gratings. The grism sequence takes both advantages of the prism and grating, i.e. it generates a large amount of negative GDD and TOD with a compact setup. This unique

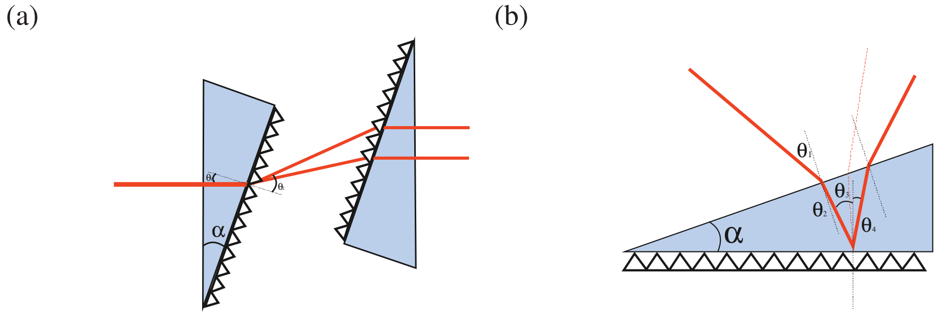

Figure 4.5: Schematic drawing of (a): a transmission grism sequence and (b): a prism attached on a reflection grating.

device was first reported by Tourinois et al in 1993 [146]. In this report, two parallel transmission gratings were engraved on two prisms (Fig. 4.5 (a)). This transmission grism realized a linear dispersion over a large relative bandwidth around an inflection point. This report expected the possibility of the grism sequence to provide a zero TOD. Afterwards, in 1997 S. Kane and J. Squier expanded upon this design, presenting a grism sequence whose TOD is opposite to that of a traditional grating sequence. They demonstrated a first transmission grism stretcher and compressor system, which simultaneously compensated for both GDD and TOD [144, 147]. The grism sequence simultaneously produces a large amount of negative GDD and TOD with a compact setup under a proper condition. The ratio of TOD and GDD for the grism sequence shows the suitable condition for each parameter, and it is described as [144]

$$\frac{\phi'''}{\phi''} = -\frac{\lambda}{2\pi c}\left(\frac{1+n_p\sin(\theta_d)\sin(\theta_i)}{\cos^2(\theta_d)}\right) , \tag{4.6}$$

where n_p is the index of the prism, θ_d is the diffraction angle and θ_i is the incident angle. Only the first negative order diffraction is considered for simplicity. It is possible to make the GDD and TOD same signs, if θ_i and θ_d in Eq. (4.6) have different signs. Because the incident angle and diffraction angle on the border between the prism and grating are related in the from of

$$\sin\theta_d(\omega) = m\frac{\lambda}{d} - n_p\sin\theta_i , \tag{4.7}$$

the following condition should be satisfied under the first diffraction order (m = 1) [148]:

$$\sin\theta_i > \frac{\lambda}{n_p d} . \tag{4.8}$$

This configuration is realized if the prism refractive index n_p, grating constant d, and incident angle θ_i are properly chosen. This indicates that the grating constant d and refractive index n_p should be large to suppress the incident angle θ_i. In experiment it is preferable to use the grating

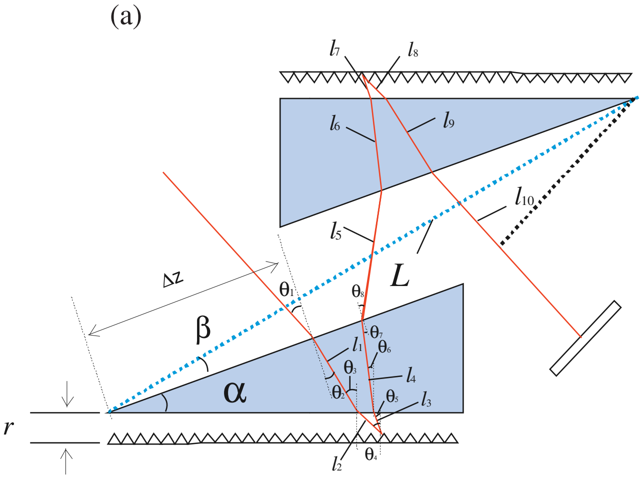

(b)

GVD	-
TOD	-
FOD	-
FiOD	-

Figure 4.6 (a): Schematic drawing of a reflection grism sequence [148]. θ_i: incident angle, α: apex angle, Δz: beam insertion, r: prism-grating distance, L: apex-to-apex distance. (b): Example of signs for the dispersion of the grism sequence. (SF57 prism, d = 651 lines/mm, α = 22.5°, r = 0.1 mm, Δz = 35.0 mm, L = 110.5 mm)

with a large d and a prism material with high refractive index, which will let the grism work at small incident angle [148]. The problem of the transmission-grism sequence has been its low diffraction efficiency. Gibson et al reported an alternative new design of a reflection-grism sequence (Fig. 4.5 (b)) [149]. The reflection grism is the combination of a reflection grating and a prism, designed to generate the negative TOD with a high transmission efficiency. In order to increase the transmission efficiency of the grism sequence, it is designed in the Littrow configuration; the angular difference between the incident and diffracted beam should be as small as possible. In this configuration Eq. (4.8) is satisfied, i.e. the diffraction beam and incident beam are at different side of the grating normal direction (solid line in Fig. 4.5 (b)). This configuration is however not convenient because the grating is coated on one side of the prism. It is more practical and adjustable if the grating and prism are separated from each other. The design considerations and comprehensive dispersion analyses of such a prism-grating separated reflection-grism sequence are discussed in detail in Ref. [148]. It is pointed out that the dispersion amount of a grism pair depends sensitively on the optical beam path within the prism. The dispersion of the grism sequence is calculated based on ray-tracing methods. Fig. 4.6 (a) shows the scheme of the reflective grism sequence with a beam trace. The GDD and TOD induced in the reflection-grism sequence are controlled by the incident angle θ_i, the apex angle α of the prisms, the beam insertion length from the prism apex Δz, and the distance r between the prism and the grating. For simplicity, the distance r for both grisms is assumed to be the same. According to the information shown in this figure, the optical beam path at frequency ω in this grism pair can be expressed as

$$l(\omega) = n_p(\omega)\left[l_1 + l_4 + l_6 + l_9\right] + \left[l_2 + l_3 + l_5 + l_7 + l_8 + l_{10}\right], \tag{4.9}$$

where the first term shows the optical path length in the prisms and the second term in air. The spectral phase is calculated by tracing the optical beam path of each frequency, which is easily obtained from the geometrical consideration by use of the Snell's low. One possible ray-tracing is shown in Ref. [150]. The resulting accumulated phase amounts to

$$\phi(\omega) = 2\left[\frac{\omega l(\omega)}{c} + R(\omega)\right], \tag{4.10}$$

where c is the speed of light in vacuum and $R(\omega)$ the corrected phase term from the gratings [143]. The factor of two in (4.10) accounts for the double pass through the setup. The $R(\omega)$ is described as

$$R(\omega) = \frac{2\pi}{d}\left[(l_3 + l_7)\sin\theta_5 + (l_4 + l_6)\sin\theta_6 + l_5\sin(\alpha - \theta_8)\right]. \tag{4.11}$$

Fig. 4.6 (b) lists an example of the sign for the dispersion of the grism sequence at the wavelength of 800 nm. As seen in the next section, the numerical simulation shows that the negative GDD and TOD generated in the grism sequence is much larger than those in the prism sequence.

4.1.5 Summary

This section has discussed the properties for representative dispersive devices. The advantages and disadvantages of the each device are as follows:

- **Transparent materials** have a positive GDD and a positive TOD. A high-transmission-efficiency is obtained with a simple configuration.

- **A prism sequence** has a negative GDD and a negative TOD. It is usually used to compensate the dispersion of thin materials. A high transmission efficiency is obtained at the Brewster-incidence. The GDD is easily controlled from negative to positive.

- **A grating sequence** has a negative GDD and a positive TOD (or a positive GDD and a negative TOD). It has a strong dispersive ability and is therefore applied to the high-power laser system but it has a low transmission (diffraction) efficiency.

- **A grism sequence** has a negative GDD and a negative TOD. It has a strong dispersive ability but a low transmission efficiency. The handling of the grism sequence is rather difficult, compared to the other devices.

4.2 Stretcher and compressor design

In the choice of the dispersive devices in the OPCPA system, there are several possible combinations that satisfy the dispersion compensation up to 3rd order or even higher order, i.e. combinations of a grating sequence and grating sequence, a prism sequence and glass-block, and a grism sequence and glass-block. It is ideal if the dispersion of a stretcher and a compressor are completely opposite in this spectral range. A grating stretcher and a grating compressor is therefore a first candidate among these combinations. It is actually the most popular stretcher-compressor pair in CPA systems and realizes a large stretching ability. However, the transmission efficiency of the grating sequence is around 50 % [63]. Even higher transmission efficiency is achievable with a combination of a glass-block and a prism sequence. Both devices have a high transmission efficiency when the angle of incidence is set at a Brewster angle. Normally, a glass-block is employed as a stretcher and a prism sequence as a compressor because a positive chirp before the amplification prevents the pulse compression in the amplifier medium and the following crystal damaging. A problem of this combination is that, when a large stretching ratio up to 10^4 with an extremely broadband spectrum is demanded, the dimension of the prism sequence becomes so large that the prism sequence is not practical in the actual laser system. The temporal duration of the pump and stretched signal pulses is a key issue in OPCPA, because it influences the energy conversion efficiency, the gain narrowing, and the shot-to-shot stability. An optimum stretching ratio is required for a good temporal overlap between the signal and pump pulse. Recently, the combination of a prism stretcher and a glass-block compressor was reported by Gaudiosi *et al.* [151]. Because this scheme employs a negative-chirp stretcher and a positive-chirp compressor, it is called down-chirped scheme. This scheme is advantageous in that the glass block with a large stretching ability and high transmission efficiency can be used as a compressor. With this scheme, the candidate of a grism stretcher and glass-block compressor comes up to the choice. This combination is expected to have a large stretching ability with a compact setup size of the grism stretcher and has been already applied to the terawatt-level OPCPA system by Tavella *et al.* [64]. They used reflection grism pair for stretcher and glass blocks for high throughput compressor, and succeeded to generate sub-10 fs pulses with 10-TW peak power. Consequently, the combination of the grism stretcher and glass-block compressor is the best selection for the dispersion management of a broadband intense OPCPA system.

In designing the grism stretcher and glass-block compressor, there is an important point that must be considered for a global dispersion management, i.e. the residual dispersion must be suppressed within the working window of the dispersive compensation device. For the compensation of the dispersion over a broadband spectral range, the dispersion up to high orders must be compensated by use of an adaptive dispersive device. The compensation wavelength range is limited due to the working window of the adaptive dispersive device. In order to broaden the effective spectral range of the adaptive optical filter, the grism stretcher is newly designed. In the following section, grism designs are discussed to suppress the residual group-delay within the working window and expand the tunable bandwidth of the adaptive dispersive device.

4.3 Grism stretcher design

This section concentrates on designing the grism stretcher in the down-chirp scheme for the OPCPA system. The grism stretcher is designed in two configurations. First, a conventional TOD/GDD-matching design is introduced, which suppresses both GDD and TOD simultaneously at the central wavelength. Then, a novel global-dispersion-balance design is discussed to broaden the acceptance bandwidth of the adaptive optics.

4.3.1 TOD/GDD-matching design

The TOD/GDD-matching design is based on the conventional grating design of Ti:sapphire CPA systems. The residual dispersion in the whole system is the sum of the dispersions introduced by the individual components [144], i.e.

$$\varphi^{(n)}(\omega)=\sum_i \varphi_i^{(n)}(\omega) \ , \tag{4.10}$$

where i indicates the individual components in the system, and n is the deviation times. The total GD, GDD, TOD… is the summation of GDs, GDDs, TODs… of all optical components. A proper pulse compression is realized when the summation of GDDs and TODs at a central wavelength for each optical component should fulfil the following relations [144]

$$\varphi''^{(total)}=\sum_i \varphi_i''=\varphi''^{(str)}+\varphi''^{(mtr)}+\varphi''^{(cmp)}=0 \tag{4.11}$$

$$\varphi'''^{(total)}=\sum_i \varphi_i'''=\varphi'''^{(str)}+\varphi'''^{(mtr)}+\varphi'''^{(cmp)}=0 \ , \tag{4.12}$$

where $\varphi^{(\mathrm{str})}$, $\varphi^{(\mathrm{mtr})}$, and $\varphi^{(\mathrm{cmp})}$ are phases for the stretcher, the amplifier medium, and the compressor, respectively. Ref. [148] provided theoretical analyses of the grism design with central wavelengths from 750 nm to 850 nm. The table in Fig. 4.7 (a) shows the signs of the GDD and TOD for each component in the down-chirped grism-stretcher and glass-block compressor system. The ratio TOD/GDD in the grism stretcher is then determined from the following equation

$$\left|\frac{\phi'''}{\phi''}\right|_{grism}=\frac{\left|\phi'''_{SF57}+\phi'''_{materials}\right|}{\left|\phi''_{SF57}+\phi''_{materials}\right|} \ . \tag{4.13}$$

The ratio TOD/GDD for the grism stretcher is set to be equal to that of the compressor and all other materials in the system [152]. In this simulation, a 25-mm TeO_2 crystal, 10-mm BBO crystal and 200-mm SF57 glass-block and 100-mm fused silica glass-block are considered. The ratio for the material is calculated to be TOD/GDD = 0.628 fs at the central wavelength of 800

(a)

Device	GVD	TOD
Stretcher	-	-
Material	+	+
Compressor	+	+

(b)

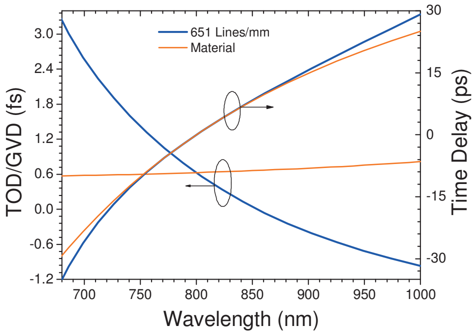

Figure 4.7 (a): Signs of the GDD and the TOD for each device. Both material and glass-block compressor show a positive GDD and TOD. (b): Ratio TOD/GDD for the grism stretcher and glass-block compressor [148]. The grism stretcher is optimized to have the same ratio as the glass-block compressor at 800 nm.

(a)

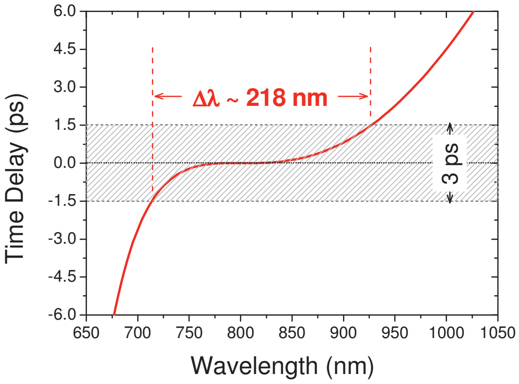

(b)

(@ 800 nm)	GDD (fs^2)	TOD (fs^3)	FOD (fs^4)	FiOD (fs^5)	TOD/GDD (fs)
grism	-6.186×10^4	-3.883×10^4	-3.089×10^5	-9.007×10^5	0.628
materials	6.186×10^4	3.885×10^4	1.143×10^4	2.159×10^4	0.628
residual	0	20	-2.975×10^5	-8.791×10^5	

Figure 4.8 (a): Residual spectral group-delay of the whole system optimized at 800 nm [148]. The shaded area denotes the compensation range of the acousto-optic filter. The acceptance bandwidth of 218 nm is obtained, when it is optimized at 800 nm. (b): Total higher-order dispersion of the grism and the following optical elements optimized at 800 nm [148]. The GDD and TOD are minimized in this configuration.

nm (See Fig.4.7 (b): orange line). The grism stetcher employs gratings with 651 lines/mm grating constant and SF57 prisms with 22.5$^{\mathrm{o}}$ apex angle. The distance r between the prism and grating is set to 1.0 mm and the insertion length of the incident beam Δz is set to 35.0 mm. The TOD/GDD-matching design requires the optimization of two parameters, the incident angle θ_i and the distance L between the apexes of two prisms. First, the angle θ_i is optimized to let the TOD/GDD ratio exactly same for each component. The blue line in Fig. 4.7 (b) shows the simulation result of the TOD/GDD ratio for the grism stretcher. Once the ratio TOD/GDD for the grism stretcher and the materials are equalized, the residual GDD and TOD of the whole system are set to be zero at the central wavelength of 800 nm. The amount of the GDD is determined by the distance L, which makes the absolute GDD amount exactly zero at the central wavelength [148]. Fig.4.8 (a) shows the residual group delay of the whole system, and Fig. 4.8 (b) provides the values of the dispersion for each order: the incident angle $\theta = 0.344^{\mathrm{o}}$, $\beta_0 = 7.367^{\mathrm{o}}$, the apex distance of two prisms $L = 102.462$ mm.

The TOD/GDD-matching design is quite beneficial when the spectrum is not broadband. However, when the amplified spectrum becomes broad enough to support few-cycle pulses, the pulse compression requires the help of the additional adaptive optics to compensate the dispersion up to higher orders. The adaptive dispersion compensation device has a certain temporal working window, e.x. 3.0 ps for the AOPDF. When the AOPDF is employed in the TOD/GDD-matching design, it enables to compensate the residual dispersion in a spectral range from 713 nm to 931 nm with a bandwidth of $\Delta\lambda = 218$ nm. Because the optical dispersive device can arbitrarily control the dispersion within the working window, other designs are also acceptable if the total dispersion is still in this window. The grism design is therefore reformed to utilize the full working range of the adaptive dispersive device for the high-order dispersion compensation over a broadband range.

4.3.2 Global-dispersion-balance design

Global-dispersion-balance design is a novel design for the broadband dispersion compensation. Dou *et al.* have modified the TOD/GDD-matching model introduced in Ref. [148] and realized an acceptance bandwidth more than one octave [150]. This design remains parts of the GDD and TOD to balance the higher order dispersion, which extends the working bandwidth of the AOPDF while the total dispersion is still in the compensation range. The configuration change from the TOD/GDD-matching design to the global-dispersion-balance design is quite simple: the apex distance L between two prisms is changed (Fig. 4.9). This design rather provides the GDD and TOD to the residual phase to balance the all dispersion order in a wide spectral range. In fig. 4.10 (a), the residual group delays of the TOD/GDD matching design and the global-dispersion-balance design with a limitation of the AOPDF are plotted. The group delay of the material and the compressor consist of 25-mm TeO_2 crystal in the AOPDF, 15-mm BBO crystal, 350-mm SF57 glass blocks and 200-mm fused-silica glass block. This ray-tracing analysis assumes a grism sequence composed of gratings with 651 lines/mm and SF57 prisms

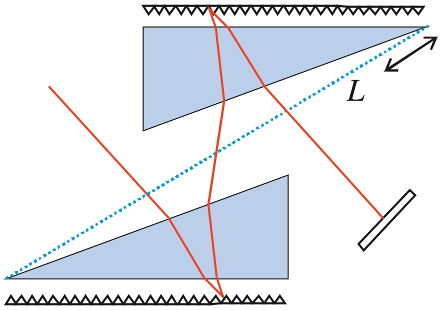

Figure 4.9: Configuration change from the TOD/GDD-matching design to global-dispersion-balance design.

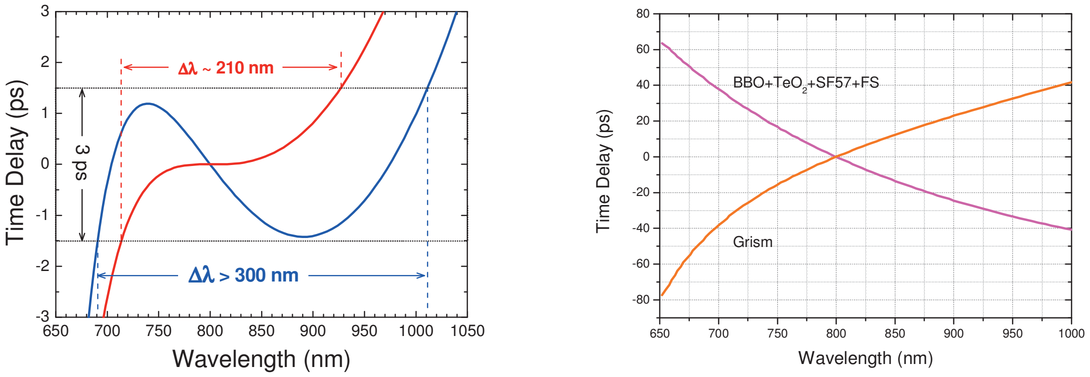

(c)

Residual	GDD (fs^2)	TOD (fs^3)	FOD (fs^4)	FiOD (fs^5)
(@ 800 nm)	9.170×10^3	-2.668×10^3	-4.216×10^5	-9.107×10^5

Figure 4.10 (a): Residual spectral group-delay of the whole system. The AOPDF compensates for the higher order dispersions in 3.0 ps range. (b): Simulated spectral group-delay for each device in our OPCPA system. Grism stretcher, 15-mm BBO, 25-mm TeO2, 350-mm SF57 and 250-mm fused silica are considered. (c): Residual high-order dispersion at the central wavelength of 800 nm.

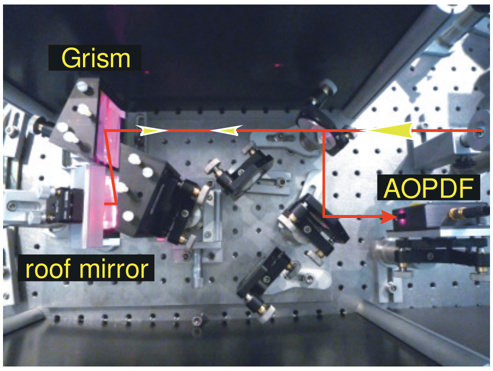

Figure 4.11: Photograph of the grism stretcher. The horizontally polarized signal beam goes into the first grism at the normal angle. The diffracted beam is collimated after the 2nd grism and then reflected back with a roof mirror. A following acousto-optic programmable dispersive filter (AOPDF) compensates for the high-order dispersion.

with apex angle $\alpha = 22.5^{\circ}$. The distance r between the grating and prism is chosen to be 0.1 mm. The incident position Δz for a central wavelength of $\lambda = 800$ nm are both 35.0 mm at the first and the second prism. In the grism stretcher, the apex distance L between two prisms is set to 110.5 mm. Compared with the TOD/GDD matching design (red line), the global-dispersion-balance design (blue line) spreads the tuning range from 690 nm to 1.01 μm (acceptance bandwidth of more than 300 nm). Low-order dispersion still remains at the central wavelength, but the tunable bandwidth of the AOPDF is expanded. Fig. 4.10 (b) shows the group-delay for the grism stretcher and the following materials and the compressor. The pulse is stretched to more than 80 ps in the spectral range from 700 nm to 1.0 μm. Such strongly stretched signal pulses allow the further energy scaling in OPCPA under the damage threshold of the amplifier medium. The residual dispersions from 2nd to 5th order at 800 nm are shown in Fig. 4.10 (c). In the TOD/GDD-matching design, the stretcher is designed to compensate the GDD and TOD at the central wavelength but the large amount of FOD and FiOD change the GD rapidly at both ends of the spectral range. On the other hand, in the global-dispersion-balance design, the GDD and TOD are allowed to have the dispersion and successfully suppress the residual group-delay of the whole system within a working range of an adaptive dispersive device for expanding its tunable bandwidth. Fig. 4.11 shows the photograph of the constructed grism stretcher and the following AOPDF. A large stretching ability is realized with a very compact stretcher size (17.5 cm × 17.5 cm), which is expected to support a long-term stability.

4.4 Summary

In this chapter we have discussed a suitable combination for a stretcher and a compressor and an optimum stretcher-compressor design. A grism pair was selected as a stretcher and a SF-57 glass-block as a compressor. This down-chirped scheme is expected to have a more than 90-% transmission efficiency of the glass-block compressor. Two grism configurations, TOD/GDD-matching design and global-dispersion-balance design, have been investigated through the simulation. The global-dispersion-balance design has broadened the tuneable bandwidth of the AOPDF more than 300 nm (from 690 nm to 1010 nm) with a large stretching ability in a compact setup. The grism stretcher and the glass-block compressor in a global-dispersion-balance design is an attractive and promising stretcher-compressor scheme to achieve an energy scaling of few-cycle pulses.

CHAPTER 5

OPCPA laser system

This chapter introduces experimental OPCPA setups based on the simulation results discussed in the previous chapters. Our OPCPA system is developed in two steps, first at 1 kHz and then at 20 kHz repetition rate. A commercial neodymium-doped yttrium lithium fluoride (Nd:YLF) laser is employed as a pump source for a 1-kHz OPCPA system, while a newly designed neodymium-doped yttrium ortho-vanadate (Nd:YVO_4) laser for a 20-kHz OPCPA system. This stepwise construction finally leads to a correct layout, where a successful stretching, amplification, and compression of signal pulses are achieved.

5.1 OPCPA system overview

A scheme of our OPCPA system is briefly displayed in Fig. 5.1. The system consists of a signal oscillator, a pump source, a synchronization system, a stretcher, an amplifier medium, a compressor, and an adaptive dispersive device. The pump source is electrically synchronized with the Ti:sapphire oscillator. Our system starts from a Kerr-lens mode-locked femtosecond Ti:sapphire oscillator. Signal pulses are expanded in a stretcher within the amplification window of the pump pulses. A β-barium borate (BBO) crystal is employed as an optical parametric amplifier stage. The stretched signal pulses are amplified in the nonlinear crystal and then compressed by use of a glass-block compressor. Output pulses are characterized by a dispersion balanced intensity autocorrelator, FRAC, and MIIPS.

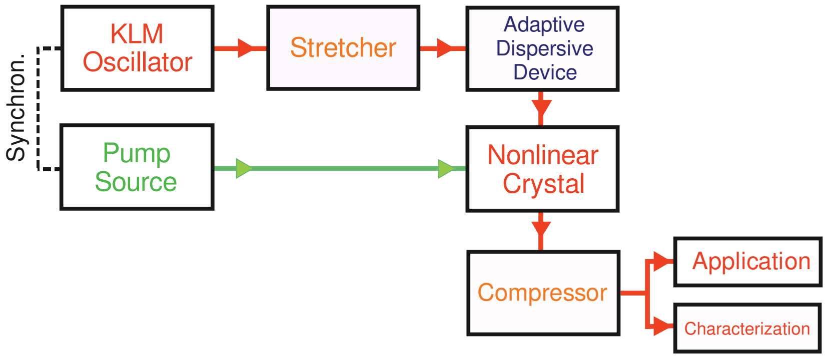

Fig. 5.1: Schematic overview of the experimental OPCPA system setup. Synchron: Synchronization system, KLM: Kerr-lens mode-locking, OPA: optical parametric amplifier.

5.2 System setup: Signal oscillator

The signal source is shared in both 1-kHz and 20-kHz OPCPA system. It is a commercial Kerr-lens mode-locked Ti:sapphire oscillator (Rainbow, Femtolesers GmbH). It generates 2.0 nJ, 7.0 fs output pulses, pumped with a 532-nm cw-laser (Verdi, Coherent). The repetition rate is varied roughly between 76 MHz and 80 MHz by changing the cavity length. Fig. 5.2 (a) shows the output spectrum and the inset shows the calculated transform-limited pulse from the spectrum. The spectrum covers a range from 650 nm to more than 1.0 μm, supporting sub-7.0 fs FWHM transform-limited pulse duration. The broadband spectrum from the oscillator is expanded to more than one octave in a periodically poled lithium niobate (PPLN) crystal together with self-phase modulation (SPM), and simultaneously difference frequency generation (DFG) signal is produced to create an f-to-0f interferometer [88]. A pair of the BaF_2 thin wedges is inserted in the cavity at the Brewster angle, which adjusts the dispersion in the cavity and the beat frequency for the CEP control. Fig. 5.2 (b) shows the carrier-envelope offset frequency f_0 signal and the repetition frequency of the oscillator f_{rep} signal monitored by a spectral analyzer. The f_0 and f_{rep} are set to 20 MHz and 80 MHz, respectively.

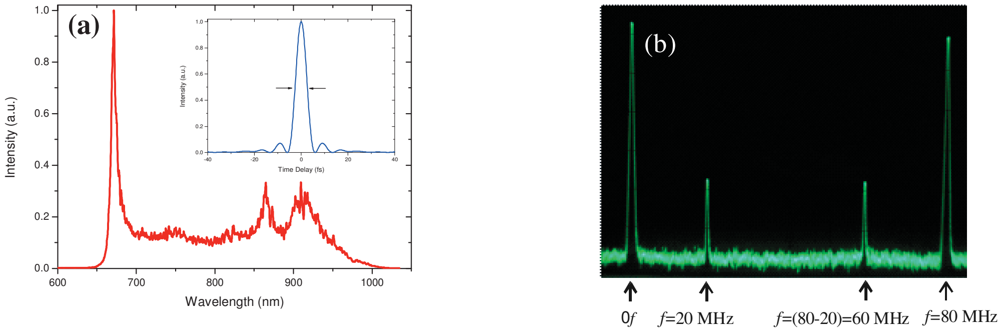

Figure 5.2 (a): Measured output spectrum of the Kerr-lens mode-locked signal oscillator (Rainbow). Inset: Sub-7 fs FWHM transform-limited pulse profile calculated from the output spectrum assuming a flat spectral phase. (b): Measured carrier-envelop offset frequency signal.

5.3 1-kHz OPCPA

In 1-kHz OPCPA demonstration, the parametric amplification performance is examined in the non-collinear optical parametric scheme designed in the previous chapter.

5.3.1 1-kHz OPCPA system setup : Pump source

The neodymium-doped yttrium lithium fluoride (Nd:YLF) pump laser (Model 4400 series, Quantronix) consists of a Nd:YLF oscillator and a Nd:YLF regenerative amplifier. The Nd:YLF

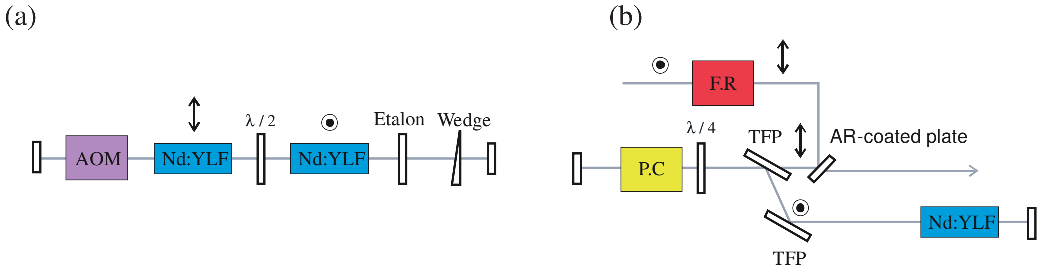

Figure 5.3: Optical layout of the 1-kHz pump laser system. (a): Nd:YLF mode-locked oscillator. AOM: acousto-optic modulator, $\lambda/2$: half-wave plate (b): Nd:YLF regenerative amplifier. F.R: Faraday rotator, P.C: Pockels cell, TFP: thin film polarizer.

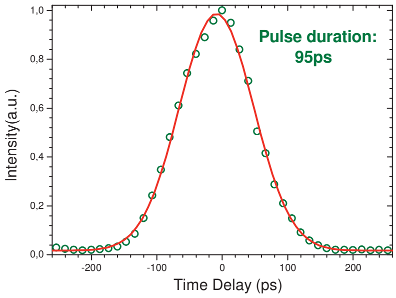

Figure 5.4: Measured autocorrelation trace for the output of the Nd:YLF regenerative amplifier after the frequency-doubling by the LBO crystal. The pulse duration is expected to be 95 ps by multiplying the deconvolution factor of the Gaussian fitting.

oscillator is electrically synchronized with the Ti:sapphire signal oscillator. Fig. 5.3 (a) and (b) show the optical layout of the oscillator and amplifier, respectively. Crystals in an oscillator and in a regenerative amplifier are pumped by arc lamps. The oscillator consists of two Nd:YLF crystals, an acousto-optic modulator (AOM), a half-wave plate, an etalon, and a wedge. Two Nd:YLF crystals with a half-wave plate realize the uniform amplification of the seeded beam. The etalon is used to select proper longitudinal modes in the cavity to control the pulse duration. The oscillator generates 1053-nm infrared pulses at a repetition rate of 76 MHz. Seeded pulses from the Nd:YLF oscillator are captured inside the cavity by use of a Pockels cell. A Faraday rotator before the amplifier cavity prevents the back reflection of the amplified pulse. The repetition rate of the amplified pulse is reduced to 1 kHz after the Nd:YLF regenerative amplifier. The pulses are frequency-doubled by use of a LBO crystal. The final output has a 750-μJ pulse energy with 95-ps FWHM pulse duration (Fig. 5.4).

5.3.2 Synchronization and timing Jitter

The three-wave coupling is an instantaneous process, and therefore the pump and signal pulses are to be strictly overlapped in time in an amplifier medium. A timing-jitter induces an energy

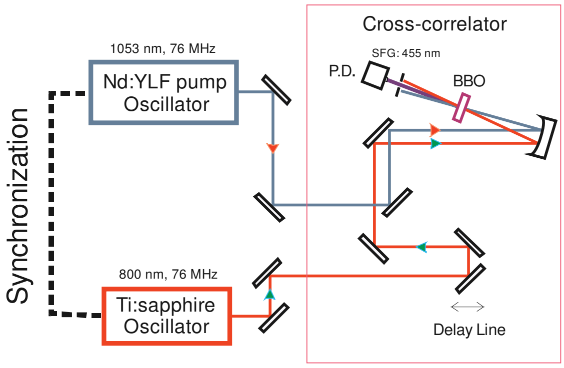

Figure 5.5: Layout of the synchronization measurement by use of a cross-correlator. Dashed lines represent electronic connections, while solid lines are laser beams from both oscillators. P.D.: photodiode, BBO: β-barium borate crystal.

fluctuation of amplified pulses and, in even worse case, it causes an amplified spectral modulation. A simple technique for measuring the timing jitter based on a cross-correlator was reported in Ref. [153, 154]. Fig. 5.5 shows the experimental setup for measuring the timing-jitter between the signal oscillator and the pump oscillator. The pulses from the Ti:sapphire oscillator and Nd:YLF oscillator are cross-correlated in the BBO crystal. The principle for the timing-jitter measurement by use of a cross-correlation is schematically illustrated in Fig. 5.6. Two pulses overlap each other in a nonlinear crystal (Fig. 5.6 (a)). The relative position between two pulses is varied from time to time due to the timing-jitter. Fig. 5.6 (b) shows the corresponding SFG signals. The intensity of the SFG signal-peak depends on the amount of the overlapping between two pulses. A high SFG signal peak is obtained in case two pulses are well overlapped in a crystal, while the SFG signal is decreased when they are separated due to a large amount of the temporal shift. The fluctuation of the SFG signal can be a measure of the timing-jitter because, in a small temporal range, the cross-correlation signal is proportional to the timing-jitter. Especially when the short pulse is placed at half peak of the long pulse, the slope of the pump-pulse envelope is steepest and therefore the SFG signal becomes sensitive to the timing-jitter. The amount of the jitter is calibrated from the slop of the measured cross-correlation trace. Fig. 5.7 shows the integrated data points of the cross-correlation and a fitting trace by use of a Gaussian function. The cross-correlation trace has a duration of 99 ps full width at half maximum (FWHM). After this cross-correlation measurement, the delay line is carefully set to reduce the SFG signal to the half maximum. The SFG signal is detected and monitored by use of a photodiode and an oscilloscope. Fig. 5.8 (a) shows the obtained SFG pulse train at the offset in time by 1/2 the pulse width. The mean value and the standard deviation (STD) of the pulse peaks are measured to be 59.5 % and 6.4 % of the maximum intensity, respectively. The time jitter is calibrated from these data by use of this cross-correlation trace. The dash line and solid line in Fig. 5.7 show to the average value and the

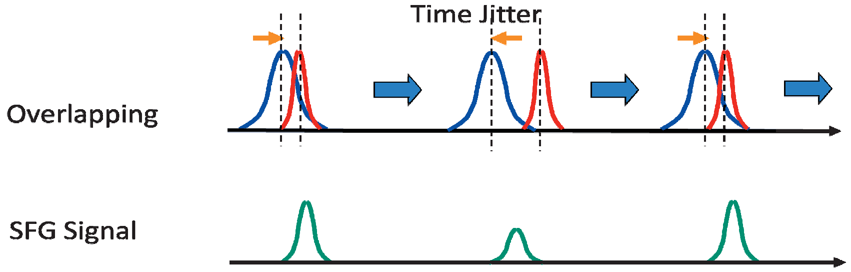

Figure 5.6: Schematic illustrations of the SFG signal intensity variation caused by the timing-jitter between the signal and pump pulses. (a): Relative position change between a signal pulse and pump pulse. (b): Corresponding SFG pulses for each relative position. The SFG peak intensity depends on the relative position.

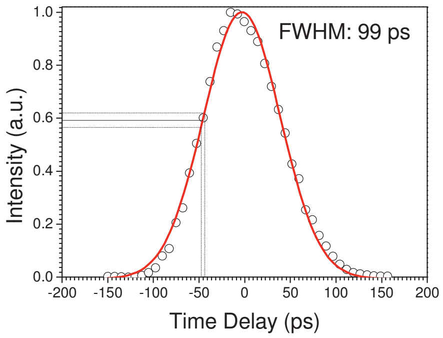

Figure 5.7: Measured cross-correlation trace for the SFG signal. The trace has a duration of 99 ps FWHM by use of a Gaussian fitting.

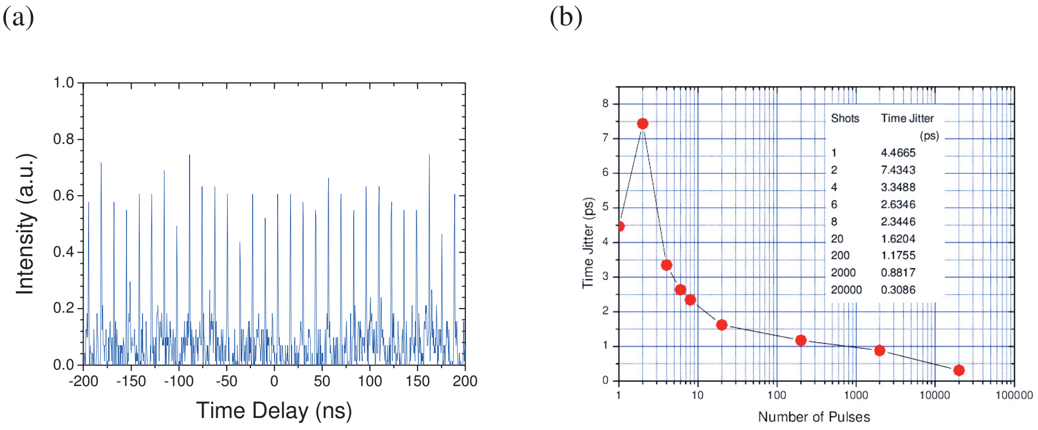

Shots	Time Jitter (ps)
1	4.4665
2	7.4343
4	3.3488
6	2.6346
8	2.3446
20	1.6204
200	1.1755
2000	0.8817
20000	0.3086

Figure 5.8 (a): Measured SFG pulse train at the offset in time by 1/2 the pulse width. The interval of the pulse peaks is 13 ns, corresponding to 76 MHz repetition rate. (b): Timing-jitter as a function of the number of pulses. The mean value and the STD for the different pulse number from 1 to 20000 shots.

STD. 6.4 % fluctuation of the SFG peak corresponds to a 4.5-ps timing-jitter. The timing-jitter is calculated for different pulse numbers from 1 to 20000 shots by use of Allan variance (AVAR) [155]. AVAR is often introduced to estimate the stability of noisy signals or imperfections coming from the temperature effects. The deviation is the square root of the AVAR and is calibrated to the amount of the timing-jitter through the cross-correlation trace. Fig. 5.8 (b) shows the results of the calibrated timing-jitter for different the number of pulses. The minimum jitter is estimated to be 7.5 ps in case every two pulses are averaged.

5.3.3 1-kHz OPCPA system: Optical layout

Fig.5.9 displays the optical layout of the 1-kHz OPCPA laser system. The Nd:YLF pump laser and the Ti:sapphire oscillator are electrically synchronized. The pump beam is focused down to 300-μm in diameter at the OPA stage by use of a relay-imaging telescope (See Appendix B). The corresponding pump intensity is 10 GW/cm^2. Signal pulses from the oscillator are temporally expanded to about 90 ps (700 nm - 1000 nm) by means of a grating pair consisting of 1800 lines/mm gratings with Aluminium coating. The stretched pulses are amplified in a single-stage double-pass OPA. The pump and signal pulse are temporally and spatially overlapped in the BBO crystal in a non-collinear geometry. The phase-matching and non-collinear angle at the OPA stage is optimized at a signal wavelength of 755 nm. The BBO crystal has a 5-mm thickness with an aperture size of 8 mm × 8 mm.

There are two possible beam geometries in NOPA configuration. In Fig. 5.10, two parametric amplification schemes are shown: a tangential phase-matching (TPM) scheme and a Poynting vector walk-off compensation (PVWC) scheme [156]. In the TPM scheme the optical axis lies in the same side of the signal beam from the pump beam, while in the PVWC scheme

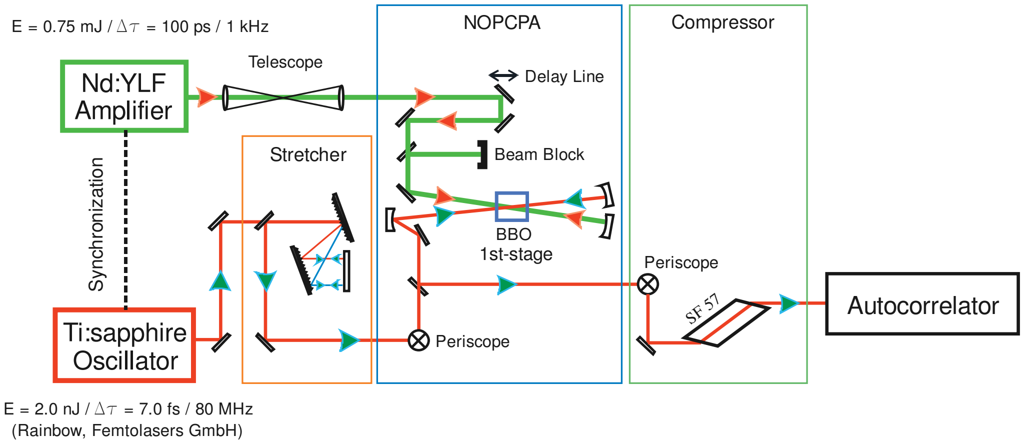

Figure 5.9: Optical layout of the single-stage two-pass 1-kHz OPCPA system. BBO: β barium-borate crystal, Telescope: relay-imaged telescope.

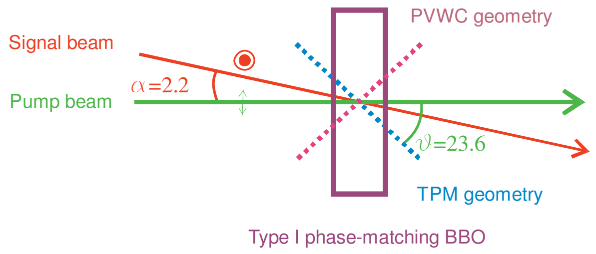

Figure 5.10: (a) Tangential phase matching (TPM) geometry (optical axis: blue-dashed line) and (b) Poynting vector walk-off compensation (PVWC) geometry (optical axis: red-dashed line) in NOPA. In TPM geometry, the direction of a signal beam lies between a pump beam and the optical axis.

the axis lies in the other side of the signal beam. The TPM and PVWC scheme in non-linear OPCPA are reported in detail in Ref. [120]. In both schemes the phase-matching angle is same, but there exists a difference in the amplification efficiency. The TPM scheme is recommended in OPCPA because this scheme prevents frequency-doubling of the signal beam and realizes a higher pump-to-signal conversion efficiency than the PVWC geometry. If the PVWC scheme is applied, the angle between the signal and optical axis ($\theta+\alpha$) is near the phase-matching angle at the wavelength of around 400 nm and results in the generation of the second harmonics for the amplified signal beam.

In experiment, infrared optical parametric fluorescence (OPF) is used as an instructive guide for the crystal alignment. When the signal beam is blocked, an infrared optical parametric fluorescence (OPF) ring is observed behind the crystal. The radius of the OPF ring is optimized by changing the phase-matching angle. The angle between the pump beam and the signal beam is in advance optimized at the non-collinear angle, and the OPF ring is set to be overlapped with the signal beam in space after the OPA stage. The signal and pump beams are imaged back and focused into the same BBO crystal again by use of concave mirrors for the 2nd pass amplification (double-pass configuration). After the 2nd pass in the amplifier medium the signal beam is collimated with two concave mirrors and goes into the compressor. A 20-cm SF-57 glass block (Schott) cut at the Brewster angle is simply employed as a compressor. After the compression the pulse is characterized by use of an intensity autocorrelator.

5.3.4 Experimental results

The spectrum and the output power are measured after the 2nd pass in the single OPA stage. Fig. 5.11 (a) plots the amplified spectrum with a broadband wavelength ranging from 660 nm to 850 nm. The cut-off of the amplified spectrum at the short wavelength of around 670 nm corresponds to that of the Ti:sapphire oscillator spectrum, while the attenuation of the amplified

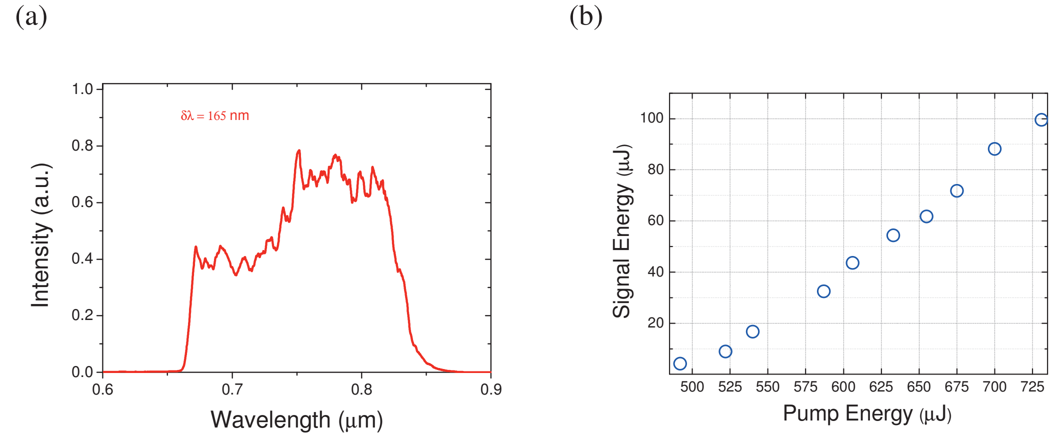

Figure 5.11 (a): Measured spectrum after the amplification. (b): Measured output-pulse-energy depending on the pump pulse energy. Note that these doubly internally reflected pulses are included in these results.

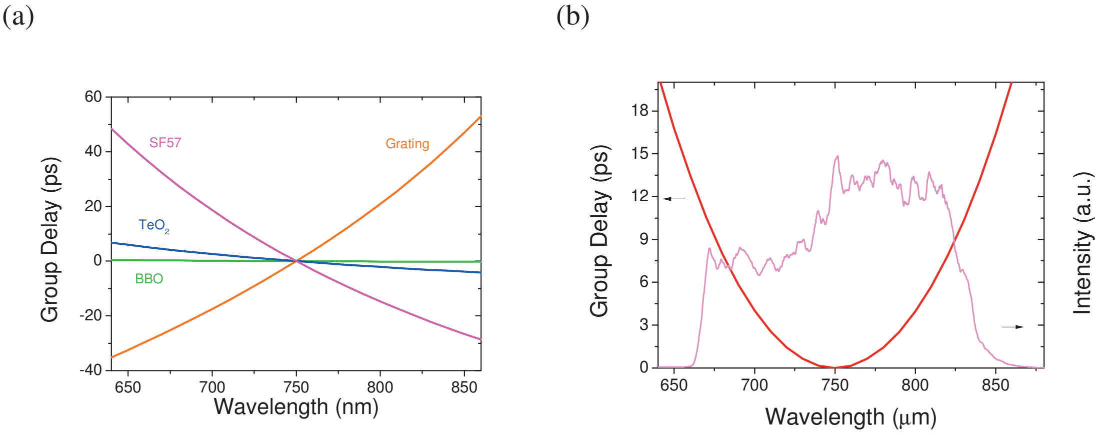

Figure 5.12 (a): Relative group-delay for each component in 1-kHz OPCPA at the central wavelength of 750 nm. (b): Total group-delay of the whole system. The shade is the measured spectrum.

spectrum at the long wavelength around 850 nm is due to the phase-mismatching in this non-collinear geometry. Because the signal spectrum form the Ti:sapphire oscillator covers the wavelength over 1.0 μm, it is expected that the further spectral broadening is possible by carefully optimizing the phase-matching condition at the rather longer wavelength. Fig. 5.11 (b) plots the output energy dependence on the pump energy after the OPA stage. The signal energy is amplified up to 100 μJ with increasing the pump energy up to 750 μJ, although no remarkable amplification is observed at the pump energy below 500 μJ. There is a possibility of the amplification at even higher energy level by constructing a 2^{nd} OPA stage.

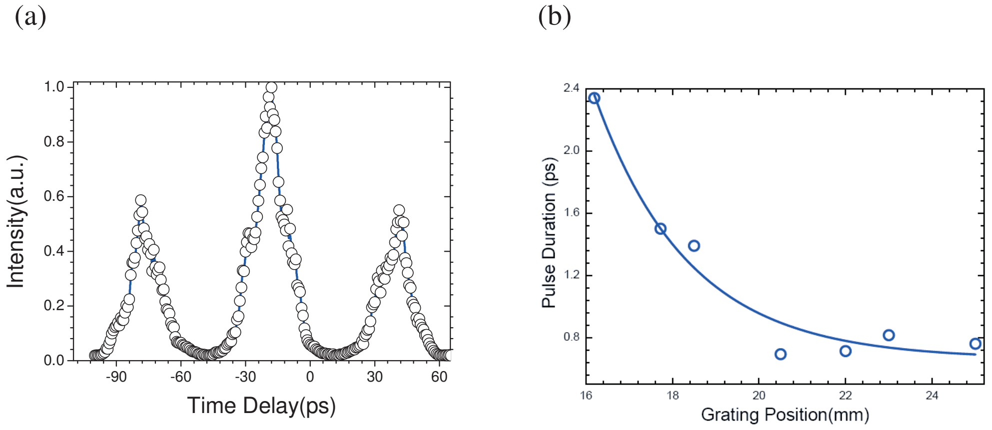

Figure 5.13 (a): Measured autocorrelation trace for the amplified signal pulse. The interval of these peaks corresponds to 60 ps. (b): Grating-position dependent pulse duration of the main pulse.

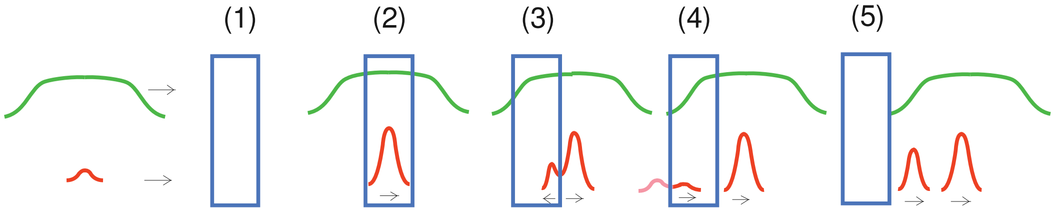

Figure 5.14: Beam propagation in a conventional BBO crystal. Doubly internally reflected pulses are amplified in OPCPA [157].

Fig. 5.12 (a) shows the simulated group-delay of the grating stretcher, the materials and the glass-block compressor in the 1-kHz OPCPA system. Because the grating stretcher and the glass-block compressor support only the GDD, the GD is flat only around the central wavelength (Fig. 5.12 (b)). 3-ps working window of the AOPDF restricts the compensable spectral range from 700 nm to 800 nm. In order to expand the bandwidth, the grating stretcher is replaced with the grism stretcher to compensate the dispersion up to 3rd order. The details will be discussed in the later section.

The compressed amplified pulses are characterized by use of an intensity autocorrelator. Fig. 5.13 (a) plots the autocorrelation trace of the amplified signal pulse after a 20-cm SF57 glass-block compressor. Several peaks are observed at the interval of 60 ps around the main pulse. Such a multi-pulse-amplification has been a general problem in OPCPA due to the amplification of internally reflected signal pulses in a crystal [157]. When a pump pulse is much longer than the length of an amplifier medium, the reflected signal pulse is amplified again in the long tail of the pump pulse. The interval of the periodic signal peaks corresponds to the rounding time in the 5-mm BBO crystal. The generation process of internally reflected pulses in an amplifier medium is illustrated in Fig. 5.14. (1): A pump pulse and a stretched signal pulse approach the BBO crystal. (2): The signal pulse and pump pulse are temporally overlapped in the crystal. (3): A part of the signal pulse is reflected on the rear surface of the BBO crystal. (4): The reflected signal pulse is bounced again on the front surface of the BBO crystal. (5): The attenuated signal pulse is amplified by the residual part of the pump pulse. There exists in actual no pulse in front of the main pulse. A peak appearing in front of a main pulse in Fig. 5.13 (a) is caused by the symmetry of the intensity autocorrelation. It turns out from this result that the measured spectrum is the superimposed spectra of the multiple pulses amplified in the nonlinear crystal. The output energy is also the cumulated ones of a main pulse and following several post pulses. These post-pulses are usually suppressed by coating the anti-reflection (AR) layer on the amplifier medium. We solved this problem by use of a wedge-cut crystal as an amplifier medium. The detailed discussion is described in the section of a 20-kHz OPCPA demonstration. Fig. 5.13 (b) shows the FWHM of the autocorrelation trace for the main pulse as a function of the normal distance between two gratings. With increasing the grating distance, the grating provides a strong negative chirp to compensate the GDD of the glass-block compressor.

In summary, 1-kHz OPCPA has been demonstrated by use of a Ti:sapphire oscillator and a Nd:YLF pump laser. The amplification of stretched signal pulses with 95-ps pump pulses has been examined in NOPA geometry. A timing-jitter of less than 7.5 ps between the pump and signal oscillator was realized by use of an electrical synchronization setup. The stretched pulses were amplified in a type-I phase-matching BBO crystal in the non-collinear geometry, and compressed by use of a simple glass-block compressor. The amplification results showed possibilities of the even broadband amplification by optimizing the phase-matching condition and the even high power amplification with the additional amplifier stages. An important problem found in this demonstration was the multiple-pulse amplification caused by a reflection of the signal pulse in the amplifier crystal. Besides, the TOD as well as GDD must be compensated by use of another stretcher-compressor pair together with AOPDF to obtain transform-limited pulses.

5.4 20-kHz OPCPA

The 20-kHz OPCPA system is constructed based on the experimental results of the 1-kHz OPCPA system. The main differences of the 20-kHz OPCPA system from the 1-kHz OPCPA system are as follows.

- **The 1-kHz Nd:YLF pump source is replaced with a 20-kHz Nd:YVO_4 pump laser system.** This pump laser generates higher energy pulses with an excellent beam quality and shot-to-shot stability.

- **The normal slab BBO crystal is replaced with a new wedge-cut BBO crystal.** The internally reflected pulses are successfully suppressed by use of the wedged crystals.

- **A 2nd OPA stage is newly constructed in the system.** The even higher energy signal amplification is expected. It is necessary to suppress the amplification of the OPF at the 2nd stage.

- **The dispersion will be precisely managed by use of a newly designed grism stretcher and a glass-block compressor coupled with an acousto-optic dispersive filter.** This combination realizes the pulse compression down to the few-cycle regime.

5.4.1 20-kHz OPCPA system setup: Pump laser

The optical layout of our pump laser system is presented in Fig. 5.15 [158, 159]. It consists of an actively mode-locked diode-pumped neodymium-doped yttrium ortho-vanadate ($Nd:YVO_4$) oscillator, a pulse picker and a diode-pumped $Nd:YVO_4$ regenerative amplifier. The $Nd:YVO_4$ oscillator generates 23.0 nJ, 1064 nm laser pulses with 200 ps pulse duration at 80MHz. An etalon is introduced into the cavity to select longitudinal modes for controlling the pump pulse duration. The repetition rate is reduced from 80 MHz to 20 kHz by use of a pulse picker. In the pulse picker, the Pockel's cell selects one pulse and a half-wave plate compensates its polarization. The Faraday isolator blocks pulses reflected from the following amplifier. After the pulse picker, the pulses are amplified in the diode-pumped $Nd:YVO_4$ regenerative amplifier. The amplifier medium is pumped by a fiber-coupled diode laser. Pulses are amplified up to 1.8 mJ after ~5 roundtrips in the amplifier cavity. After the amplification the output pulses are frequency-doubled by use of a type-I phase-matching LBO crystal. The conversion efficiency of the frequency-doubling reaches 70 % at maximum. The output energy is controlled by using a

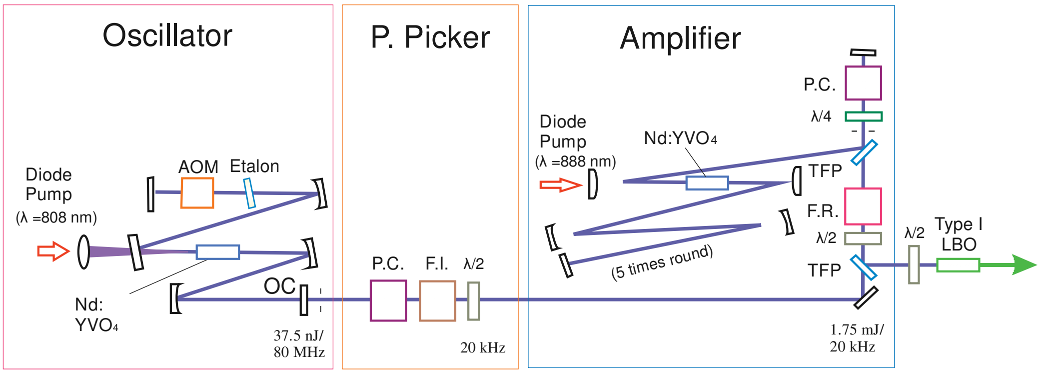

Figure 5.15: Layout of the 20-kHz pump laser system [158, 159]. The system consists of a mode-locked, diode-pumped $Nd:YVO_4$ oscillator and a diode-pumped $Nd:YVO_4$ amplifier. AOM: acousto-optic modulator, OC: output coupler, P.C.: Pockels cell, F.I.: Faraday isolator, $\lambda/2$: half-wave plate, P.D: photodiode, F.R.: Faraday rotator TFP: thin film polarizer.

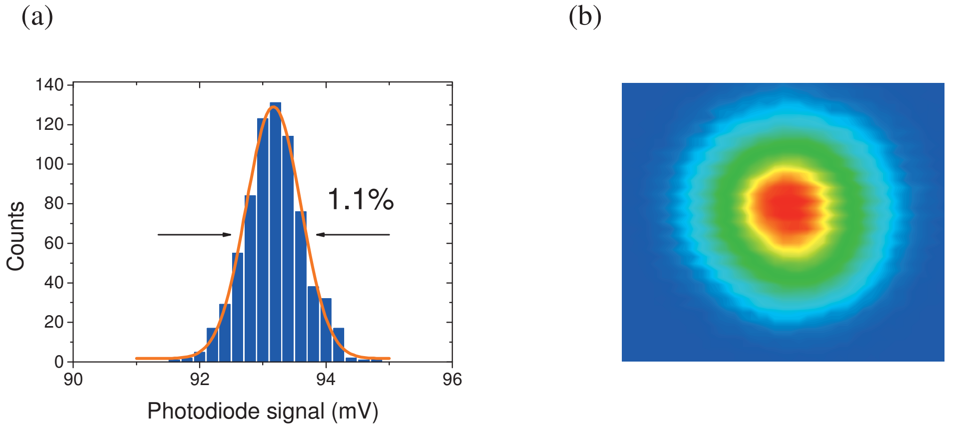

Fig. 5.16: (a) Shot-to-shot histogram of the output energy from the pump laser. The fluctuation in root-mean-square (RMS) is less than 1.1%. (b) Beam profile of the output pulses from the Nd:YVO_4 amplifier. M^2 value is 1.1 in both horizontal and perpendicular direction.

half-wave plate in front of the LBO crystal. The frequency-doubled beam is separated from the fundamental beam through the reflection on two dielectric mirrors. The pulse duration after the frequency-doubling is measured by use of an intensity autocorrelator. The final output pulse energy is 1.25 mJ with a pulse duration of 250ps at 532 nm. The shot-to-shot stability of the output energy is measured by counting the photodiode-detected pulse intensity. Fig. 5.16 (a) shows a histogram of a shot-to-shot output energy after the frequency-doubling in the LBO crystal. The pulse intensity has been counted for 30 minutes. The energy fluctuation of less than 1.1 % in root-mean-square (RMS) shows an excellent shot-to-shot energy stability. Fig. 5.16 (b) shows the pump beam profile at the 1st OPA stage measured by use of a CCD camera. The beam has a good quality with a M^2-value of 1.1 in both horizontal and perpendicular direction [159].

5.4.2 Wedge-cut nonlinear crystal

The multi-pulse amplification was a quite serious problem in our 1-kHz OPCPA system. Whether the internally reflected pulse is amplified or not depends on the balance between a crystal length and the pump pulse duration. If the pump pulse is short enough, the internally reflection problem can be avoided. OPCPA systems, however, employ ps-order pump sources, which causes the generation of multiple pulses. The use of an AR coated crystal is a common method to suppress these pulses. However, the anti-reflection for a broadband spectral range requires a very precise and fine coating technique. In addition, the damage threshold of the coating is generally lower than that of the nonlinear crystal itself. Another method for suppressing the multiple pulse amplification is to use a wedge-cut crystal, which varies the propagation direction of the internally reflected pulses and a main pulse. The amplification

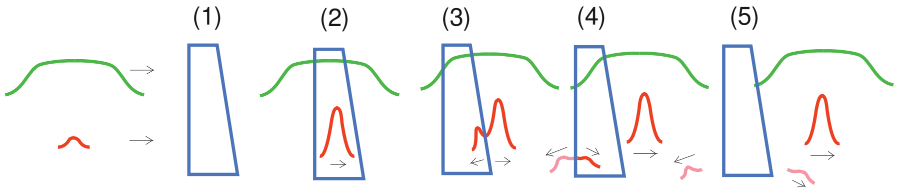

Figure 5.17: Beam propagation in a wedged BBO crystal. Due to the angled reflection in the crystal, the reflected pulses propagate in another direction. Compare this illustration with Fig. 5.14.

process in the wedge-cut crystal is illustrated in Fig. 5.17. (1): The conventional slab crystal is replaced with a wedge-cut crystal. The backside surface of this crystal has a certain angle against the front surface. (2): The signal and pump pulses are temporally overlapped in the wedge-cut crystal. (3): A part of the amplified signal pulse is reflected on the backside surface of the crystal. (4): The reflected signal pulse propagates in the other direction owing to a small tilt of the wedge surface. (5): The reflected signal pulses are removed from the optical path so that only a main pulse is successfully amplified. The wedged crystal in our system has a 5-mm thickness with the backside surface tilted at an angle of 6.0^{o} from the parallel plane of the front surface. In the following section, the amplification by use of this wedge-cut crystal is demonstrated and the amplification results are discussed in detail.

5.4.3 20-kHz OPCPA system: Optical layout

Fig.5.18 shows the optical configuration for our 20-kHz OPCPA system. The system consists of signal and pump laser sources, a grism stretcher, two amplifier stages and a glass-block compressor. The $Nd:YVO_4$ pump laser is synchronized with the Ti:sapphire signal oscillator by use of the same electrical devices as in 1-kHz OPCPA. 1.25-mJ, 250-ps green pump pulses are focused into amplifier crystals by use of relay-imaging telescopes. The beam diameter is set to 300 μm at the 1st stage and 250μm at the 2nd stage to compensate the pump depletion and the pump energy attenuation caused by the reflection on the mirrors and the 1st stage crystal. The pump intensity reaches 10 GW/cm^2 for both stages. Signal pulses from the Ti:sapphire oscillator are stretched to about 100 ps (650 nm - 1.0 μm) in the grism stretcher, which consists of a 651 lines/mm gold-coated reflective grating (Carl Zeiss Microimaging GmbH) and an anti-reflection coated SF57 glass prism (Hellma Optik GmbH). The diffraction efficiency of the grism stretcher is measured to be about 31 %. The wavelengths shorter than 690 nm are beforehand rejected in the following AOPDF because of the phase-mismatch in the BBO crystal at 532-nm pump-wavelength. 25-mm TeO_2 crystal in the AOPDF has a positive material dispersion, which compresses negatively chirped pulses to about 80 ps (690 nm - 1.0 μm). The transmission efficiency of the AOPDF is about 10 %. The signal pulse duration is set at around 1/3 of the

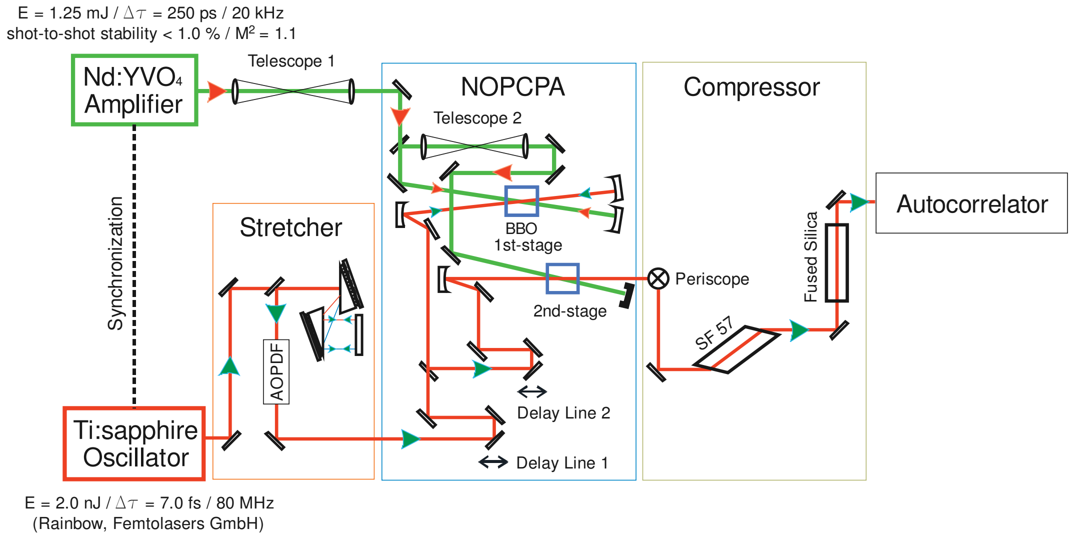

Figure 5.18: Optical layout of the two-stage three-pass 20-kHz OPCPA system. Dazzler: acousto-optic programmable dispersive filter, BBO: wedge-cut β barium-borate crystal, Telescope1: relay-imaged telescope for the 1^{st} stage, Telescope 2: relay-imaged telescope for the 2^{nd} stage.

pump pulse duration because the pump intensity variation becomes relatively small across the entire chirped signal pulse, which leads to a similar gain for all wavelengths and prevents the gain narrowing in the crystal [138]. The signal beam is amplified twice in the 1^{st} stage and once in the 2^{nd} stage. The pump beam and signal beam cross each other in the type-I phase-matching BBO crystal in non-collinear geometry. A tangential phase-matching (TPA) scheme is employed in this setup as well. The non-collinear angle and the phase-matching angle are initially set at about 2.24^{o} and 23.6^{o}, respectively. After this two-stage three-pass amplification in the OPA stages, the signal beam is collimated and sent to a glass-block compressor. This compressor consists of a Brewster-cut SF57 glass blocks and a fused-silica glass block. Because the fused-silica glass block has a much lower third order nonlinear susceptibility $\chi^{(3)}$ than the SF57 glass block, the self-action is not induced inside the fused-silica glass block with even shorter pulses.

5.4.4 Suppression of doubly reflected pulses

Intensity autocorrelation is plotted to check whether internally reflected pulses are suppressed. Fig. 5.19 plots the autocorrelation trace after the 2^{nd} pass at the 1^{st} stage amplifier with the 20-cm glass-block compression. Only one peak appears in a large scanning window over 500 ps. Because the scale of the intensity is set to a small value to detect the multiple pulses sensitively,

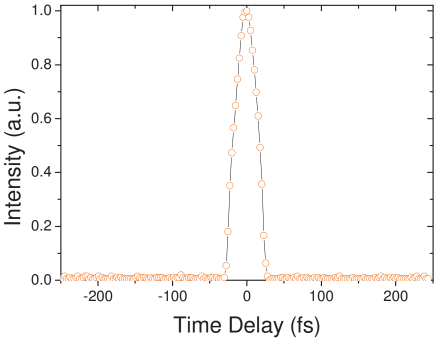

Figure 5.19: Measured autocorrelation trace for the wedged BBO crystal. Only one pulse is successfully amplified in the crystal. Compare this figure with Fig. 5.13.

the peak of the main pulse reaches the saturation regime. It turns out from this result that the wedge-cut BBO crystal successfully removes the internally reflected pulses. The amplification results exactly reflect the data for only the main pulse.

5.4.5 Amplification results

The pulse energies and spectra are measured after each system component at the maximum pump energy of 1.25 mJ. The Ti:sapphire oscillator generates signal pulses with the energy of 2.0 nJ. The pulse energy is reduced to 620 pJ after the grism stretcher. The energy is further reduced to about 50 pJ after the AOPDF. The stretched pulses are then amplified up to 50.0 μJ after the 2nd pass at the 1st stage. In order to suppress OPF, the pump and signal pulses are separated in time at the 2nd pass, which leads to the temporal shift of OPF out of the maximum gain regime. Consequently, the pulse energy is attenuated to 20 μJ before the 3rd pass at 2nd stage. The signal pulses are then fed into the 3rd-pass and are scaled to 175 μJ.

The normalized spectra from the signal oscillator and after the grism stretcher are shown in Fig. 5.20 (a) and (b), respectively. Since the spectrum in the range from 650 nm to 700 nm is not phase-matched in the BBO crystal, the spectral range is in advance selected from 700 nm to 1.0 μm in the AOPDF (Fig. 5.20 (c)). Spectra after the 1st pass and 2nd pass at the 1st stage and following 3rd pass at 2nd stage are shown in Fig. 5.20 (d), (e), and (f), respectively. The measured amplified spectra roughly maintain the same spectral bandwidth. The amplified spectra after the 1st, 2nd and 3rd pass support transform-limited pulse durations of 9.0 fs, 8.8 fs, and 8.1 fs, respectively. The gain narrowing at the 1st pass is due to the low-input signal amplification in unsaturated regime. The spectral broadening at the 3rd pass is a result of the back conversion process during the parametric amplification.

In OPCPA, the measurement of the OPF is one of the important themes. The incompressible OPF should be suppressed as weak as possible. At present, there is no direct method to measure

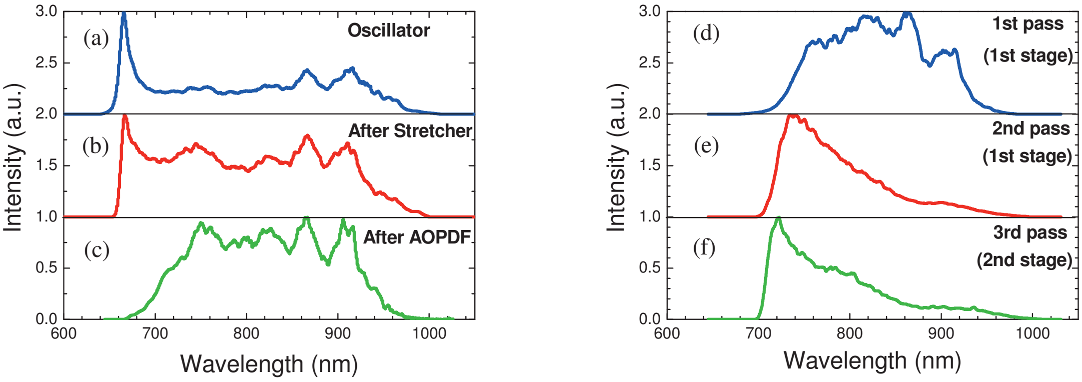

Figure 5.20: Measured output spectra of the signal pulse. (a): Oscillator spectrum, (b): spectrum after the grism stretcher, (c): spectrum after the AOPDF, (d): amplified spectrum after the 1st pass at the 1st stage, (e): amplified spectrum after the 2nd pass at the 1st stage, and (f): amplified spectrum after the 3rd pass at the 2nd stage. The transform-limited pulse has 8.1-fs FWHM pulse duration.

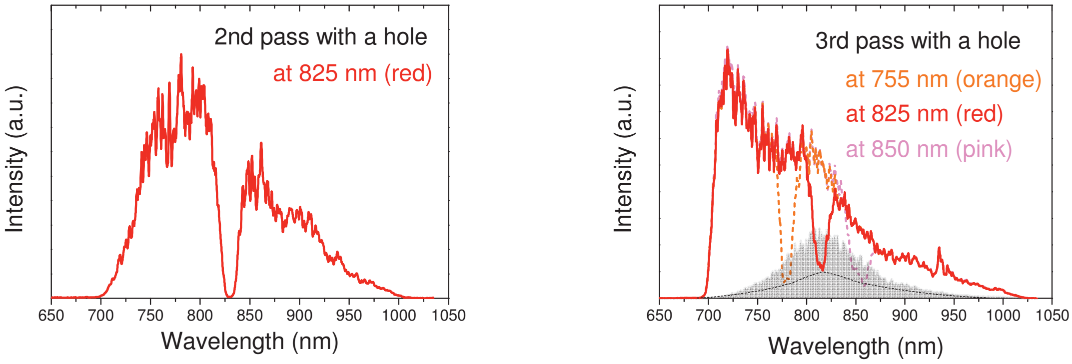
(a)

(b)

Figure 5.21: Measured output spectrum with a spectral hole. (a): after the 2nd-pass at the 1st-stage OPA stage and (b): after the 3rd pass at 2nd stage. Spectral holes are created at 775 nm (orange), at 825 nm (red) and at 850 nm (pink). OPF in the seed-unblocked case is also shown in this figure (gray).

the amount of OPF because of the spatial and spectral overlap of OPF with the amplified signal pulse. OPF observed by blocking the signal beam is expected to have much higher energy than in case the signal is not blocked. It is therefore necessary to estimate the energy amount of the signal-unblocked OPF. Recently, a method to estimate the energy of signal-unblocked OPF was reported in Ref. [160]. This method has its base on the principle for estimating the amplified spontaneous emission (ASE) level in a Ti:sapphire amplifier system [161]. A spectral hole is introduced into the amplified spectrum to measure the signal-unblocked OPF spectrum. The

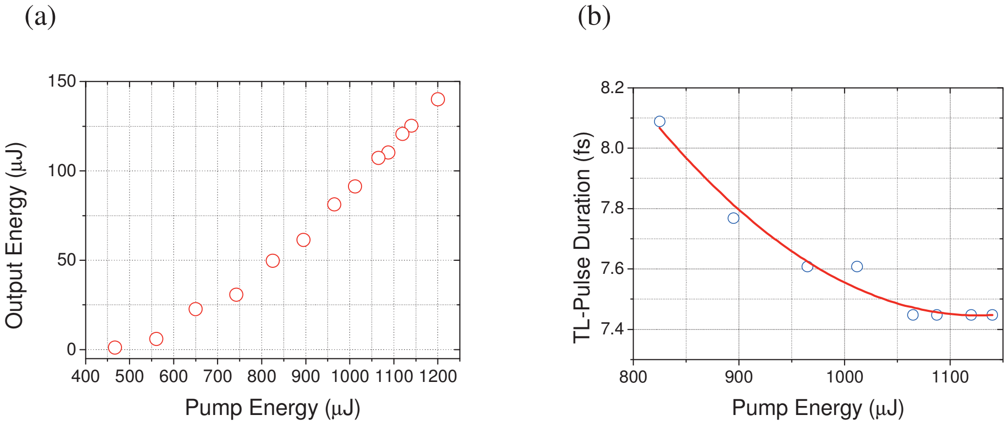

Figure 5.22 (a): Pump-energy dependent output energy after the 2^{nd} stage. The pump energy is changed by rotating the half-wave plate before the frequency doubling. (b): Pump-energy dependent transform-limited pulse duration. Circular points are measured data and solid line is the guide to the eye. As the pump energy is increased, the broadband spectrum is obtained. Around the energy of 1.1 mJ, the spectrum becomes the broadest.

energy of the signal-unblocked OPF is estimated by comparing the intensity of the OPF spectrum of the signal-unblocked case with that of the signal-blocked case. A zero-reaching spectral hole is introduced by placing a narrow block on the Fourier plane within the grism stretcher (Fig. 5.21 (a)). This spectral-hole-induced pulse is amplified in the OPA stages, except for the wavelength where the spectral hole is introduced. The spectral intensity at the bottom of the hole is increased due to the OPF generation. By measuring the depth of the spectral hole at different wavelengths across the spectrum, we can trace out the spectral distribution of signal-unblocked OPF and determine the OPF energy amount [160]. Fig. 5.21 (b) shows amplified spectra after the 3^{rd} pass amplification with a spectral hole at 775 nm (orange), at 825 nm (red) and at 850 nm (pink). The spectrum of the OPF in the signal-blocked case (gray) is also shown in this figure. It turns out from this result that OPF is scarcely measured at the 2^{nd} pass but mainly amplified at the 3^{rd} pass. The expected signal-unblocked OPF spectrum has about the half level of the spectral intensity for signal-blocked OPF (black line). The energy of OPF in the signal-unblocked case is therefore estimated to be the half of that in the signal-blocked case. The amount of signal-blocked OPF is diminished by carefully controlling the telescopes to decrease the pump intensity for the reduction of the gain at each OPA stage. The optimum signal output is experimentally found with a compromise between the high energy amplification and the OPF suppression. OPF has the energy of 70 μJ after the 3^{rd} pass when the signal beam is blocked before the first OPA stage. OPF in the signal-unblocked case is therefore estimated to be 35 μJ. The output energy of the amplified signal pulse is therefore estimated to include 140-μJ net energy without the OPF distribution. The pump-to-signal conversion efficiency is calculated to be 11.2 % and the quantum efficiency reaches 16.8 %. The signal output energy

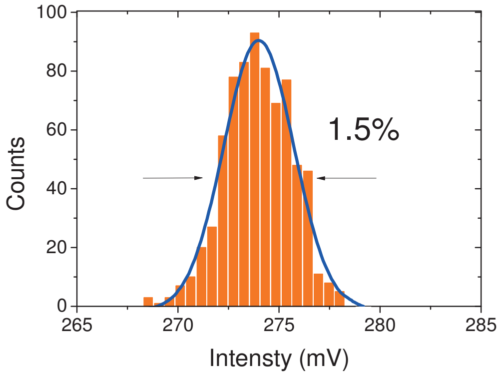

Figure 5.23: Shot-to-shot histogram of the output energy after the 2nd OPA stage. The measured time is more than 30 minutes. The fluctuation in RMS is less than 1.5 %.

dependence on the pump energy is shown in Fig. 5.22 (a). In this figure, the energy of signal-unblocked OPF is subtracted from the measured output energy. In the small pump energy region (500 μJ - 900 μJ) the signal pulse energy exponentially increases, while in the high pump energy region (900 μJ - 1.15 mJ) the signal pulse energy increases proportionally to the pump energy and the conversion efficiency becomes constant. The pump-energy-dependent amplification bandwidth is evaluated from the transform-limited pulse durations calculated from the amplified signal spectrum. Fig. 5.22 (b) shows the transform-limited pulse duration depending on the pump energy. With the increase of the pump energy, a short transform-limited pulse duration, i.e. a broadband spectrum is obtained. At the maximum pump intensity the shot-to-shot stability of the output energy is measured by use of a photodiode. Fig. 5.23 shows the shot-to-shot histogram of the amplified signal pulses over 30-minutes period. The energy fluctuation is less than 1.5% in rms. This result shows a good stability in the operation of the OPCPA system. After the amplification the signal pulses are compressed by use of a glass-block compressor, which allows the high transmission output energy of 125 μJ. The pulse duration after the compressor is characterized by use of an intensity autocorrelator.

5.4.6 Pulse compression

This section discusses the result of the pulse compression after our grism stretcher and glass-block compressor pair under the global-dispersion-balance design. The detailed discussion on the stretcher design and its photograph are shown in *Chapter 4.3.4*. The pulse compression is first achieved by use of a 350-mm SF57 glass-block and the remained dispersion is compensated by use of a 250-mm fused-silica glass-block. This stepwise compression prevents the undesired nonlinear interaction in the glass-blocks. Fig. 5.24 shows the scheme of the compressor and the following autocorrelator. Because the SF57 glass-block is cut into one bulk

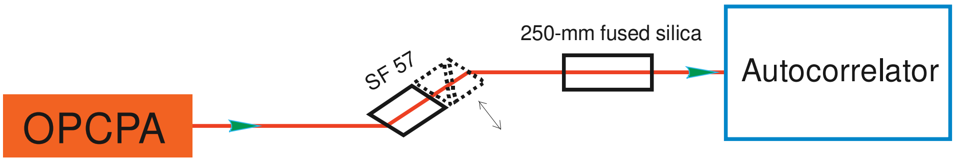

Figure 5.24: Optical layout of the pulse compressor. 350-mm SF57 glass-block and 250-mm fused-silica glass-block are employed as a compressor. The length of the SF57 glass-block can be controlled with a pair of prisms.

and a pair of prisms, the glass-block length is arbitrarily controlled around 350 mm by sliding one of the prisms. The minimum pulse duration is found by finely and precisely changing the glass-block length. Fig. 5.25(a)-(e) show several autocorrelation traces for different glass-block lengths. The pulse duration and the pulse shape are varied with changing the glass-block length. The trace (a) depicts the autocorrelation trace at the glass-block length of 331.0 mm. The pulse duration is measured to be 33.0 fs with a Lorentzian fitting. With a small increase of the glass-block length, the pulse duration is decreased (trace (b)). The shortest pulse of 15.4 fs is obtained at the glass-block length of 333.9 mm (trace (c)). At the even longer glass-block length, the autocorrelation trace becomes broader and a shoulder appears around the main pulse (trace (d)). Finally, the trace is strongly modulated in the longer glass-block as shown in the trace (e). The pulse duration for each glass-block length is summarized in Fig. 5.25 (f). Circles in the figure show the measured data points and the solid line is the guide to the eye. The shortest pulse duration is obtained at the optimum glass-block length (c). In such an ultrashort pulse regime, the influence of the pulse front tilting on the intensity autocorrelation measurement becomes effective. Because the two beams are non-collinearly focused into the crystal in the autocorrelator, the pulse front tilting causes the spatial pulse-duration change. It is investigated by checking the dependence of the pulse duration on the beam cross-section. Fig. 5.26 shows the autocorrelation traces for different aperture size before the autocorrelator. The aperture size is set to make the peak intensity of the autocorrelation trace by half and twice of the original intensity. The results show that the pulse duration is same for three aperture sizes, which indicates that there is no influence of the pulse front tilting on the autocorrelation measurement.

Although the glass-block thickness is optimized, there exists the pedestal at the both side of the autocorrelation trace in the full temporal widow of the autocorrelation trace. The pedestal has its origin in mainly fourth order dispersion remaining in the pulse. The high-order dispersion is compensated by use of an AOPDF. Fig. 5.27 (a) and (b) show the same autocorrelation traces at the optimum glass-block length in larger scanning range. The y-axis is shown (a): in the linear scale and (b): in log scale. The signal distribution has a duration of 1.2 ps, which is within the working window of the AOPDF (3.0 ps). In the next chapter, we report the details of the compensation of the higher-order dispersion by use of a novel phase-detection and phase-compensation method.

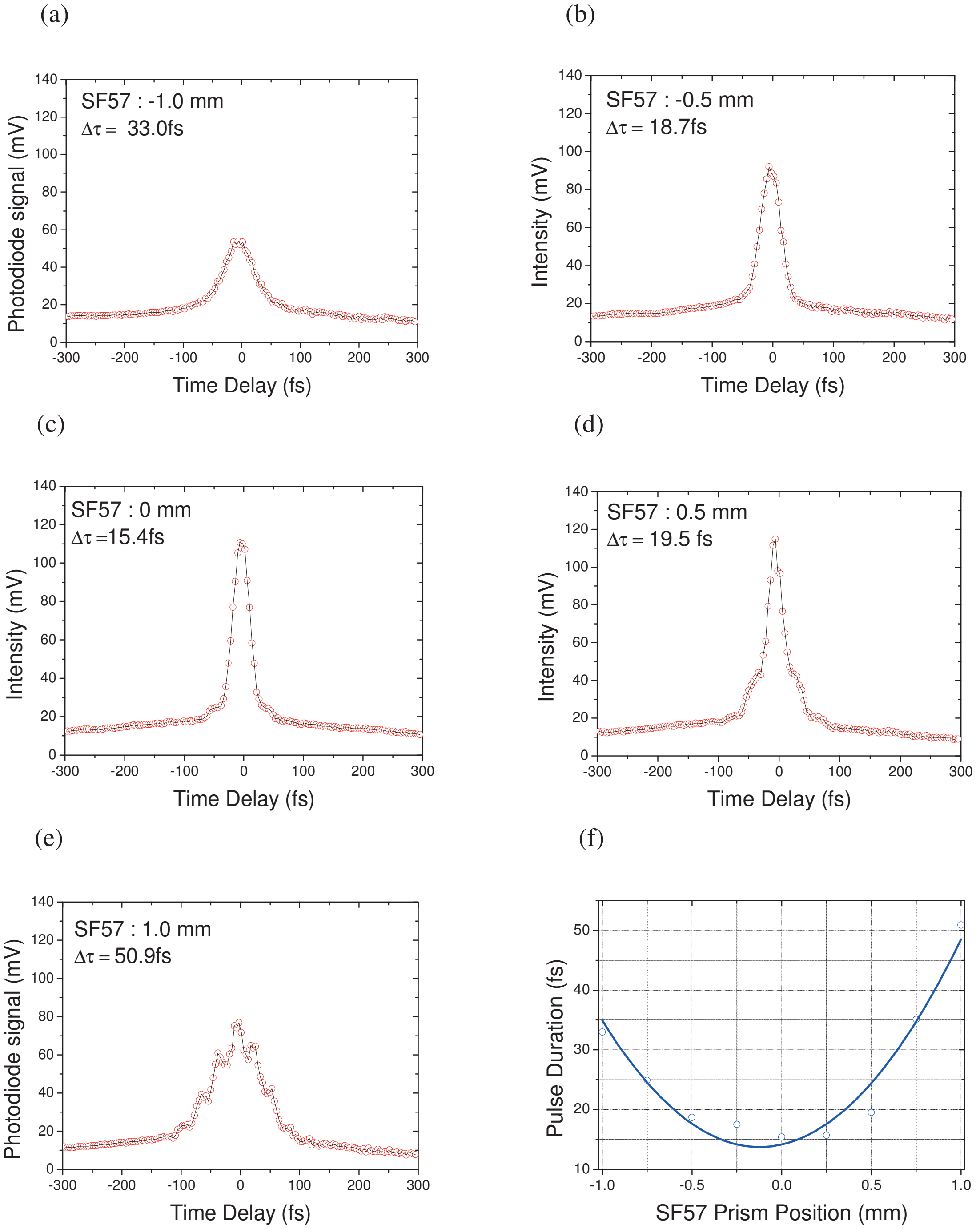

Figure 5.25: Measured autocorrelation traces for each glass-block length are fit with a Lorentzian. Relative position from the optimum glass-block length of (a): -1.0 mm, (b): -0.5 mm, (c): 0 mm, (d): 0.5 mm, and (e): 1.0 mm, respectively. (f): Glass-block-length dependent pulse duration. The shortest pulse has the duration of 15.4 fs, where the highest peak intensity is obtained.

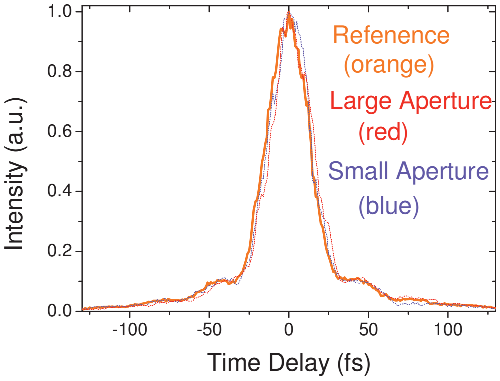

Figure 5.26: Measured autocorrelation traces for different aperture sizes in front of the autocorrelator.

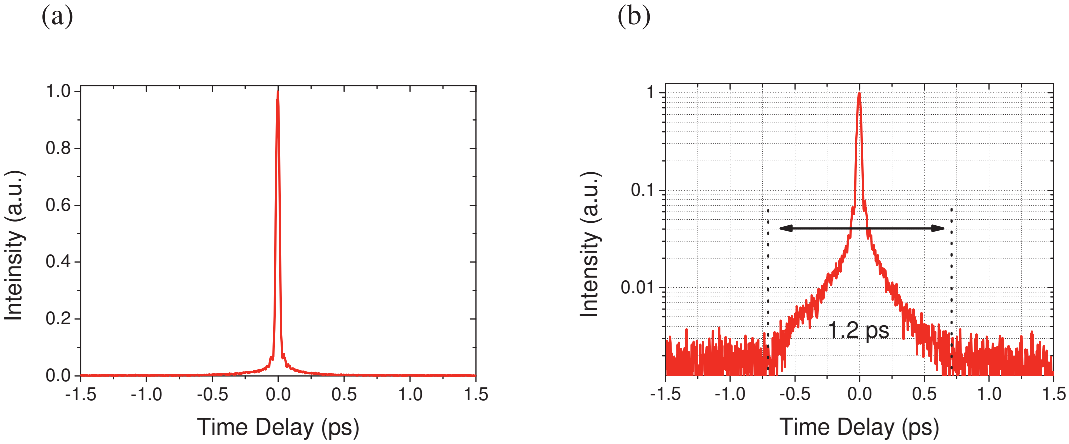

Figure 5.27: Measured autocorrelation trace in the temporal scale of 3.0 ps. Both figures show the same trace but the y axis is shown in (a): a linear scale and (b): a log scale. The temporal signal distribution is clearly observed in (b). The pedestal of the pulse has the duration of 1.2 ps.

Chapter 6

Optimized compression

Pulse compression down to a few-cycle regime is realized by managing the dispersion up to higher orders. The goal of this chapter is to compensate the dispersion up to 5th order and compress the pulse even shorter down to sub-10 fs. An adaptive dispersive device is used to compensate the dispersion under the global-dispersion-balance design. The residual phase information is obtained by means of a multi-photon intrapulse interference phase scan (MIIPS) method. Based on the MIIPS trace, the residual phase is fed back to the adaptive dispersive device. A small amount of the dispersion is step by step added to the original phase and finally a few-cycle pulse is obtained. The pulse pedestal is successfully suppressed after the final compression. After the MIIPS measurement, the pulses are characterized by use of FRAC.

6.1 Adaptive dispersion compensation device

Traditional compression techniques only provide GDD and sometimes TOD by use of gratings or prisms [162]. The residual dispersion induced in the CPA system is often compensated by adaptive dispersive devices, which have the flexibility in managing dispersions by arbitrarily and precisely providing a certain amount of dispersions. The optimum compression aims at the removal of spectral phase distortions accumulated by the propagation through dispersive media [96]. Ultimately a clean-shaped transform-limited few-cycle pulse is obtained with a flat phase over a broadband spectral range. In following sections we introduce two representative adaptive dispersion devices.

6.1.1 Spatial light modulator (SLM)

The spatial light modulator (SLM) is a widely used device to manipulate the spectral phase [163]. An advantage of the SLM is its higher transmission efficiency compared to a pulse shaper based on the acousto-optic modulator. The optical configuration of the SLM is basically same as the grating-based pulse stretcher. The only difference is that a phase mask is placed in the Fourier-plane at a distance f behind the first lens and the gratings. Lenses are mirror-imaged set to give exactly zero dispersion, which spatially separates all the frequencies on the Fourier plane. This $4f$ -setup enables the individual frequencies to be focused next to each other on a line. By placing a phase mask in the plane, the spectral properties of the pulse can be manipulated directly in the frequency domain. The mask modulator consists of an array of cells filled with liquid crystals. A voltage is applied to each pixel to orient the molecules in the liquid crystal, in which each optical wave experiences different refractive index and transparency. The pulse consequently receives a temporal modulation due to the different propagation speed of each frequency component in the liquid crystal. When the phase information is exactly known in advance, the proper phase modulation in the SLM approaches the flat phase. The SLM however requires a rigorous alignment and a relatively large space compared to the acousto-optic dispersive devices.

6.1.2 Acousto-optic programmable dispersive filter (AOPDF)

The acousto-optic programmable dispersive filter (AOPDF) is a recent dispersive for dispersion compensation [164-166]. It consists of a birefringent crystal and an acousto-optic modulator. The birefringence in the crystal induces a difference in propagation speed for each polarization in the crystal. Fig. 6.1 shows the schematic representation of the AOPDF principle [165]. A piezo transducer is mounted on the one side of the crystal to generate an acoustic wave. The incident beam propagates as an ordinary wave in the crystal. The phase-matching condition $k_e = k_o + k_a$ is satisfied in the crystal, where k_e, k_o and k_a are the wave number of extra-ordinary wave, ordinary wave, and acoustic wave, respectively. An optical wave coupled with an acoustic wave changes the polarization and experiences a different refractive index. Each wavelength component is transformed from the ordinary wave to the extraordinary wave at different position due to the chirp in the acoustic wave and experiences a different amount of optical distance in the TeO_2 crystal. The difference in the group-delay for each wavelength in the crystal results in the spectral phase control. The amplitude of the acoustic wave decides the conversion efficiency and therefore modulates the signal spectrum. The AOPDF operates much faster than the SLM system with a compact setup. In our OPCPA system, the AOPDF is set between the grism stretcher and the 1st OPA stage. It compensates for the dispersion in 3.0 ps range.

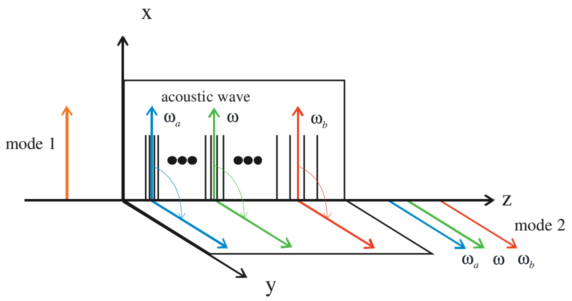

Figure 6.1: Schematic representation of the AOPDF principle. An optical axis is in the direction of the x-axis. The ordinary wave and extra-ordinary wave are represented as mode 1 and mode 2, respectively [165].

6.2 Pulse compression methods

Both a precise measurement for the spectral phase and a fine manipulation of the dispersion are essential for the optimized compression. For the phase measurement, the FROG and SPIDER technique are widely used in many laboratories because these sophisticated techniques provide reliable phase information. In addition, the algorithms for retrieving the phase are commercially available. However, in the novel global-dispersion-balance design of the stretcher-compressor pair, a large amount of the residual dispersion is left in the pulse, and there are some difficulties in measuring the spectral phase by use of such techniques. For example, in the FROG technique a large amount of data points are required to obtain a transform-limited pulse. Because the pulse duration of a few-cycle pulse is several fs, the measurement demands quite small sampling steps although it needs a large scanning range. It takes therefore a considerable time for canning the whole trace. In addition, the phase-retrieval requires the iterative-loop-algorithm, which is not suitable for the real-time pulse-compression measurement. In the SPIDER technique, it is advantageous that no iterative algorithm is needed for the phase retrieval, but the measurement always demands a pulse reconstruction because the interference-fringe data is not intuitive. In addition, a precise calibration of the spectral shear and the relative delay between two replicas are essential. Compared to these two techniques, the MIIPS technique is advantageous to obtain the phase information in several points. First, the dispersion order and its approximate amount can be immediately determined from the intuitive MIIPS trace. MIIPS requires no complicated phase-retrieval algorithm, which is suitable for the real-time operation. The estimated dispersion is fed back to the AOPDF and the residual dispersion is step by step compensated until a transform-limited pulse is obtained. Second, because the dispersion is read from the shape of the plots, the MIIPS measurement is insensitive to the energy fluctuation. Finally, this technique operates quite easy with a simple setup. It requires no any additional components such as gratings or lenses. Because the AOPDF has been already set in our OPCPA system, we need only a non-linear crystal and a spectrometer. The MIIPS technique is therefore a great candidate for both the phase detection and the optimum pulse compression, coupled with an adaptive dispersive device. In the next section the simulated MIIPS traces are shown by use of self-developed software [167]. Based on these simulation results, the residual spectral phase is experimentally compensated. After the final MIIPS optimization, the pulse duration is measured by use of FRAC.

6.2.1 MIIPS simulation

This section briefly shows simulation results for the two-dimensional MIIPS trace. The analytical consideration and discussion on the simulation traces are provided in detail in Ref. [167]. A sinusoidal function is commonly used as a reference function as mentioned in *Chapter 2.5.5*. The scanning parameter δ in Eq. (2.30) is described in two forms:

$$\delta = \begin{cases} 2n\pi + \gamma(\omega-\omega_0) + a\sin[\frac{\phi_2(\omega)}{\alpha\gamma^2}] \\ \\ (2n+1)\pi + \gamma(\omega-\omega_0) - a\sin[\frac{\phi_2(\omega)}{\alpha\gamma^2}] \end{cases} \qquad n \in \mathrm{int} \cdot \qquad (6.1)$$

where α is the amplitude of the function, γ decides the frequency of the sinusoidal wave, ω_0 is the central wavelength to be characterized. These equations have solutions only when $|\phi_2/\alpha\gamma^2| < 1$ is satisfied. Therefore the optimum value of $\alpha\gamma^2$ must be carefully chosen to correctly measure the phase. Because the choice of γ value depends on the pulse bandwidth and is usually set to the temporal bandwidth of the transform-limited pulse, the value of α is adjusted to optimize the whole value of $\alpha\gamma^2$. Under the condition that $\alpha\gamma^2$ is much larger than ϕ_2 ($|\phi_2/\alpha\gamma^2| << 1$), the last term asin($\phi_2/\alpha\gamma^2$) simplifies to $\phi_2/\alpha\gamma^2$. In the following simulations, a Gaussian spectrum with the central wavelength of 800 nm is considered as a fundamental spectrum and the dispersion from 2nd- to 5th-orders is introduced into the flat spectral phase.

The simulated MIIPS trace for a transform-limited pulse is shown in Fig. 6.2 (a). A holizontal dash-line set at 400 nm indicates the central wavelength of the second harmonics signal. Slanted dashed lines equally spaced at intervals of π with the same slope correspond to zero-dospersion trace. The MIIPS plots are completely overlapped with the slanted dashed lines. They become guidelines when the dispersion is introduced into a flat phase. Because the trace is depicted in wavelength, plots are not straight lines but slightly curved. This trace is simulated on condition that $\alpha = 3.0\pi$ and $\gamma = 8.0$ fs. The scanning range from 0 to 4π results in plotting two replicas, which ensures the certainty of the measurement. The color of the contour depicts the intensity of the measured spectrum for the second-harmonics signal.

First, a positive GDD is introduced into the flat phase. Fig. 6.2 (b) shows the simulated MIIPS trace with a positive GDD of 500 fs^2 introduced into the original flat phase. The simulated plots are still parallel to each other, but the distances between these plotted lines are no longer equal. The distance depends on the amount of the GDD added to the original phase. If a negative GDD is added to the original phase, the two lines shift in the opposite direction. The guidelines are therefore a criterion to decide whether the dispersion is positive or negative.

Next, a certain amount of positive TOD is introduced into the transform-limited pulse. Fig. 6.2 (c) shows the simulated MIIPS trace with the introduction of a positive TOD of 3×10^3 fs^3. The TOD induces the line-tilting around the central wavelength but it doesn't lead to a shape modulation. Because the TOD leads to a linear dependence of ϕ“ in Eq. (6.1), the plotted lines linearly depend on the second harmonics frequency. A positive TOD tilts the lines such that the two plotted lines are separated far away at long wavelengths and approach closer at short wavelengths. On the contrary, a negative TOD tilts these two lines in the opposite direction through the guidelines.

The dispersion orders more than TOD change the plot itself. When a certain amount of FOD is introduced into the original phase, curved structures are induced in the trace. Fig. 6.2 (d) plots the MIIPS trace when a positive FOD of 3×10^4 fs^4 is introduced into the flat phase. Because ϕ“

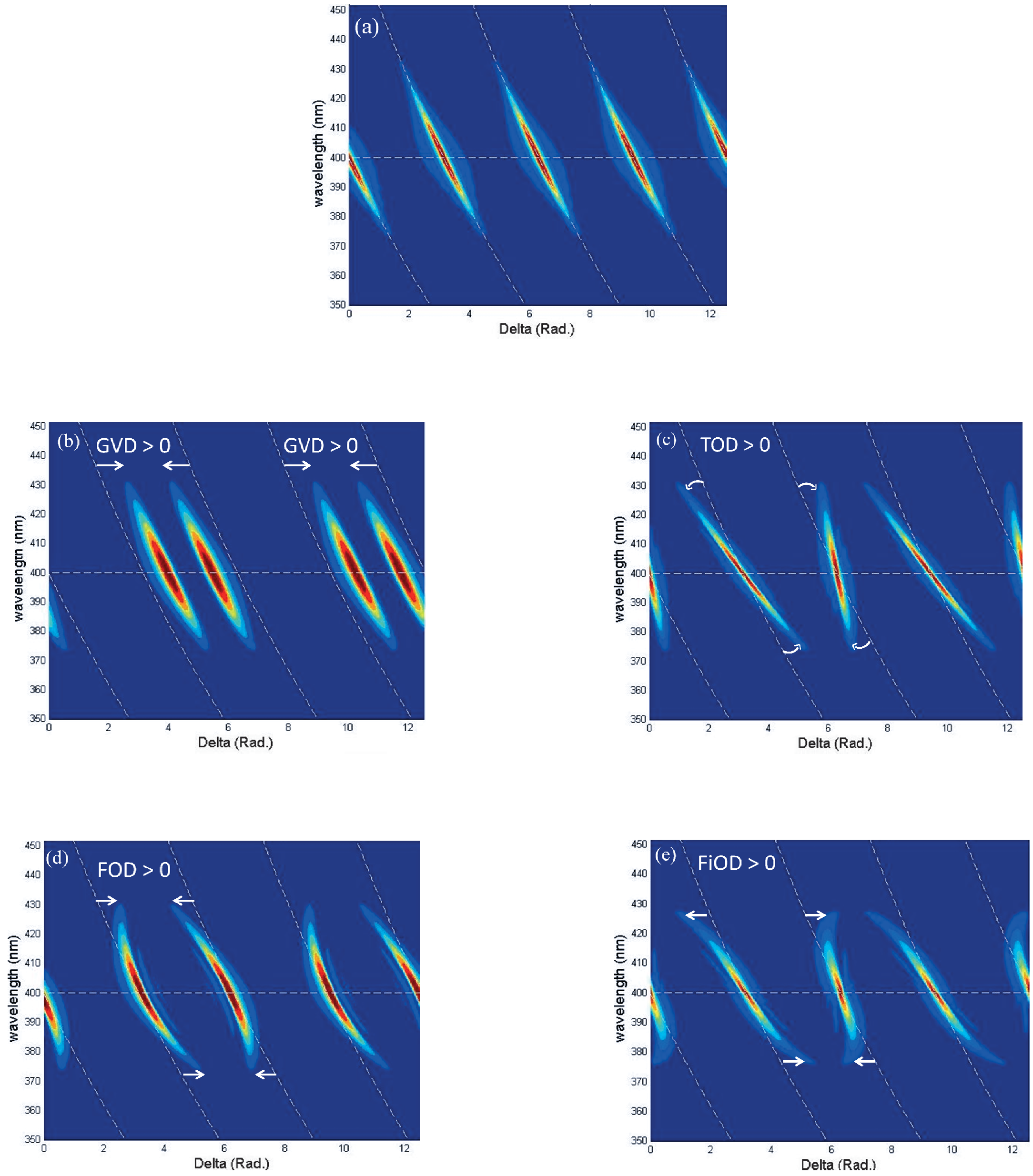

Figure 6.2: Simulation results of MIIPS traces for different dispersion orders. Horizontal line at 400 nm indicates the central wavelength. Lines parallel to the trace are guidance for the pulse compression. (a): Transform-limited pulse ($\alpha = 3.0\pi$ and $\gamma = 8.0$ fs) (b): positive GDD of 500 fs^2. (c): positive TOD of 3×10^3 fs^3. (d): positive FOD of 3×10^4 fs^4 (e): positive FiOD of 1×10^5 fs^5. ((b)-(e) $\alpha = 4.0\pi$ and $\gamma = 8.0$ fs)

term becomes a parabolic versus frequency, the two lines show a parabolic dependence on the second harmonic frequency. If a large amount of a positive FOD is introduced into the fundamental phase, the edges of two lines are strongly curved and finally a circular plot is obtained. Generally, the odd-order dispersions make the trace cross through the guidelines at the interaction points at the central wavelength and the even-order dispersions make the trace located one side of guidelines. The introduction of a negative FOD leads to the line curvature in the other direction of the guidelines. In contrast to the TOD, the FOD plots the trace located one side of the guideline without crossing through it.

Finally, a fifth-order dispersion (FiOD) is introduced into the transform-limited pulse. The FiOD is the highest dispersion that can be detected by MIIPS. Eq. (6.1) consists of the linear and cubic terms of the frequency. Fig. 6.2 (e) shows the MIIPS trace for a positive FiOD of 1×10^5 fs^5. The cubic term of ϕ“ causes “S”-like traces crossing the guideline. The exact information on the dispersion for even higher orders is difficult to obtain because the trace of the high-order dispersion is no longer unique and therefore resembles that of the above 2nd- to 5th-order dispersion.

6.2.2 Experimental results

The MIIPS simulation in the previous section has visualized the dispersion by introducing a certain amount of the dispersion into the flat spectral phase. When it comes to the pulse characterization, the experimental procedure goes backward: the dispersion order and its amount in the original phase are measured from the MIIPS trace and a proper amount of the dispersion is step by step added to the residual phase to approach the transform-limited pulse.

The dispersion in the AOPDF is initially set at -2000 fs^2 to maintain a reasonable diffraction efficiency of the AOPDF. The glass-block compressor is first set at the optimum length where the shortest pulse of 15.4 fs is obtained without the help of the AOPDF phase-compensation. The residual dispersion after the glass-block compressor is first measured by scanning the MIIPS trace. Fig. 6.3 (a) shows the first trial of the MIIPS scanning before the dispersion compensation. The values of α and γ of the reference function are set to 3π and 8.0 fs, respectively. The measured MIIPS lines are so strongly modulated that the top and the bottom of two lines are combined each other to form circles. This strong modulation is caused from the FOD remaining in the residual phase. It turns out from the simulation result that a positive FOD must be fed back to the AOPDF (See Fig. 6.2 (d)). After several trials, the trace is modulated from the circular to the curved structures as shown in Fig. 6.3 (b). In this trace the first and second lines are tilted to right and left side of the guideline, respectively. The compensation of the FOD is still not complete, but the main dispersion order remaining in the residual phase is altered to the TOD. This strong negative TOD is compensated by adding a positive TOD to the residual phase, which results in the orientation of the lines parallel to the guidelines. Fig. 6.3 (c) shows the MIIPS trace after the optimization of the TOD. The measured data are depicted with

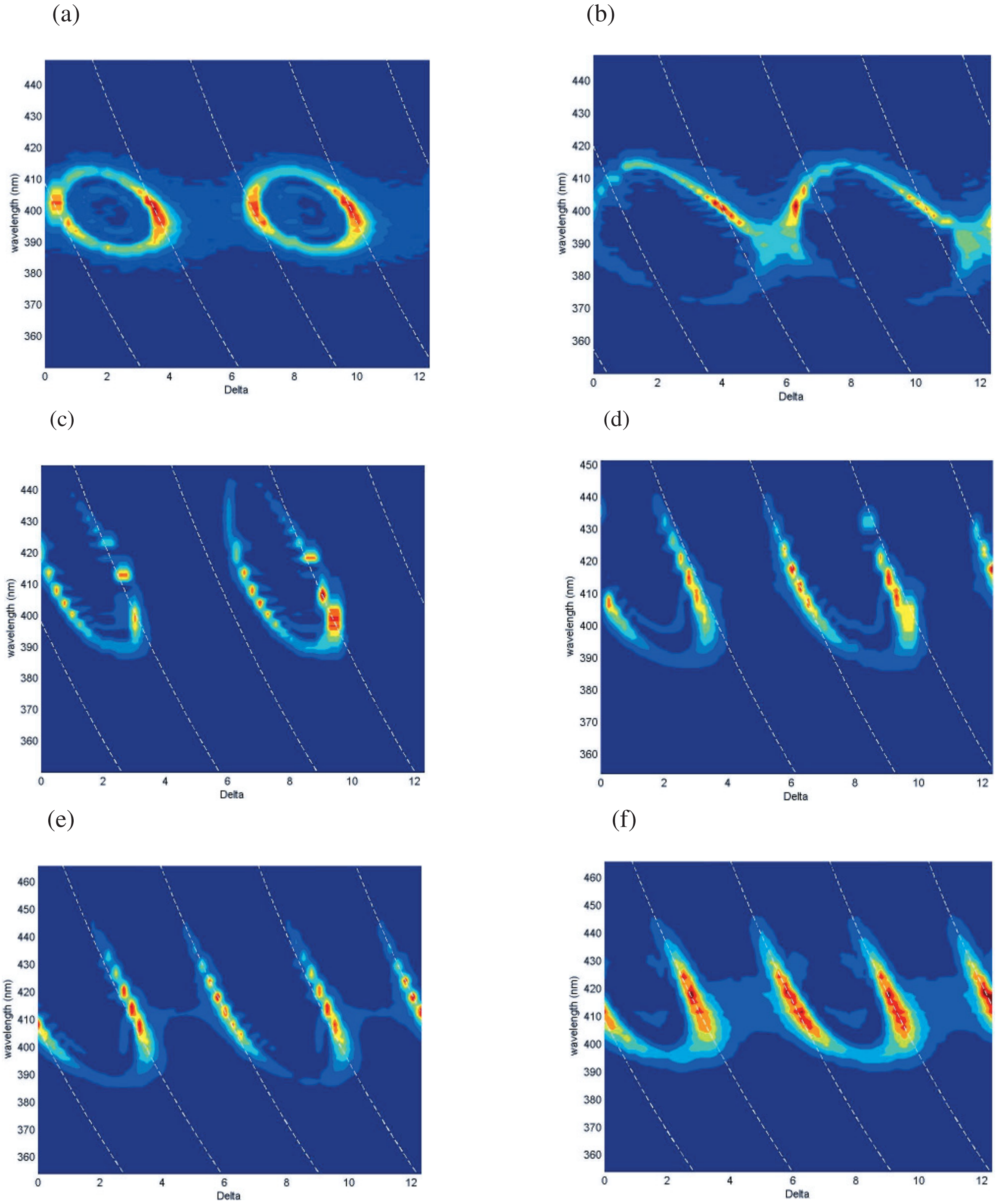

Figure 6.3: Measured MIIPS traces of the output pulses from the OPCPA system. (a): Trace for pulses compressed without AOPDF. Parameters in the sinusoidal function are set such that $\alpha = 3\pi$ and $\gamma = 8.0$ fs. (b)-(d): Trace for pulses after the partial compensation of (b): FOD, (c): TOD, and (d): GDD. (e): Fine GDD compensation by use of the AOPDF. (f): $\alpha = 1.5\ \pi$ and $\gamma = 8.0$ fs.

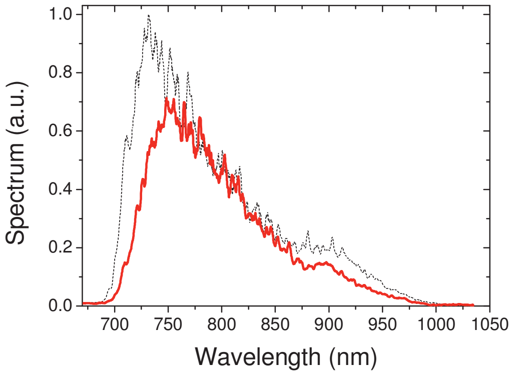

Figure 6.4: Measured spectrum after the pertial compensaiton of the FiOD. Further phase compensation results in the low diffraction efficiency of the AOPDF.

points along the trace lines due to a lack of the resolution caused by the large step of scanning parameter δ. This figure indicates that there remains a negative GDD because the plots are not overlapped with the equally spaced guidelines. In order to leave an enough working window for the AOPDF to compensate the high-order dispersion, the glass-block compressor is continuously used to compensate the GDD. The negative GDD is compensated by changing the glass-block length. The plotted lines are moved parallel to the guidelines and roughly overlapped with them (Fig. 6.3 (d)). Precise optimization of the GDD is carried out by using the AOPDF (Fig. 6.3 (e)). In addition, the 5th-order dispersion (FiOD) is introduced to reform the plots parallel to the guidelines in this figure. The final MIIPS trace is obtained as shown in Fig. 6.3 (f). There still remains the high-order dispersion in the compressed pulses, but the even compensation of this pulse is not carried out because the further compensation with the AOPDF leads to a low diffraction efficiency. Fig. 6.4 shows the spectral modulation of the amplified pulse after the FiOD compensation. The dotted line shows the amplified spectrum before the MIIPS measurement, while the red line after the MIIPS measurement with 5^{th}-order dispersion compensation. Further FiOD and even high-order dispersion compensation induce low diffraction efficiency. In this successive MIIPS operation, the central spectrum has been set to $\lambda = 865$ nm because the pulse compression with the MIIPS measurement was first checked in the infrared part of the pulse spectrum due to the easiness (See Ref. [167].). However, because the peak intensities of the second-harmonics spectra at the beginning are around the wavelength of 400 nm (Fig. 6.3 (a)), it is the best choice to set the central wavelength at 800 nm.

Fig. 6.5 (a)-(c) show the FRAC traces (a): after the FOD compensation, (b): after the FOD, TOD, and GDD compensation, and (c): after the FOD, TOD, GDD, and partial compensation of the FiOD. Fig. 6.5 (a) indicates that the GDD and odd-order dispersion are left in the pulse. In Fig. 6.5 (b), the GDD is obviously compensated but there still remains the FiOD. It is clearly shown in Fig. 6.5 (c) that the modulations in the wings of both sides vanish when the odd-order

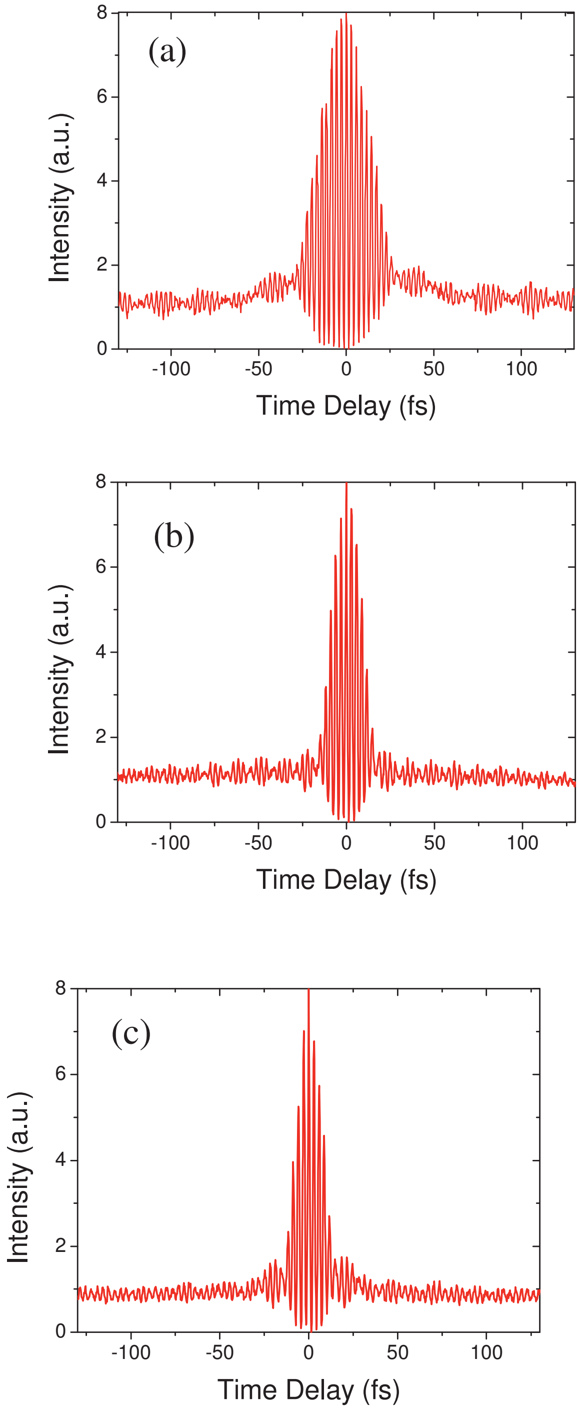

Figure 6.5: Measured FRAC trace (a): after FOD compensation, (b): after FOD, TOD, and GDD compensation, and (c): FOD, TOD, GDD, and partial FiOD compensation.

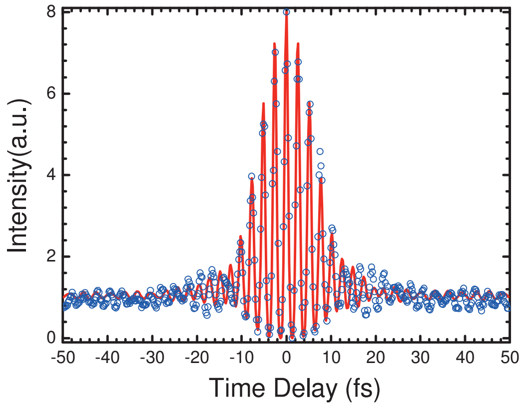

Figure 6.6: Same FRAC trace as Fig. 6.5 (c) with a temporal window from -50 fs to 50 fs. Circular points are measured data and a solid line is the simulated FRAC trace with a direct searching method.

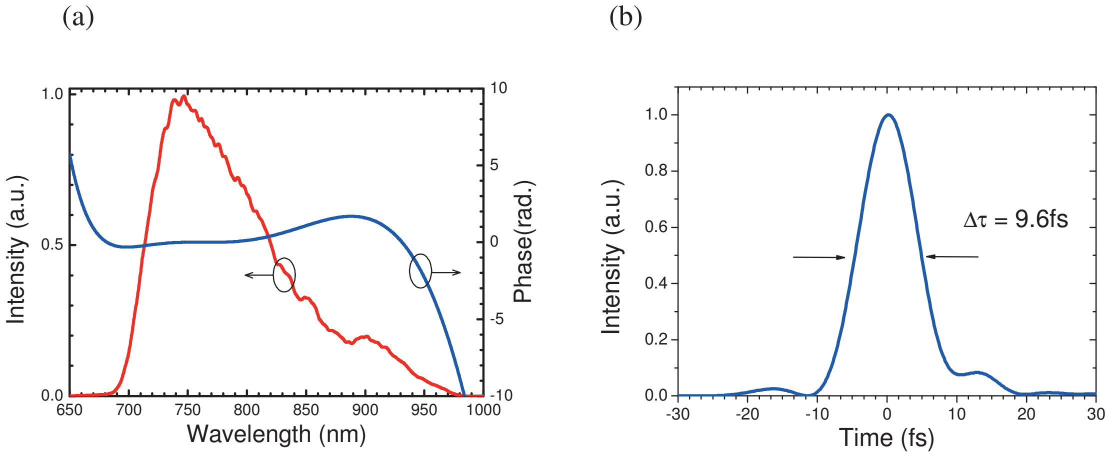

Figure 6.7: Amplified signal pulse after the compression: (a) Measured signal spectrum and the retrieved spectral phase. (b) Reconstructed temporal intensity envelope and its phase. The reconstructed pulse has a duration of 9.6 fs with Gaussian and 8.0 fs with Lorenzian fitting.

dispersion is compensated. Fig. 6.6 shows the same FRAC trace as Fig. 6.5 (c) in the temporal window within 50 fs. The spectral phase is calculated from the FRAC trace with a direct-searching method [168]. The solid line in the trace shows the numerically fitted FRAC trace. A good agreement between the experimental data points and fitting is achieved. The measured spectrum and retrieved spectral phase are shown in Fig. 6.7 (a). The retrieved spectral phase shows that a part of the fifth order dispersion still remains in the compressed pulses particularly at longer wavelengths. Fig. 6.7 (b) shows the reconstructed temporal intensity profile with the pulse duration of 9.6 fs at FWHM.

6.3 Summary

We have successfully compressed the amplified pulse down to sub-10 fs by use of the MIIPS technique. The simulation results revealed that the dispersion order and its amount were successfully visualized through the MIIPS trace. Based on the simulation results, the residual phase has been estimated and fed back to the AOPDF. The residual phase was step by step compensated up to 5th-order. Under the global-dispersion-balance design, the GDD was still compensated by use of the glass-block compressor, while a large amount of higher-order dispersion was compensated by using the AOPDF. This allowed the residual dispersion to be suppressed within the working window of the AOPDF during the MIIPS measurement. The FiOD is partially compensated due to the attenuation of the diffraction efficiency and the following spectral modulation. The pulse reconstructed from the FRAC trace showed the pulse duration of 9.6 fs.

CHAPTER 7

Conclusion and outlook

This thesis has reported the development of a high-average-power infrared few-cycle pulse OPCPA system. The laser output shows sub-10 fs, 125 μJ pulses generated at a repetition rate of 20 kHz with an average power of 2.5 W and a pulse peak power of 13 GW. This laser source is unique in that a global-dispersion-balance design has been applied to a high-repetition-rate OPCPA system. The global-dispersion-balance design of the grism stretcher has realized a large stretching ability of more than 10^4 and provided pulses more than 80 ps duration with a bandwidth from 690 nm to 1010 nm in a compact system. Such a large stretching ability shows the feasibility for further energy scaling. This laser system will serve to generate high-average-power XUV, soft x-ray pulses through the HHG process. Ultrashort soft x-ray sources with a high photon-flux have many possible applications such as ultrafast soft x-ray photoelectron spectroscopies and high-resolution soft x-ray microscopies. We have approached this laser performance through theoretical considerations and step-by-step experimental trials.

We have first simulated the dynamics of the propagating wave in a nonlinear crystal. A BBO crystal was chosen as an amplifier medium due to its large nonlinear coefficient, high damage threshold, and large transparency range. The simulations in a small signal gain regime have shown a great sensitivity of the gain spectrum to the non-collinear angle and the phase-matching angle. The crystal thickness and the pump intensity also determine the gain bandwidth and its spectral shape. It turned out from these simulations that a thin crystal with a high pump intensity was desirable. A two-stage OPCPA has been simulated by use of modified coupled-wave equations, in which the non-collinear angle and the pump walk-off are taken into account. The simulation result revealed the spectral gain-narrowing in the first stage and the spectral broadening in the saturation regime due to the back conversion. A suitable crystal thickness was determined by not the output power but the energy-bandwidth product (EBP). Because of the phase broadening in the back conversion regime, the optimum crystal thickness was a little longer than the position of the maximum output power.

Next, we have dedicated to the dispersion management of the extremely broadband spectrum extending to more than 300 nm. The down-chirp scheme was employed as a stretcher-compressor system. The selection of the grism stretcher as a stretcher and a SF 57 glass block as a compressor has realized a large stretching ability and a very high transmission efficiency of the compressor. Compared to the conventional TOD/GDD-matching design, the global-dispersion-balance design has realized a further increase of the stretching factor of more than 10^4 and extended the tunable bandwidth of the AOPDF from 690 nm to 1010 nm. The grism stretcher and glass-block compressor in a global-dispersion-balance design promise a feasibility of the high energy scaling of few-cycle pulses in OPCPA.

Based on the simulation results on the non-collinear optical parametric interaction and the stretcher-compressor design, the beam path of the high-repetition-rate OPCPA laser system was constructed. The system has been built up in two steps: first at 1 kHz with a commercial frequency-doubled Nd:YLF pump source, and then at 20 kHz with a home-built mode-locked frequency-doubled Nd:YVO_4 pump source. We first characterized the single-stage 1-kHz OPCPA by evaluating the achievable spectral bandwidth, the pulse compression, and the pulse energy. The system has amplified the signal pulses over a broadband spectral range at the central wavelength of 750 nm. The multi-pulse amplification caused by the doubly-internally reflection in the crystal has been observed in the autocorrelation measurement. In 20-kHz OPCPA, the multi-pulse amplification was suppressed by use of a wedged BBO crystal. A 2nd stage was newly constructed, and the dispersion was precisely managed by use of the grism stretcher and the glass-block compressor. In a global-dispersion-balance design, the grism pair has succeeded to stretch the pulses with a high stretching factor of more than 10^4 and the high-transmission glass blocks have compressed the amplified pulses down to 15.4 fs FWHM without the help of an adaptive dispersive device. OPF was measured by the spectral-hole method and was suppressed down to 35 μJ. The three-pass two-stage OPCPA succeeded to amplify the signal up to 175 μJ and therefore the net energy without OPF was estimated to be 140 μJ. After the compressor the output pulse energy was 125 μJ. The amplified spectrum had a range from 700 nm to 1.0 micrometer supporting a 8.1-fs FWHM pulse. The shot-to-shot energy fluctuation of the amplified signal pulse was less than 1.5 % in RMS.

Finally, the dispersion was managed up to 5th order by use of the AOPDF under the global-dispersion-balance design. The residual phase information was obtained through the MIIPS technique. This is a relatively new technique to measure the phase in single-beam geometry. The setup is therefore quite simple: only an adaptive dispersive device, a nonlinear crystal, and a spectrometer are used. The spectrum of the frequency-doubled beam is measured, while scanning with a sinusoidal phase function, which is added to the original phase of the AOPDF. Based on the trace, the measured phase was fed back to the adaptive dispersive device. The residual dispersion was stepwise compensated with the AOPDF and the glass-block compressor. The high-order dispersions was compensated by use of the AOPDF, while the GDD was mainly compensated by use of the glass-block compressor. The residual dispersion was compensated and the pulse was successfully compressed down to 9.6 fs.

The next step for the further improvement of this 20-kHz OPCPA system is to control the CEP of the signal oscillator by use of an electro-locking-loop device. HHG is quite sensitive to the amplitude of the carrier wave and therefore the stabilization of the CEP is an important theme in the fs-laser-based soft x-ray generation. OPCPA is advantageous in stabilizing CEP because the signal phase is preserved during the optical parametric amplification. Once the CEP is locked in the oscillator, the CEP stability should be maintained in the whole OPCPA system. The locking-loop system including an 0-to-*f* setup is already equipped in our OPCPA system. The CEP-stabilized intense few-cycle pulses will be focused into a noble gas to generate high-flux soft x-ray. This system will be applied to the CEP sensitive time-resolved soft x-ray photoelectron spectroscopy, and high-resolution soft x-ray microscopy.

Zusammenfassung (German translation)

In der vorliegenden Arbeit wurde über die Entwicklung eines OPCPAs für *few-cycle* Pulse im nahen Infrarot mit hoher mittlerer Leistung berichtet. Es wurden sub-10 fs Pulse mit einer Pulsenergie von 125 µJ bei einer Repetitionsrate von 20 kHz erzeugt, was einer mittleren Leistung von 2,5 W und einer Spitzenleistung von 13 GW entspricht. Diese Laserquelle ist einzigartig durch das globale Dispersionsbalancedesign des Grism-Stretcher angewendet auf einen OPCPA mit hoher Repetitionsrate. Das globale Dispersionsbalacedesign des *Grism*-Stretchers hat eine Streckung des Pulses um einen Faktor $>10^4$ auf über 80 ps Pulsdauer in einer Bandbreite von 690 nm bis 1010 nm in einem kompakten Aufbau ermöglicht. Eine Streckung in dieser Größenordnung bietet die Möglichkeit die Pulsenergie weiter zu erhöhen. Dieses Lasersystem könnte durch die Erzeugung von hohen Harmonischen Pulse im XUV, bzw. weichen Röntgenbereich mit hoher mittlerer Leistung erzeugen. Ultrakurzpulsquellen im weichen Röntgenbereich mit hohem Photonenfluss haben ein breites Anwendungsgebiet, z.B. zeitaufgelöste Röntgen-Photoemissionsspektroskopie und hochauflösende Röntgenmikroskopie. Diese Leistungsmerkmale des OPCPAs wurden durch theoretische Überlegungen und schrittweise Experimente erreicht.

Zunächst haben wir die Dynamik der Wellenpropagation in einem nichtlinearen Kristall simuliert. Ein BBO Kristall wurde als Verstärkungsmedium ausgewählt, aufgrund seines hohen Nichtlinearitätskoeffizienten, der hohen Zerstörschwelle und des großen Transparenzbereichs. Die Simulation hat für kleine Signalverstärkungen eine große Abhängigkeit des Verstärkungsspektrums vom nichtkollinearen Winkel und vom Phasenanpassungswinkel gezeigt. Die Kristalldicke und die Pumpintensität haben ebenfalls Einfluss auf die Verstärkungsbandbreite und die Form des Spektrums. Es zeigte sich in diesen Simulationen, dass ein dünner Kristall in Verbindung mit einer hohen Pumpintensität wünschenswert ist. Ein zweistufiger OPCPA wurde mit Hilfe modifizierter gekoppelter Wellengleichungen simuliert, welche den nichtkollinearen Winkel und den *Walk-Off* des Pumpstrahls berücksichtigen. Die

Simulation ergab eine Verschmälerung des Spektrums am Anfang und eine spektrale Verbreiterung durch Rückkonversion ab Erreichen der Sättigung. Eine geeignete Kristalllänge wurde nicht nach der maximalen Ausgangsleistung, sondern dem maximalen Energie-Bandbreitenprodukt (EBP) ausgewählt. Aufgrund der spektralen Verbreiterung im Bereich der Rückkonversion ist die optimale Kristalllänge etwas länger, als die Propagationslänge mit maximaler Ausgangsleistung.

Als nächstes haben wir uns dem Dispersionsmanagement des, mit einer Ausdehnung von über 300 nm, extrem breiten Spektrums gewidmet. Das *Down-Chrip* Schema wurde dabei als Strecker-Kompressorschema angewandt. Die Auswahl des *Grism*-Streckers als Strecker und eines SF 57-Glasblocks als Kompressor ermöglichte eine große Streckung und eine sehr hohe Transmissionseffizienz des Kompressors. Verglichen mit einem konventionellen TOD/GDD-Anpassungsdesign, wurde durch das globale Dispersionsbalancedesign eine Erhöhung des Streckfaktors auf über 10^4 und eine Erweiterung der durchstimmbaren Bandbreite des AOPDFs auf 690 nm bis 1010 nm erreicht. Das globale Dispersionsbalancedesign mit dem *Grism*-Strecker und dem Glasblockkompressor verspricht die Machbarkeit einer Energieskalierung der *few-cycle* Pulse in einem OPCPA.

Der Strahlengang des OPCPAs mit hoher Repetitionsrate wurde basierend auf den Simulationen zur nichtkollinearen optisch parametrischen Wechselwirkung und des Strecker-Kompressordesigns aufgebaut. Das System wurde in zwei Arbeitsschritten aufgebaut: Zunächst mit einem kommerziellen, frequenzverdoppelten Nd:YLF-Pumplaser bei 1 kHz Repetitionsrate, anschließend bei 20kHz mit einem speziell angefertigtem frequenzverdoppeltem Nd:YVO_4-Pumplaser. Wir charakterisierten zuerst den 1 kHz OPCPA indem wir die erreichbare Bandbreite, die Pulskompression und die Pulsenergie bestimmten. Das System verstärkte die Signalpulse spektral breitbandig bei einer zentralen Wellenlänge von 750 nm. Die durch zweifach interne Reflexion im Kristall hervorgerufene Multipulsverstärkung wurde in einer Autokorrelationsmessung beobachtet. Beim 20 kHz OPCPA wurde die Multipulsverstärkung durch die Verwendung von keilförmigen BBO-Kristallen unterdrückt. Eine zweite Stufe wurde entworfen und die Dispersion wurde präzise durch den *Grism*-Strecker und den Glasblockkompressor angepasst. In dem globalen Dispersionsbalancedesign wurde durch den *Grism*-Strecker eine Streckung des Pulses auf mehr als das 10^4-fache erreicht und die hochtransmittierenden Glasblöcke komprimierten die verstärkten Pulse bis auf 14,5 fs FWHM ohne Hilfe eines aktiven Pulsformers. Die OPF wurde mit Hilfe der sog. *Spectral-hole method* gemessen und wurde auf unter 35 µJ unterdrückt. Der zweistufige OPCPA mit 3 Durchgängen erreichte eine Signalverstärkung auf bis zu 175 µJ. Deswegen wurde die effektive Energie, ohne OPF, auf 140 µJ geschätzt. Nach dem Kompressor betrug die Ausgangspulsenergie 125µJ. Das verstärkte Spektrum reichte von 700 nm bis 1 µm und unterstützt damit bis zu 8,1 fs FWHM

Pulse. Die Puls zu Puls-Energiefluktuation der verstärkten Signalpulse betrug weniger als 1,5 % RMS.

Zuletzt wurde die Dispersion bis zur 5. Ordnung mit Hilfe eines AOPDF im globalen Dispersionsbalancedesign angepasst. Die verbliebene Phase wurde durch die MIIPS-Technik bestimmt. Dies ist eine relativ neue Technik um die Phase in einem Einstrahlaufbau zu messen. Deswegen ist der Aufbau einfach: nur ein aktiver Pulsformer, ein nichtlinearer Kristall und ein Spektrometer werden gebraucht. Das Spektrum des frequenzverdoppelten Strahls wird gemessen, während eine sinusförmige Phasenfunktion, die zur ursprünglichen Phase des AOPDFs addiert wird, variiert wird. Auf Grundlage des Messergebnisses wurde die gemessene Phase zurück an den aktiven Pulsformer gegeben. Die verbliebene Dispersion wurde Schrittweise mit dem AOPDF und dem Glasblockkompressor ausgeglichen. Die hohen Ordnungen der Dispersion wurden durch den AOPDF kompensiert, die GDD wurde im Wesentlichen durch den Glasblockkompressor ausgeglichen. Die verbliebene Dispersion wurde kompensiert und der Puls wurde erfolgreich auf bis zu 9,6 fs komprimiert.

Appendix

A: Non-collinear angle

The non-collinear angle is derived from the group-velocity matching and phase-matching condition.

$$\upsilon_{gs} = \upsilon_{gi}\cos(\alpha+\beta) \tag{A1}$$

$$k_p \sin\alpha = k_i \sin(\alpha+\beta) \tag{A2}$$

The equation (A1) shows that the projection of the idler group velocity υ_{gi} along the signal direction equals the signal group velocity υ_{gs}. This equation allows to determine the signal-idler angle $\alpha+\beta$ required for broadband phase matching and can be satisfied only if $\upsilon_{gi} > \upsilon_{gs}$. The equation (A2) comes from the vector equation $k_p = k_s+k_i$. From the equation (A1) and (A2), we can derive the following equation

$$(\frac{k_p}{k_i}\sin\alpha)^2 = 1-(\frac{\upsilon_{gs}}{\upsilon_{gi}})^2 \quad . \tag{A3}$$

Let’s consider the cosine theorem for the pump beam vector

$$\begin{aligned} k_p^2 &= k_i^2 + k_s^2 - 2k_i k_s \cos(\pi-(\alpha+\beta)) \\ &= k_i^2 + k_s^2 + 2k_i k_s \cos(\alpha+\beta) \quad . \end{aligned} \tag{A4}$$

From the equation (A1)

$$\cos(\alpha+\beta) = \frac{\upsilon_s}{\upsilon_i} \quad ,$$

the equation (A4) is changed to the following equation

$$k_p^2 = k_i^2 + k_s^2 + 2k_i k_s \frac{\upsilon_s}{\upsilon_i} \quad . \tag{A5}$$

Then this equation becomes

$$\frac{k_p}{k_i} = \sqrt{1+2\frac{\upsilon_s k_s}{\upsilon_i k_i}+(\frac{k_s}{k_i})^2} \quad . \tag{A6}$$

Then we can get the following form

$$(\frac{k_p}{k_i})^2 = 1 + 2\upsilon_s n_s \omega_s / \upsilon_i n_i \omega_i + (n_s \omega_s / n_i \omega_i)^2 \quad . \tag{A7}$$

By inserting (A7) into the right side value of the equation (A3), we can obtain the following equation

$$\left\{1 + 2\upsilon_s n_s \omega_s / \upsilon_i n_i \omega_i + (n_s \omega_s / n_i \omega_i)^2\right\} \sin^2 \alpha = 1 - (\frac{\upsilon_s}{\upsilon_i})^2 . \tag{A8}$$

This means the noncollinear angle is written in the form of

$$\alpha = \sin^{-1}(\sqrt{\frac{1-(\upsilon_s/\upsilon_i)^2}{1 + 2\upsilon_s n_s \omega_s / \upsilon_i n_i \omega_i + (n_s \omega_s / n_i \omega_i)^2}}) \quad . \tag{A9}$$

B: Relay-imaged telescope

A suitable condition of the pump-beam focusing to the amplifier medium is essential to the effective signal pulse amplification in the medium. The amount of the gain and the gain bandwidth of the seed beam are determined by the pulse duration, phase matching angle, pump beam tilt besides the nonlinear coefficient d_{eff} with an ultimate limitation of the pump intensity due to the damage threshold of the crystals. In the OPCPA simulation in *Chapter 3* a constant intensity was assumed in the whole crystal position. However, the actual laser beam has a spatial divergence in propagation. Fig. B.1 shows the schematic for the ray-tracing of the Gaussian beam. The pump beam is collimated at the focal position by use of a relay-imaged telescope. It consists of two convex lenses to control the collimation of the beam and its intensity. This enables the pump beam to have good spatial overlap with the seed beam at the OPA stage and the beam quality is preserved after several amplifications. In our OPCPA system, we apply a pump laser with M^2 value of less than 1.1. The Gaussian beam is a paraxial solution of the scalar Helmholtz equation and is suitable to describe the propagation of coherent laser beams. The propagation through an optical system can be described by an ABCD matrix. The Gaussian-beam parameter transforms as

$$q_f = \frac{Aq_i + B}{Cq_i + D} \, . \tag{B.1}$$

The ABCD matrix law is valid quite generally as long as the paraxial approximation holds. For example, when the beam propagates in the distance d in vacuum, the following matrix is valid

$$M_v = \begin{pmatrix} A & B \\ C & D \end{pmatrix} = \begin{pmatrix} 1 & d \\ 0 & 1 \end{pmatrix} . \tag{B.2}$$

When the beam propagates in a thin lens, the matrix is given by

$$M_l = \begin{pmatrix} A & B \\ C & D \end{pmatrix} = \begin{pmatrix} 1 & 0 \\ -1/f & 1 \end{pmatrix} . \tag{B.3}$$

The final ray transfer matrix M_f of two successive optical elements M_1 and M_2 is given by

$$M_f = M_1 M_2 \, . \tag{B.4}$$

As shown in Fig. B.1, the beam is actually divergent in propagation so that the beam size is approximately kept constant only around the beam waist. Therefore, the nonlinear crystal is set near the position. The position of the beam waist moves when the 1st and 2nd lens position, and the focal length of them are changed. By use of the ABCD matrix, we can estimate the beam

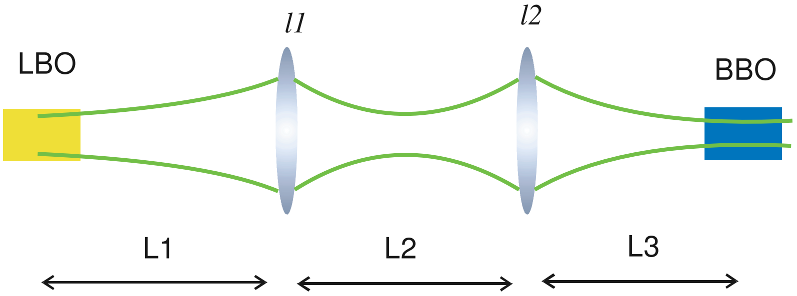

Figure B.1: Relay-imaged telescope. The beam size is controlled by changing the distance between two lenses.

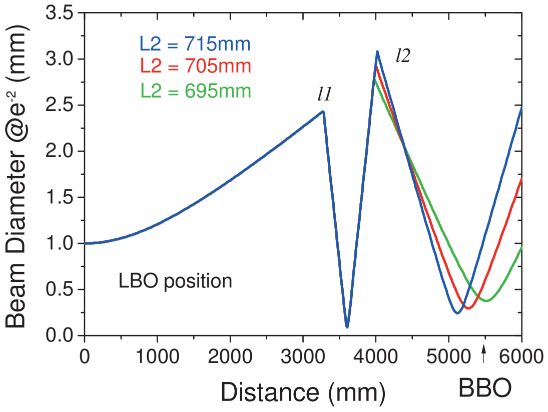

Figure B.2: Calculated beam diameter versus the distance from the LBO crystal in the pump laser to the BBO crystal at the OPA stage.

diameter as a function of the propagation distance. The ray tracing for the relay-imaged telescope is described by use of Eqs (B.2) and (B.3) as

$$M_f = M_{v_3} M_{l_2} M_{v_2} M_{l_1} M_{v_1} \ . \tag{B.5}$$

Note that the order of matrix for each component and the order of the actual optics are vice versa. The simulation result of the pump beam diameter versus the distance from the crystal for the frequency-doubling in the pump laser is shown in Fig. B.2. The position of the 1st and 2nd lens and BBO crystal, and the focal length of both lenses are optimized in the simulation. In the telescope the focal length for each lens is set to 300 mm. The calculation determines the distance from the frequency-doubling LBO crystal in the Nd:YVO$_4$ pump laser to the 1st OPA stage. In experiment we measured the beam diameter at the OPA stage by use of a CCD camera and optimized the telescope position and OPA stage position. Once the position of the OPA stage is settled, the signal beam path is determined so that the both pulses are temporally overlapped in the crystal. For a fine adjustment of the synchronization between the pump and signal pulse, a delay stage is set on the seed beam path. The timing between these two pulses is measured by use of a photodiode at the position of the 1st stage. Both pump and signal beams are relay-image reflected back by use of focal mirrors. The pump intensity in the crystal is set to about 10 GW/cm^2 in 1st and 2nd pass at 1st stage.

References

[1] T. H. Maiman, “Stimulated Optical Radiation in Ruby,“ Nature **187**, 493494 (1960)

[2] B. Lavorel, H. Tran, E. Hertz, O. Faucher, P. Joubert, M. Motzkus, T. Buckup, T. Lang, H. Skenderovi, G. Knopp, P. Beaud, H. M. Frey, “Femtosecond Raman time-resolved molecular spectroscopy,” C. R. Physique, **5**, 215 (2004)

[3] A. Stolow, A. E. Bragg, D. M. Neumark, “Femtosecond Time-Resolved Photoelectron Spectroscopy,” Chem. Rev. **104**, 1719 (2004)

[4] G. R. Fleming, “Chemical Applications of Ultrafast Spectroscopy,” New York, Oxford Univ. Press (1986)

[5] A. H. Zewail, “Femtochemistry: Recent Progress in Studies of Dynamics and Control of Reactions and Their Transition Stages,” J. Phys. Chem. **100** 12701 (1996)

[6] G. Steinmeyer, D. H. Sutter, L. Gallmann, N. Matuschek, U. Keller, “Frontiers in ultrashort pulse generation: pushing the limits in linear and nonlinear optics,“ Science **286**, 1507 (1999)

[7] I. Hertel, W. Radloff, “Ultrafast dynamics in isolated molecules and molecular clusters,” Rep. Prog. Phys. **69**, 1897 (2006)

[8] J. Manz, L. Wöste, “Femtosecond Chemistry,” New York, VCH (1995)

[9] E.Constant, H. Stapelfeldt, P.B. Cokum, “Observation of Enhanced Ionization of Molecular Ions in Intense Laser Fields,” Phys. Rev. Lett. **76**, 4140 (1996)

[10] T. Kobayashi, T. Saito, H. Ohtani, “Real-time spectroscopy of transition states in bacteriorhodopsin during retinal isomerization,”Nature. **414**, 531 (2001)

[11] A. H. Zewail, “Femtochemistry,“ Singapore, World Scienfitic (1994)

[12] P. B. Corkum, “Plasma perspective on strong field multiphoton ionization,” Phys. Rev. Lett. **71**, 1994 (1993)

[13] M. Lewenstein, P. Balcou, M. Y. Ivanov, A. L’huiller, P. B. Corkum, “Theory of high-harmonic geenration by low-frequency laser fields,“ Phys. Rev. A **49**, 2117 (1994)

[14] J. Seres, E. Seres, A. J. Verhoef, G. Tempea, C. Streli, P. Wobrauschek, V. Yakovlev, A. Scrinzi, C. Spielmann, F. Krausz, “Source of coherent kiloelectronvolt X-rays,“ Nature **433**, 596 (2005)

[15] C. Spielmann, N. H. Burnett, S. Sartania, R. Koppitsch, M. Schnürer, C. Kann, M. Lenzner, P. Wobrauschek, F. Krausz, “Generation of coherent X-rays in the water window using 5-femtosecond laser pulses,“ Science **278**, 661 (1997)

[16] I. P. Christov, M. M. Murnane, H. C. Kapteyn, “High-harmonic generation of attosecond pulses in the ‘single-cycle’ regime,” Phys. Rev. Lett. **78**, 1251 (1997)

[17] P. B. Corkum, “Attosecond pulses at last,” Nature **403** 845 (2000)

[18] P. M. Paul, E. S. Toma, P. Breger, G. Mullot, F. Auge, P. Balcou, H. G. Muller, P. Agostini, “Observation of a Train of Attosecond Pulse from High Harmonic Generation,” Science **292**, 1689 (2001)

[19] R. Kienberger, M. Uiberacker, E. Goulielmakis, A. Baltuska, M. Drescher, F. Krausz, “Single sub-fs soft-x-ray pulses: generation and measurement with the atomic transient recorder,“ J. Mod. Opt. **20**, 261 (2005)

[20] R. Kienberger, M. Hentschel, M. Uiberacker, Ch. Spielmann, M. Kitzler, A. Scrinzi, M. Wieland, Th. Westerwalbesloh, U. Kleinberg, U. Heinzmann, M. Drescher, F. Krausz, „Steering attosecond electron wave packets with light,“ Science **297**, 1144 (2002)

[21] G. Sansone, E. Benedetti, F. Calegari, C. Vozzi, L. Avaldi, R. Flammini, L. Poletto, P. Villoresi, C. Altucci, R. Velotta, S. Stagira, S. De Silvestri, M. Nisoli, “Isolated Single-Cycle Attosecond Pulses,” Science **314**, 443 (2006)

[22] F. Krausz, M. Ivanov, “Attosecond physics,” Rev. Mod. Phys. **81**, 163 (2009)

[23] M. Schultze, E. Goulielmakis, M. Uiberacker, M. Hofstetter, J. Kim, D. Kim, F. Krausz, U. Kleineberg, “Powerful 170-attosecond XUV pulses generated with few-cycle laser pulses and broadband multilayer optics,“ New J. Phys. **9**, 243 (2007)

[24] E. Goulielmakis, M. Schultze, M. Hofstetter, V. S. Yakovlev, J. Gagnon, M. Uiberacker, A. L. Aquila, E. M. Gullikson, D. T. Attwood, R. Kienberger, F. Krausz U. Kleineberg, “Single-Cycle Nonlinear Optics,” Science **320**, 1614 (2008)

[25] F. Krausz, “From femtochemistry to attophysics,” Phys. World. **13** 31 (2001)

[26] P. Agostini, L. F. DiMauro, “The physics of attosecond light pulses,” Rep. Prog. Phys. **67**, 813 (2004)

[27] A. Scrinzi, M. Y. Ivanov, R. Kienberger, D. M. Villeneuve, “Attosecond physics,“ J. Pys. B **39**, R1 (2006)

[28] M. Hentschel, R. Kienberger, Ch. Spielmann, G. A. Reider, N. Milosevic, T. Brabec, P. Corkum, U. Heinzmann, M. Drescher, F. Krausz, “Attosecond metrology,“ Nature **414**, 509 (2001)

[29] A. Baltuska, Th. Udem, M. Uiberacker, M. Hentschel, E. Goulielmakis, Ch. Gohle, R. Holzwarth, V. S. Yakovlev, A. Scrinzi, T. W. Hänsch, F. Krausz, “Attosecond control of electronic processes by intense light fields,“ Nature **421**, 611 (2003)

[30] M. Drescher, M. Hentschel, R. Kienberger, M. Uiberacker, V. Yakovlev, A. Scrinzi, Th. Westerwalbesloh, U. Kleinberg, U. Heinzmann, F. Krausz, “Time-resolved atomic inner-shell spectroscopy,“ Nature **419**, 803 (2002)

[31] J. Itatani, J. Levesque, D. Zeidler, H. Niikura, H. Pepin, J. C. Kieffer, P. B. Corkum, D. M. Villeneuve, “Tomographic imaging of molecular orbitals,” Nature **432**, 867 (2004)

[32] E. Goulielmakis, “Direct measurement of light waves,” Science **305** 1267 (2004)

[33] C. A. Larabell, M. A. Le Gros,”X-ray Tomography Generates 3-D Reconstructions of the Yeast, *Saccharomyces cerevisiae*, at 60-nm Resolution,” Mol. Bio. Cell. **15**, 957 (2003)

[34] W. Meyer-Ilse, D. Hamamoto, A. Nair, S. A. Lelievre, G. Denbeaux, L. Johnson, A. L. Pearson, D. Yager, M. A. Legros, C. A. Larabell, “High resolution protein localization using soft X-ray microscopy,” J. Microsc. **201**, 395 (2001)

[35] D. Shapiro, P. Thibault, T. Beetz, V. Elser, M. Howells, C. Jacobsen, J. Kirz, E. Lima, H. Miao, A. M. Neiman, D. Sayre, “Biological imaging by soft x-ray diffraction microscopy,” Appl. Phys. Sci. **102**, 15343 (2005)

[36] M. C. Chen, P. Arpin, T. Popmintchev, M. Gerrity, B. Zhang, M. Seaverg, D. Popmintchev, M. M. Murnane, H. C. Kapteyn, “Bright, Coherent, Ultrafast Soft X-Ray Harmonics Spanning the Water Window form a Tabletop Light Source,” Phys. Rev. Lett. **105**, 173901 (2010)

[37] M. D. Seaberg, D. E. Adams, E. L. Townsend, D. A. Raymondson, W. F. Schlotter, Y. Liu, C. S. Menoni, L. Rogn, C. C. Chen, J. Miao, H. C. Kapteyn, M. M. Murnane, “Ultrahigh 22 nm resolution coherent diffractive imaging using a desktop 13 nm high harmonic source,“ Opt. Exp **19**, 22470 (2011)

[38] P. F. Moulton, “Spectroscopic and laser characteristics of Ti:Al_2O_3,“ J. Opt. Soc. Am. B **3**, 125 (1986)

[39] D. E. Spence, P. N. Kean and W. Sibbette, “60-fsec pulse generation from a self-mode-locked Ti:sapphire laser,” Opt. Lett **16**, 4244 (1991)

[40] A. Baltuska, Z. Wei, M. S. Pshenichnikov, “Optical pulse compression to 5 fs at a 1-MHz repetition rate,“ Opt. Lett. **22**, 102 (1997)

[41] U. Morgner, F. X. Kärtner, S. H. Cho, Y. Chen, H. A. Haus, J. G. Fujimoto, E. P. Ippen, V. Scheuer, G. Angelow, T. Tschudi, “Sub-two-cycle pulses from a Kerr-lens mode-locked Ti:sapphire laser,“ Opt. Lett. **24**, 411 (1999)

[42] D. Strickland and G. Mourou, “Compression of amplified chirped optical pulses,” Opt. Comm. **56**, 219 (1985)

[43] P. Maine, D. Strickland, P. Bado, M. Pessot, and G. Mourou, “Generation of Ultrahigh Peak Power Pulses by Chirped Pulse Amplification,” IEEE J. Quantum Electron. **24**, 398403 (1988)

[44] J. A. Koch, B. J. MacGowan, L. B. Da Silva, D. L. Matthews, J. H. Underwood, P. J. Batson, S. Mrwoka, ”Observation of Gain-Narrowing and Saturation Behavior in Se X-Ray Laser Line Profiles,” Phys. Rev. Lett. **68**, 3291 (1992)

[45] C. Le Blanc, P. Curley, F. Salin, “Gain-narrowing and gain-shifting of ultrashort pulses in Ti:sapphire amplifiers,” Opt. Comm. **131**, 391 (1996)

[46] M. Nisoli, S. De Silvestri, and O. Svelto, “Compression of high-energy laser pulses below 5 fs,” Opt. Lett. **22**, 522 (1997)

[47] G. Stibenz, N. Zhavoronkov and G. Steinmeyer, “Self-compression of millijoule pulses to 7.8 fs duration in a white-light filament,” Opt. Lett. **31**, 274 (2006)

[48] S. Takeuchi, T. Kobayashi, “Broadband near-infrared pulse generation in $KTiOPO_4$,” J. Appl. Phys. **75**, 2757 (1994)

[49] T. Wilhelm, J. Piel, E. Riedle, “Sub-20-fs pulses tunable across the visible from a blue-pumped single-pass noncollienar paramegtric converter,“ Opt. Lett. **22**, 1494 (1997)

[50] G. Cerullo, M. Nisoli, S. De Silvestri, “Generation of 11 fs pulses tunable across the visible by optical parametric amplification,” Appl. Phys. Lett. **71**, 3616 (1997)

[51] A. Shirakawa, T. Kobayashi, “Noncollinearly phase-matchied femtosecond optical parametric amplification with 2000 cm^{-1} bandwidth,” Appl. Phys. Lett. **72**, 147 (1998)

[52] R. A. Baumgartner, R. L. Byer, “Optical Parametric Amplificaiton,” IEEE. J. Quant. Electr. **15**, 432 (1979)

[53] P. A. Franken, A. E. Hill, C. W. Peters, and G. Weinreich, “Generation of optical harmonics,” Phys. Rev. Lett. **7**, 118 (1961)

[54] M. Bass, P. A. Franken, A. E. Hill, C. W. Peters, and G. Weinreich, “Optical mixing,” Phys. Rev. Lett. **8**, 18 (1962)

[55] C. C. Wang, G. W. Racette, “Measurement of parametric gain accompanying optical difference frequency generation,” Appl. Phys. Lett., **6**, 169 (1965)

[56] E. Riedle, M. Beutter, S. Lochbrunner, J. Piel, S. Schenkl, S. Spoerlein, W. Zinth, “Generation of 10 to 50 fs pulses tunable through all of the visible and the NIR,“ Appl. Phys. B **71**, 457 (2000)

[57] A. Shirakawa, I. Sakane, M. Takahashi, T. Kobayashi, “Sub-5-fs visible pulse generation by pulse-front-matched noncollinear optical parametric amplification,” Appl. Phys. Lett. **74**, 2268 (1999)

[58] G. Cerullo, S. De Silvestri, “Ultrafast optical parametric amplifiers,” Rev. Sci. Instrum., **1-18**, 831 (2003)

[59] A. Piskarskas, A. Stabinis, A. Yankauskas, “Phase phenomena in parametric amplifiers and generators of ultrashort light pulses,“ Sov. Phys. Usp. **29**, 869879 (1986)

[60] A. Dubietis, G. Jonusauskas, and A. Piskarskas, “Powerful femtosecond pulse generation by chirped and stretched pulse parametric amplification in BBO crystal,” Opt. Comm. **88**, 43744 (1992)

[61] R. Butkus, R. Danielius, A. Dubietis, A. Piskarskas, A. Stabinis, “Progress in chirped pulse optical parametric amplifiers,” Appl. Phys. B **79**, 693700 (2004)

[62] N. Ishii, L. Ture, V. S. Yakovlev, T. Fuji, F. Krausz, A. Baltuska, R. Butkus, G. Veitas, V. Smilgevicius, R. Danielius, A. Piskarskas, “Multimillijoule chirped parametric amplification of few-cycle pulses,” Opt. Lett. **30**, 567 (2005)

[63] S. Witte, R. Th. Zinkstok, A. L. Wolf, W. Hogervorst, W. Ubachs and K. S. E. Eikema, “A source of 2 terawatt, 2.7 cycle laser pulses based on noncollinear optical parametric chirped pulse amplification,” Opt. Exp. **14**, 8168 (2006)

[64] F. Tavella, Y. Nomura, L. Veisz, V. Pervak, A. Marcinkeviius and F. Krausz, “Dispersion management for a sub-10 fs, 10 TW optical parametric chirped-pulse amplifier,” Opt. Lett. **32**, 2227 (2007)

[65] D. Herrmann, L. Veisz, R. Tautz, F. Tavella, K. Schmid, V. Pervak, F. Krausz, “Generation of sub-three-cycle, 16 TW light pulses by using noncollinear optical parametric chirped-pulse amplification,“ Opt. Lett. **34**, 2459 (2009)

[66] D. Herrmann, C. Homann, R. Tautz, M. Scharrer, P. St. J. Russell, F. Krausz, L. Veisz, E. Riedle, “Approaching the full octave: Noncollinear optical parametric chirped pulse amplification with two-color pumping,” Opt. Exp. **18**, 18752 (2010)

[67] S. Demmler, J. Rothhardt, A. M. Heidt, A. Hartung, E. G. Rohwer, H. Bartelt, J. Limpert, A. Tuennermann, “Generation of high quality, 1.3 cycle pulses by active phase control of an octave spanning supercontinuum,” Opt. Exp. **19**, 20151 (2011)

[68] S. Adachi, N. Ishii, T. Kanai, A.Kosuge, J. Itatani, Y. Kobayashi, D. Yoshitomi, K. Torizuka, S. Watanabe, “5-fs, multi-mJ, CEP-locked parametric chirped-pulse amplifier pumped by a 450-nm source at 1 kHz,” Opt. Exp. **16,** 14341 (2008)

[69] F. Tavella, A. Willner, J. Rothhardt, S. Hädrich, E. Seise, S. Düsterer, T. Tschentscher, H. Schlarb, J. Feldhaus, J. Limpert, A. Tünnermann, J. Rossbach, “Fiber-amplifier pumped high average power few-cycle pulse non-collinear OPCPA,“ Opt. Exp. **18**, 4689 (2010)

[70] J. Rothhardt, S. Hädrich, E. Seise, M. Krebs, F. Tavella, A. Willner, S. Düsterer, H. Schlarb, J. Feldhaus, J. Limpert, J. Rossbach, A. Tünnermann, “High average and peak power few-cycle laser pulses delivered by fiber pumped OPCPA system,“ Opt. Exp. **18** 12719 (2010)

[71] S. Hädrich, S. Demmler, J. Rothhardt, C. Jocher, J. Limpert, and A. Tünnermann, “High-repetition-rate sub-5-fs pulse with 12 GW peak power from fiber-amplifier-pumped optical parametric chirped-pulse amplification,” Opt. Lett. **36**, 313 (2011)

[72] M. Schultze, T. Binhammer, G. Palmer, M. Emons, T. Lang, and U. Morgner, “Multi-μJ, CEP-stabilized, two-cycle pulses from an OPCPA system with up to 500 kHz repetition rate,“ Opt. Exp. **18**, 27291 (2010)

[73] J. Rothhardt, S. Demmler, S. Hädrich, J. Limpert, A. Tünnermann, “Octave-spanning OPCPA system delivering CEP-table few-cycle pulses and 22 W of average power at 1 MHz repetition rate,“ Opt. Exp. **20**, 10870 (2012)

[74] C. Manzoni, D. Polli, G. Cirmi, D. Brida, S. De Silvestri, and G. Cerullo, “Tunable few-optical-cycle pulses with passive carrier-envelope phase stabilization from an optical parametric amplifier,“ Appl. Phys. Lett. **90**, 171111 (2007)

[75] A. Baltuska, T. Fuji and T. Kobayashi, “Self-referencing of the carrier-envelope slip in a 6-fs visible parametric amplifier,” Opt. Lett. **27**, 1241 (2002)

[76] N. Ishii, S. Adachi, Y. Nomura, A. Kosuge, Y. Kobayashi, T. Kanai, J. Itatani, S. Watanabe, “Generation of soft x-ray and water window harmonics using a few-cycle, phase-locked, optical parametric chirped-pulse amplifier,” Opt. Lett. **37**, 97 (2012)

[77] A. E. Siegman, “Lasers,” University Science Books (1986)

[78] J. D. Jackson, “Classical electrodynamics,” Academic Press (1998)

[79] D. J. Jones, S. A. Diddams, J. K. Ranka, A. Stentz, R. S. Windeler, J. L. Hall, and S. T. Cundiff, “Carrier-envelope phase control of femtosecond mode-locked lasers and direct optical frequency systhesis,” Science **288**, 635 (2000)

[80] A. Apolonski, A. Poppe, G. Tempea, C. Spielmann, Th. Udem, R. Holzwarth, T. W. Hänsch, F. Krausz, “Controlling the Phase Evolution of Few-Cycle Light Pulses,“ Phys. Rev. Lett. **85**, 740 (2000)

[81] L. Xu, C. Spielmann, A. Poppe, T. Brabec, F. Krausz, „Ultrabroadband ring oscillator for sub-10-fs pulse generation,“ Opt. Lett. **21**, 2008 (1996)

[82] H. R. Telle, G. Steinmeyer, A. E. Dunlop, J. Stenger, D. H. Sutter, U. Keller, “Carrier-envelope offset phase control: A novel concept for absolute optical frequency measurement and ultrashort pulse generation,“ Appl. Phys. B **69**, 327 (1999)

[83] S. Witte, “Terawatt-intensity few-cycle laser pulses-Optical parametric chirped-pulse amplification and frequency comb spectroscopy,” Ph. D thesis, University of Amsterdam (2007)

[84] O. D. Mucke, O. Kuzucu, F. N. C. Wong, E. P. Ippen, F. X. Kaerhner, S. M. Foreman, D. J. Jones, L. S. Ma, J. L. Hall, J. Ye, “Experimental implementation of optical clockwork without carrier-envelope phase control,“ Opt. Lett. **29**, 2806 (2004)

[85] M. Zimmermann, Ch. Gohle, R. Holzwarth, Th. Udem, T. W. Hänsch, “Optical clockwork with an offset-free difference-frequency comb: accuracy of sum- and difference-frequency generation,” Opt. Lett. **29** 310 (2004)

[86] A. Baltuska, T. Fuji, T. Kobayashi, “Controlling the Carrier-Envelope Phase of Ultrashort Light Pulses with Optical Parametric Amplifiers,“ Phys. Rev. Lett. **88**, 133901 (2002)

[87] T. Fuji, A. Apolonski, F. Krausz, “Self-stabilization of carrier-envelope offset phase by use of difference-frequency generation,” Opt. Lett., **29**, 632 (2004)

[88] T. Fuji, J. Rauschenberger, A. Apolonski, V. S. Yakovlev, G. Tempea, T. Udem, C. Gohle, T. W. Hänsch, W. Lehnert, M. Scherer, F. Krausz, “Monolithic carrier-envelope phase-stabilization scheme,” Opt. Lett., **30**, 332 (2005)

[89] Z. Wei, H. Han, W. Zhang, Y. Zhao, J. Zhu, H. Teng, Q. Du, “Measurement and Control of Carrier-Envelope Phasein Femtosecond Ti:sapphire Laser,” Advance in Solid-State Lasers: Development and Applicatios, **14**, 301 (2010)

[90] W. Zhang, H. Han, Y. Zhao, Q. Du, Z, Wei, “A 350 MHz Ti:sapphire laser comb based on monolithic scheme and absolute frequency measurement of 729 nm laser,” Opt. Exp. **17**, 6059 (2009)

[91] R. Holzwarth, Th. Udem, T. W. Hänsch, J. C. Knight, W. J. Wadsworth, and P. S. J. Russell, “Optical frequency synthesizer for precision spectroscopy,” Phys. Rev. Lett. **85**, 2264 (2000)

[92] K. L. Sala, G. A. Kenny-Wallace, G. E. Hall, “CW Autocorrelation Measurements of Picosecond Laser Pulses,” IEEE. J. Quantum Electron. **16**, 990 (1980)

[93] W.Rudolph, B. Wilhelmi, “Light pulse compression,” Harwood academic publishers (1989)

[94] J.-C. Diels, J. J. Fontaine, I. C. McMichael, F. Simoni, “Control and measurement of ultrashort pulse shapes (in amplitude and phase) with femtosecnd accuracy,“ Appl. Opt. **24**, 1270 (1985)

[95] F. Hasche, T. J. Driscoll, W. Cavallari, G. M. Gale, “Measurement of ultrashort pulse durations by interferometric autocorrelation: unfluence of various parameters,” Appl. Opt. **35**, 3230 (1996)

[96] A. Baltuska, “Hydrated Electron Dynamics Explored with 5-fs Optical Pulses,” Ph.D Thesis, University of Groningen (2000)

[97] K. Naganuma, K. Mogi, H. Yamada, “General Method for Ultrashort Light Pulse Chirped Measureent,” IEEE J. Quantum Electron. **25**, 1225 (1989)

[98] J. W. Nicholson, W. Rudolph, "Noise sensitivity and accuracy of femtosecond pulse retriecal by phase and intensity from correlation and spectrum only (PICASO)," J. Opt. Soc. Am. B **19**, 330 (2002)

[99] R. Trebino, D. J. Kane, "Using phase retrieval to measure the intensity and phase of ultrashort pulses: frequency-resolved optical gating," J. Opt. Soc. Am. A. **10**, 1101 (1993)

[100] R. Trebino, K. W. DeLong, D. N. Fittinghoff, J. N. Sweetser, M. A. Krumbugel, B. A. Richman, and D. J. Kane, "Measuring ultrashort laser pulses in the time-frequency domain using frequency-resolved optical gating," Rev. Sci. Instrum. **68**, 3277 (1997)

[101] K. W. Delong, R. Trebino, J. Hunter, W. E. White, "Frequency-resolved optical gating with the use of second-harmonic generation," J. Opt. Soc. Am. B **11**, 2206 (1994)

[102] C. Iaconis, I. A. Walmsley, "Spectral phase interferometry for direct electric-field reconstruction of ultrashort optical pulses," Opt. Lett. **23**, 792 (1998)

[103] V. A. Zubuv, T. I. Kuznetsova, "Solution of the phase problem for time-dependent optical signals by an interference system," Sov. J. Quant. Electr. **21**, 1285 (1991)

[104] C. Iaconis, I. A. Walmsley, "Self-Referencing Spectral Interferometry for Measuring Ultrashort Optical Pulses," Opt. Lett. **19**, 287 (1994)

[105] F. X. Kaertner, "Few-Cycle Laser Pulse Generation and its Applications," New York, NY Springer-Verlag (2004)

[106] I. Walmsley, L. Waxer, C. Dorrer, "The role of dispersion in ultrashort optics," Rev. Sci. Instrum. **72** 1 (2001)

[107] J. -C. Diels, W. Rudolph, Ultrashort laser phenomena, American Press. San Diego (1996)

[108] M. E. Anderson, L. E. E. de Araujo, E. M. Kosik, I. A. Walmsley, "The effects of noise on ultrashort-optical-pulse measurement using SPIDER," Appl. Phys. B **70**, 85 (2000)

[109] A. M. Weiner, "Ultrafast Optics," Wiley (2009)

[110] V. V. Lozovoy, I. Pastirk, and M. Dantus, "Multiphoton intrapulse interference. IV. Ultrashort laser pulse spectral phase characterization and compensation," Opt. Lett. **29**, 775 (2004)

[111] B. Xu, J. M. Gunn, J. M. Dela Cruz, V. V. Lozovoy, and M. Dantus, "Quantitative investigation of the multiphoton intrapulse interference phase scan method for simultaneous phase measurement and compensation of femtosecond laser pulses," J. Opt. Soc. Am. B. **23**, 750 (2006)

[112] V. V. Lozovoy, M. Dantus, "Systematic Control of Nonlinear Optical Process Using Optimally Shaped Femtosecond Pulses," Chem. Phys. Chem, **6**, 1970, 2005

[113] J. Shane, "Optical micromanipulation using dispersion-compensated and phase-shaped ultrashort pulsed lasers," MPhil thesis, Michigan state university (2009)

[114] V. V. Lozovoy, I. Pastirk, K. A. Walowicz, and M. Dantus, "Multiphoton intrapulse interference. ii. control of two- and three-photon laser induced fluorescence with shaped pulses," J. Chem. Phys. **118**, 3187 (2003)

[115] F. Tavella, "Multiterawatt few-cycle pulse OPCPA for applications in high field physics," Ph. D thesis, Ludwig-Maximilians Universität München (2007)

[116] V. G. Dmitriev, G. G. Gurzadyan, D. N. Nikogosyan, “Handbook of Nonlinear Optical Crystals,” Springer (1997)

[117] H. Hellwig, J. Liebertz, L. Blhaty, “Linear optical properties of the monoclinic bismuth borate BiB$_3$O$_3$,“ Journ. Of Appl. Phys., **88**, 240 (2000)

[118] J. Kroupa, D. Kasprovicz, A. Majkrowki, E. Michalski, M. Drozdowski, “Optical Properties of Bismuth Triborate (BiBO) Single Crystal,“ Ferroelectrics: Taylor and Francis **318** 7782 (2005)

[119] D. Xue, S. Zhang, “Structure and non-linear optical properties of □-Barium Borate,” Acta. Cryst., **54**, 652 (1998)

[120] N. Ishii, “Development of optical parametric chirped-pulse amplifiers and their applications,” Ph. D thesis, Ludwig-Maximilians Universität München (2006)

[121] Castech. Inc, Manufacture data (2012)

[122] I. Jovanovic, B. J. Comaskey, D. M. Pennington, “Angular effects and beam quality in optial parametric amplification,” J. Appl. Phys., **90** 4328 (2001)

[123] S. E. Harris, M. K. Oshman, R. L. Byer, “Observation of Tunable Optical Parametric Fluorescence,” Phys. Rev. Lett., **18**, 732 (1967)

[124] R. L. Byer, S. E. Harris, “Power and Bandwidth of Spontaneous Parametric Emission,” Phys. Rev. **168**, 1064 (1968)

[125] J. A. Armstrong, “Interactions between light waves in a nonlinear dielectric,” Phys. Rev. **127** 1918 (1962)

[126] M. Yamada et al. “First-order quasi-phase matched LiNbO$_3$ waveguide periodically poled by applying an external field for efficient blue second-harmonics generation,” Appl. Phys. Lett., **62**, 435 (1993)

[127] P. D. Maker, R. W. Terhune, M. Nisenoff, and C. M. Savage, “Effects of dispersion and focusing on the production of optical harmonics,” Phys. Rev. Lett. **8**, 19 (1962)

[128] S. Reisner, M. Gutmann, “Numerical treatment of UV-pumped white-lignt-seeded single-pass noncollinear parametric amplifiers,“ J. Opt. Soc. Am. B, **16** 1801 (1999)

[129] D. N. Schimpf, J. Rothardt, J. Limpert, A. Tuennermann, D. C. Hanna, “Theoretical analysis of the gain bandwidth for noncollinear parametric amplification of ultrafast pulses,“ J. Opt. Soc. Am. B, **24**, 2837 (2007)

[130] A. Shirakawa, “Sub-5-fs pulse generation by noncollinear optical parametric amplification and its application to the study of geometrical relaxation in polydiacetylenes,” Ph. D thesis, University of Tokyo (1998)

[131] C. Manzoni, D. Polli, G Cerullo, “Two-color pump-probe system broadly tunable over the visible and the near infrared with sub-30 fs temporal resolution,” Rev. Sci. Instr. **77**, 023103 (2006)

[132] J. Zheng, H. Zacharias, “Non-collinear optical parametric chirped-pulse amplifier for few-cycle pulses,” Appl. Phys. B, **97**, 765 (2009)

[133] I. N. Ross, P. Matousek, M. Towrie, A. J. Langley, J. L. Collier, “The prospects for ultrashort pulse duration and ultrahigh intensity using optical parametric chirped pulse amplifiers,” Opt. Comm., **144**, 125 (1997)

[134] G. M. Gale, M. Cavallari, F. Hache, “Femtosecond visible optical parametric oscillator,” J. Opt. Soc. Am. B, **15**, 702 (1998)

[135] I. N. Ross, P. Matousek, G. H. C. New, K. Osvay, “Analysis and optimization of optical parametric chirped pulse amplification,” J. Opt. Soc. Am. B **19**, 2945 (2002)

[136] G. Cerullo, S. De Silvestri, ”Ultrafast optical parametric amplifiers,” Rev. Sci. Instr. **74**, 1 (2003)

[137] F. Tavella, A. Marcinkevicius, F. Krausz, “Investigation of the superfluorescence and signal amplification in an ultrabroadband multiterawatt optical parametric chirped pulse amplifier system,” New. J. Phys. **8**, 219 (2006)

[138] S. Witte, R. T. Zinkstok, W. Hogervorst, K. Eikema, “Numerical simulations for performance optimization of a few-cycle terawatt NOPCPA system,” Appl. Phys. B, **87**, 677(2007)

[139] J. Moses, C. Manzoni, S. Huang, G. Cerullo, F. X. Kärtner, “Temporal optimization of ultrabroadband high-energy OPCPA,” Opt. Exp., **17**, 5540 (2009)

[140] G. A. Reider, “Photonik”, Springer (2006)

[141] J. Zheng, Private communication (2012)

[142] R. L. Fork, O. E. Martinez, J. P. Gordon, “Negative dispersion using pairs of prisms,” Opt. Lett. **9**, 150 (1984)

[143] E. B. Treacy, “Optical Pulse Compression with Diffraction Gratings,” IEEE J. Quantum Electron. **5**, 454 (1969)

[144] S. Kane, J.Squier, “Grism-pair stretcher-compressor system for simultaneous second- and third- order dispersion compensation in chirped-pulse amplification,” J. Opt. Soc. Am. B **14**, 661 (1997)

[145] M. Ware, W. E. Dibble, S. A. Glasgow, and J. Peatross, ”Energy flow in angularly dispersive optical systems,” J. Opt. Soc. Am. B, **18**, 6 (2001)

[146] P. Tournois, “New diffraction grating pair with very linear dispersion for laser pulse compression,” Electron. Lett. **29**, 1414 (1993)

[147] S. Kane, J. Squier “Grating Compression of Third-Order Material Dispersion in the Normal Dispersion Regeme: Sub-100-fs Chirped-Pulse Amplification Using a Fiber Stretcher and Grating-Pair Compressor,” IEEE J. Quantum Electron. **31**, 2052 (1995)

[148] J. Zheng, H. Zacharias, “Design consideration for a compact stretcher for non-collinear optical chirped-pulse amplification,” Appl. Phys. B. **96** 445 (2009)

[149] E. A. Gibson, D. M. Gaudiosi, H. C. Kapteyn, R. Jimenez, S. Kane, R. Huff, C. Durfee, J. Squier, “Efficient reflection grisms for pulse compression and dispersion compensation of femtosecond pulses,” Opt. Lett. **31**, 3363 (2006)

[150] T. Dou, R. Tautz, X. Gu, G. Marcus, T. Feurer, F. Krausz, L. Veisz, “Dispersion control with reflection grisms of an ultra-broadband spectrum approaching a full octave,“ Opt. Exp., **18**, 27900 (2010)

[151] D. M. Gaudiosi, A. L. Lytle, P. Kohl, M. M. Murnane, H. C. Kapteyn, and S. Backus, “11-W average power Ti:sapphire amplifier system using downchirped pulse amplification,” Opt. Lett. **29**, 2665 (2004)

[152] S. Backus, C. G. Durfee III, M. M. Murnane, H. C. Kapteyn, “High power ultrafast lasers,” Rev. Sci. Instrum. **69** 1211 (1998)

[153] L. S. Ma, K. K. Shelton, H. C. Kapteyn, M. M. Murnane, J. Ye, ”Sub-10-femtosecond active synchronizatin of two passibely mode-locked Ti :sapphire oscillators,” Phys. Rev. A, **64**,021802 (2001)

[154] R. Paschotta, “Noise of mode-locked laser (Part II): timing jitter and other fluctuations,” Appl. Phys. B **79**, 163 (2004)

[155] D. W. Allan, “Statistics of Atomic Frequency Standards,” Proc. IEEE 54, 221 (1966)

[156] A. L. Oien, I. T. Mckinnie, P. Jain, N. A. Russel, D. M. Warrington, and L. A. W. Gloster, “Efficient, low-threshold collinear and noncollinear β-barium borate optical parametric oscillators,” Opt. Lett. **22**, 859 (1997)

[157] F. Tavella, K. Schmid, N. Ishii, A. Marchinkevicius, L. Veisz, F. Krausz, “High-dynamic range pulse-contrast measurements of a broadband optical parametric chirped-pulse amplifier,“ Appl. Phys. B, **81**, 753 (2005)

[158] M. Lührmann, C. Theobald, R. Wallenstein and J. A. L’huillier, “Efficient generation of mode-locked pulses in Nd:YVO_4 with a pulse duration adjustable between 34 ps and 1 ns,” Opt. Exp. **17**, 6177 (2009)

[159] M. Lührmann, C. Theobald, R. Wallenstein and J. A. L’huillier, “High energy cw-diode pumped Nd:YVO_4 regenerative amplifier with efficient second harmonics generation,“ Opt. Exp. **17**, 22761 (2009)

[160] X. Gu, G. Marcus, Y. Deng, TMetzger, C. Teisset, N Ishii, T. Fuji, A. Baltuska, R. Butkus, V. Pervak, H. Ishizuki, T. Taira, T. Kobayashi, R. Kienberger and F. Krausz, Opt. Express, **17**, 62 (2008)

[161] Y. Cha, Y. Lee, S. Nam, J. Han, Y. Rhee, B. Yoo, B. Lee, Y. Jeong, “Simple method for the temporal characterization of amplified spontaneous emission in femtosecond terawatt T:sapphire lasers,” Appl. Opt. **46**, 6854 (2007)

[162] F. Träger, “Springer Handbook of Lasers and Optics,” Springer (2007)

[163] A. M. Weiner, “Femtosecond pulse shaping using spatial light modulators,” Rev. Sci. Instr. **71**, 1929 (2000)

[164] D. Kaplan P. Tournois, “Theory and Performance of the Acousto-Optic Programmable Dispersive Filter used for Femtosecond Laser Pulse Shaping,” Journal de Physique IV France **12**, 69 (2002)

[165] F. Verluise, V. Laude, J. P. Huignard, P. Tournois, A. Migus, “Arbitrary dispersion control of ultrashort optical pulses with acoustic waves,” J. Opt. Soc. Am. B, **17**, 138 (2000)

[166] V. Y. Molchanov, S. I. Chizhikov, O. Y. Makarov, N. P. Solodovnikov, V. N. Ginzburg, E. V. Katin, E. A. Khazanov, V. V. Lozhkarev, I. V. Yakovlev, “Adaptive acousto-optic technique for femtosecond laser pulse shaping,” Appl. Opt. **48**, 118 (2009)

[167] T. Hamann, “Adaptive Compression of Intense Ultrashort OPCPA Laser Pulses“, Diplomarbeit, Westfälischen Wilhelms-Universität Münster (2010)

[168] N. Kleimeier, T. Haarlammert, H. Witte, U. Schühle, J. Hochedez, A. BenMoussa, and H. Zacharias, “Autocorrelation and phase retrieval in the UV using two-photon absorption in diamond pin photodiodes,“ Opt. Exp. **18**, 6945 (2010)

Danksagung

An dieser Stelle möchte ich mich herzlich bei all jenen bedanken, die zum Gelingen dieser Arbeit beigetragen haben. Besonderer Dank geht an:

- …Prof. Helmut Zacharias für die Möglichkeit in seiner Arbeitsgruppe zu studieren, die interessante Aufgabenstellung sowie seine Betreuung und Unterstützung bei der Durchführung dieses Projekts.
- …Prof. Carsten Fallnich für die kurzfristige Begutachtung und Bewertung dieser Arbeit.
- …Dr. Jiaan Zheng für seine gute Betreuung und passende Diskussion in meiner Laborarbeit sowie die nette Leitung bei meiner Doktorarbeit. Außerdem möchte ich mich noch bei ihm dafür bedanken, dass er mir die Freude an der Forschung nahe gebracht hat.
- …Dr. Thoben Haarlammart und Daniel Nürenberg für das Korrekturlesen in letzter Sekunde und die brauchbare Diskussion.
- …Thomas Hamann für die Hilfestellungen im Laboralltag und seine alltägliche Unterstützung beim Lernen der deutschen Sprache.
- …Frank Wahlert, Sven Eppenhoff und Tamara Kleimann für die Lösung zahlreicher technischer Probleme und die schnelle und hervorragende Bearbeitung von Aufträgen.
- …Anja Fliß für die allgemein Hilfe im Büro und die gute Arbeitsatmosphäre
- …die Mitglieder der Arbeitsgruppe Zacharias für die allgemein gute Arbeitsatmosphäre, die erheiternden Diskussionen sowie die interessanten Zafernafahrten.

Zuletzt möchte ich meiner Familie danken, die mich während meines Studiums finanziell und emotional unterstützt hat. Neben meinen Eltern geht dabei besonderer Dank an meine Freunde, Kaori Shinohara und Midori Okuno, die mir im Privatleben geholfen haben.